UC Davis
UC Davis Electronic Theses and Dissertations

Title

Sustainable Biomass Utilization: Exploring Advanced Materials and Carbon-Neutral Industrial Products

Permalink

https://escholarship.org/uc/item/1hf9v9zr

Author

Wei, Jiahui

Publication Date

2024

Peer reviewed|Thesis/dissertation

Sustainable Biomass Utilization: Exploring Advanced Materials and Carbon-Neutral Industrial Products

By

JIAHUI WEI
DISSERTATION

Submitted in partial satisfaction of the requirements for the degree of

DOCTOR OF PHILOSOPHY

in

Chemistry

in the

OFFICE OF GRADUATE STUDIES

of the

UNIVERSITY OF CALIFORNIA

DAVIS

Approved:

Mark Mascal, Chair

Dean, J, Tantillo

Shota, Atsumi

Committee in Charge

2024

Table of Contents

Abstract

This Ph.D. thesis investigates the versatile applications of biomass derivatives including cellulose, the most abundant polymer in nature.

Chapter 1 provides a general introduction to the research areas covered in this thesis.

Chapter 2 explores the utility of trifluoroacetic acid (TFA) as a dispersing medium for cellulose nanocrystals (CNCs), emphasizing its distinctive solvent properties and its ability to stabilize CNC suspensions. The study demonstrates the dispersibility of native CNCs in TFA and investigates the aging of CNC-TFA suspensions, resulting in the gradual addition of trifluoroacetyl groups to the CNC surface. This method is extended to the formation of a nanocomposite with polyethylene terephthalate (PET), presenting a promising strategy for combining organic-soluble polymers with native cellulose.

Chapter 3 introduces an innovative concept involving dyes synthesized entirely from biomass-derived platform molecules, specifically 5-(chloromethyl)furfural (CMF), which can be produced directly from cellulose in a one-step reaction. This methodology circumvents the limitations associated with petrochemical-derived dyes and natural colorants. Using a furylogous malonate or furylogous cyanoacetate and biomass-derived aldehydes, the study process generates industrially relevant synthetic colorants with vibrant hues, demonstrating excellent performance and fastness on selected fabrics. The vision of achieving 100% renewable textiles, where both synthetic fibers and dyes are biobased, is discussed, constituting a transformative approach to sustainable wearables.

In Chapter 4, the focus shifts to the transformation of CMF into 2,5-diformylfuran

(DFF), which is used in the synthesis of the sustainable dyes in Chapter 3, through oxidation with bismuth nitrate pentahydrate. The study spans different scales, and works toward optimizing yields and addressing challenges encountered during scale-up. Techniques such as continuous extraction, sonication, and variations in extraction solvents are employed to enhance reproducibility. Despite the progress made, further work will be necessary to give consistent yields, particularly at larger scales. Collectively, these chapters significantly contribute to the evolving landscape of sustainable materials and processes, showcasing the potential for innovative applications across diverse fields.

Acknowledgements

I would like to express my appreciation for all the support from my family, especially my parents, without whom I could not have made this happen.

I would also like to extend my gratitude to my academic advisor, Dr. Mark Mascal, for his patient guidance and advice on my Ph.D. projects. It is a great fortune to have Mark as my advisor during my Ph.D. period.

Moreover, I would like to thank the current and former members of the Mascal group, including Dr. Zheng Li, Dr. Jan Saska, Dr. Jingjing Meng, Dr. Boqiong Lu, Dr. Andrew Otsuki, Dr. Haoqian Miao, Dr. Nikolay E. Shevchenko, Lena Svanholm, Joseph Beckett, Huitao Ling, and Jordan Lara.

Finally, I would like to express my gratitude to Dr. Kristie J Koski and Dr. Melekeh Nasiri for their support!

1 Introduction

Biomass chemistry is a crucial field of study that delves into chemical transformations encompassing plant and animal sources. This area of research is driven by the urgent need for sustainable alternatives to traditional fossil fuels and petrochemical-based materials. Understanding the chemical composition of biomass is paramount in developing efficient methods for biomass utilization, conversion, and valorization. Investigating the intricate molecular structures of biomass components such as cellulose, hemicellulose, and lignin is pivotal for advancing technologies like biofuel production, biorefinery processes, and the development of renewable materials. Biomass chemistry plays an important role in unlocking the potential of renewable resources, contributing to the transition towards a more sustainable and environmentally friendly bio-based economy.
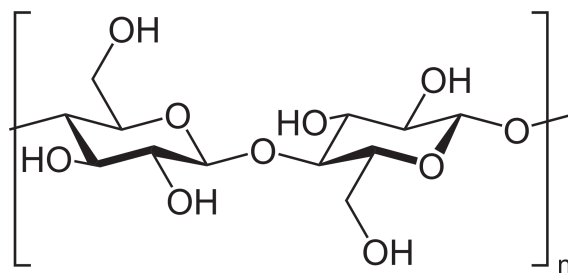
Figure 1.1: Structure of cellulose

1.1 Cellulose Nanocrystals (CNC)

Cellulose, the most abundant molecule in nature, is characterized by a linear syndiotactic homopolymer of D-anhydroglucopyranose linked by β-(1,4) glycosidic bonds (Figure 1.1). Its unique structural features arise from intricate hydrogen bonding interactions, both intra- and intermolecular, coupled with Van der Waals forces. These interactions result in linear and rigid polymer chains that organize into crystalline regions, reaching dimensions exceeding hundreds of nanometers in length and around

ten nanometers in width. The self-assembly of these crystalline regions forms cellulose nanocrystals (CNCs) which, due to their inherent rigidity, when bundled into cellulose microfibrils, contribute to the exceptional strength of plant cell walls. Various techniques are employed for the isolation of CNCs, with acid hydrolysis being a widely used method, involving strong acids such as sulfuric acid (Revol et al., 1994; X. M. Dong et al., 1998). This method selectively removes amorphous regions, leaving behind crystalline cellulose in the form of nanorods. Other acids like hydrochloric acid (Yu et al., 2013), phosphoric acid (Camarero Espinosa et al., 2013), acetic acid, butyric acid (Braun et al., 2012), and citric acid (Spinella et al., 2016) have also been employed in cellulose hydrolysis, acting as both solvents and reactants.

1.1.1   Applications of CNCs

Figure 1.2 provides a comprehensive graphical overview of cellulose nanocrystal (CNC) literature on applications, biomedical engineering, antimicrobial/antiviral systems, tissue engineering, biosensors, and drug/gene delivery. In biomedical engineering, CNC toxicity studies, specifically through inhalation and cellular uptake pathways, are critical for assessing their biomedical utility. CNCs prepared via sulfuric acid hydrolysis, which feature negative surface charges, exhibit minimal cell internalization (Mahmoud et al., 2010). Furthermore, Endes et al. studied interactions between CNCs and a multicellular in vitro model of the epithelial airway barrier post aerosol exposure, revealing distinct uptake behaviors influenced by nanofiber length and concentration. Longer tunicate-derived CNCs exhibited reduced clearance compared to shorter cotton-derived CNCs, highlighting the importance of considering both length and concentration in assessing their interaction with lung cells in vitro (Endes et al., 2015). CNCs improve structural stability and increase the elastic modulus of injectable hydrogels. Gelation occurs rapidly upon extrusion, with CNCs evenly distributed

throughout the composite, demonstrating enhanced elasticity and dimensional stability, making them suitable for biomedical applications such as drug delivery and tissue engineering (Yang et al., 2013). Despite decreased cell adhesion caused by CNC hydrophobicity, CNCs promote long-term cell proliferation and reduce enzymatic degradation (K. Wang et al., 2016). CNCs produced by acidic processing can also play a role in bone regeneration on bioactive glasses (BG). Cell culture studies indicate that the presence of BG/CNCs blended coating substantially accelerated cell attachment, spreading, proliferation, differentiation, and mineralization of an extracellular matrix (Chen et al., 2015).

For antimicrobial systems, CNCs incorporated with Ag nanoparticles demonstrate properties that enhance their adherence to bacterial surfaces, resulting in effective inhibition of bacterial growth (Shi et al., 2015). Furthermore, Ag nanoparticle-coated CNCs display potential for aqueous glucose detection (S. Wang et al., 2016). In the realm of biomarkers/biosensors, CNCs conjugated with fluorescent fluorescein isothiocyanate (FITC) molecules serve as versatile tools for monitoring cellular internalization, biomolecule sensing, and diagnosing diseases (S. Dong and Roman, 2007). Similarly, functional high surface area scaffolds based on cellulose nanocrystals (CNCs) and poly(vinyl alcohol) (PVA) were developed for fluorescence-based sensing, offering a facile immobilization platform for biological probes. These nanocomposite films, deposited on glass substrates, exhibited porous nanostructures fixated by heat treatment, enabling the detection of pH changes and protease activity at concentrations typical for abnormal proteolytic activity in wound fluids (Schyrr et al., 2014).

CNC-based biosensors developed were subsequently employed in drug delivery systems. Folic acid-conjugated CNCs, targeting cancer cells, outperformed FITC CNCs in tests on rat and human brain tumor cells (S. Dong et al., 2014). Grafted CNCs were used in pH-dependent drug release, displaying high binding efficiency, stability,
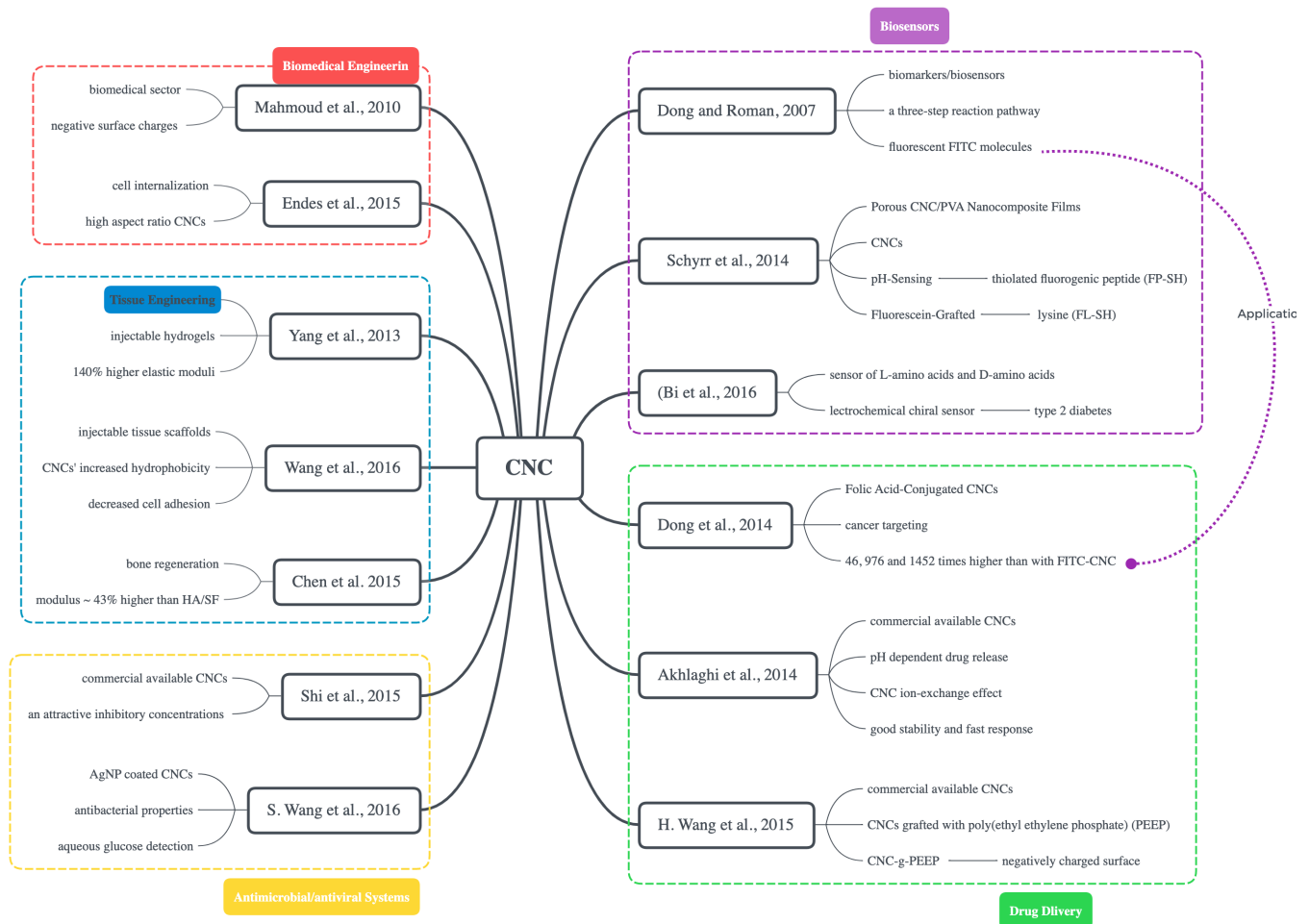
3

Figure 1.2: Graphical literature map describing CNC applications

and response (Akhlaghi et al., 2014). Other applications include the use of grafted CNCs in drug delivery systems, for example using the antitumor drug doxorubicin (H. Wang et al., 2015).

In conclusion, CNCs exhibit versatility and promise across diverse domains, showcasing remarkable properties for various applications. Their unique features, including high surface area, controllable dimensions, and tunable surface chemistry, make them valuable tools across various applications. The above discussed applications underscore the potential of CNCs to contribute to sustainable and innovative solutions, reshaping the landscape of materials science.

1.1.2   CNC PET Composites

The incorporation of cellulose nanocrystals (CNCs) into polymer matrices is a topic of growing interest, offering a novel approach to enhance the properties of polymeric materials. Chapter 2 of this thesis will specifically explore the combination of CNCs with polyethylene terephthalate (PET) to demonstrate the production of a nanocomposite. Derived from abundant and renewable cellulose, CNCs possess exceptional mechanical strength, low density, and eco-friendly attributes, making them attractive as reinforcing agents in polymer matrices. The structure of PET, a widely used thermoplastic polymer known for its durability and versatility, can be further optimized by integrating CNCs. The synergistic effects resulting from this integration hold the promise of creating nanocomposites with better mechanical, thermal, and barrier properties compared to PET itself. This introduction briefly introduces the synthesis, characterization, and potential applications of CNC-reinforced PET nanocomposites, which can contribute to the field of sustainable and high-performance materials.

As outlined in Figure 1.3, some methods for synthesizing cellulose/PET nanocomposites include thermal processing, co-precipitation from trifluoroacetic acid (TFA),
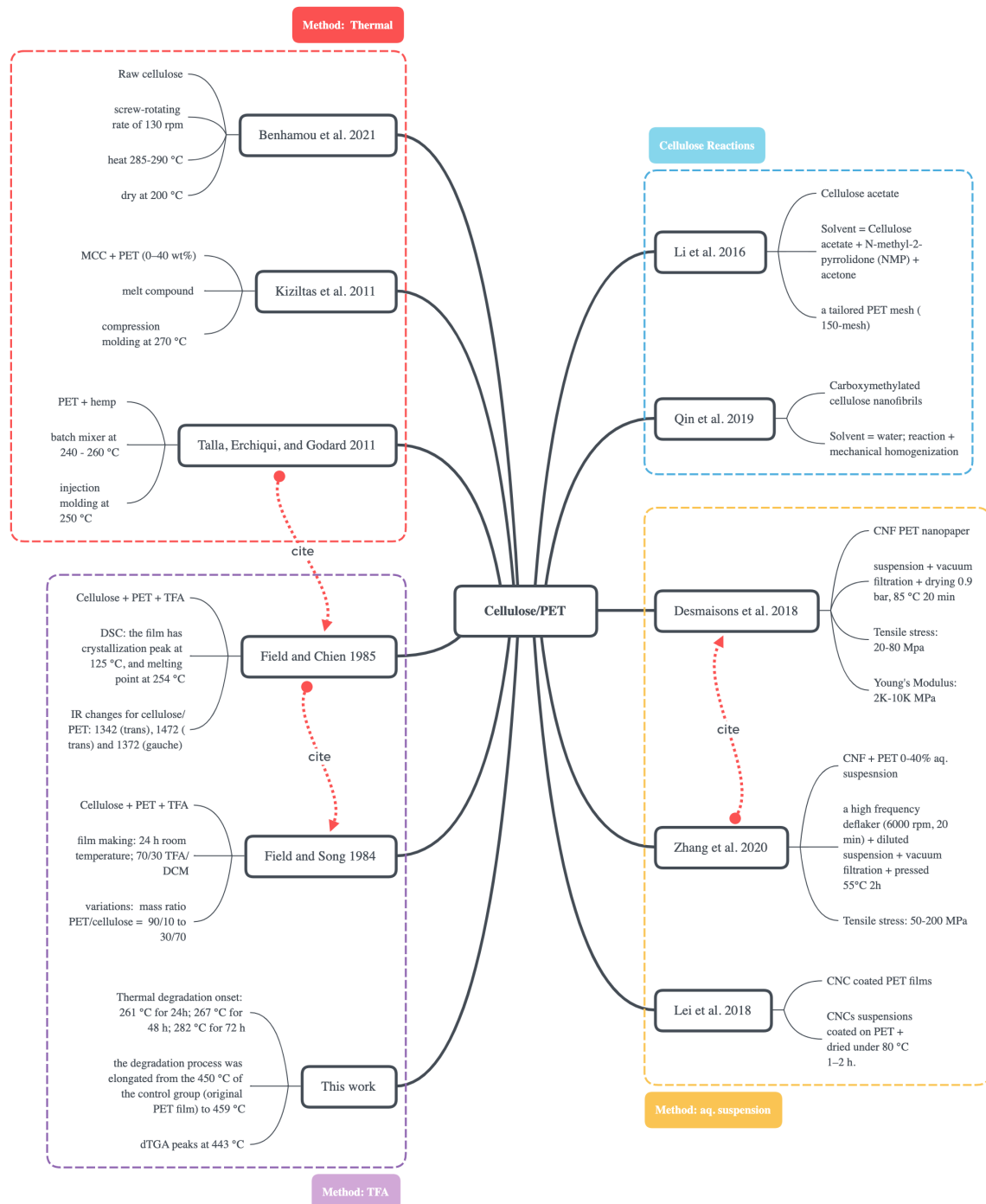
Figure 1.3: Graphical literature map describing Cellulose PET nanocomposite.

modification by chemical derivatization, and film coating.

In thermal methods, studies by Benhamou et al. demonstrated that heating cellulose with PET at 285-290 °C resulted in an 88% increase in Young's modulus and a 36% increase in tensile strength (Benhamou et al., 2022). Kiziltas et al. heated microcrystalline cellulose (MCC) at 270 °C with PET, which showed that the thermal stability of the composite decreased with increasing MCC content (Kiziltas et al., 2011). Talla et al. investigated the thermal degradation of a cellulose/PET composite, generated by blending cellulose and PET and heating it at 250 °C and observing potential positive impacts on sample crystallinity (Talla et al., 2011).

Methods involving cellulose reactions include positioning a PET mesh on the surface of a casting solution containing cellulose acetate, resulting in a composite with good mechanical strength (Li et al., 2016). Carboxymethylated cellulose nanofibrils demonstrated efficacy in removing cupric ions from water (Qin et al., 2019). Utilizing CNC aqueous suspension methods, applying a CNC coating on PET surfaces enhanced water vapor barrier properties and controllable hydrophobicity (Lei et al., 2018).

Similar methods have been employed to produce cellulose-PET nanopaper, which demonstrated enhanced mechanical properties (Desmaisons et al., 2018). An advanced method, utilizing a high-frequency homogenizer and vacuum filtration, resulted in a PET/CNF film four times stronger than the CNF film (itself), showcasing improved tensile stress.

In TFA-based methods, cellulose and PET were dissolved in TFA and films were dried at room temperature for 24 hours with different mass ratios (Field and Song, 1984). These films, analyzed by DSC, revealed that cellulose or associated water-nucleated PET crystallization with melting points at a maximum 254 °C (Field and Chien, 1985).

In summary, these diverse methods offer opportunities to tailor cellulose/PET

composites with enhanced mechanical, thermal, and barrier properties. Each method presents its own advantages and challenges, necessitating further research to optimize them for specific applications and explore novel techniques addressing current limitations in cellulose/PET composite synthesis.

1.2 Biomass Derivatives

5-(Chloromethyl)furfural (CMF), derived from renewable sources such as agricultural wastes, holds significant potential due to the interest in its derivatives (Mascal, 2015, 2019). Likewise, 2,5-diformylfuran (DFF), derived from biomass, exhibits synthetic versatility with its two formyl groups, making it a valuable precursor for various materials and fine chemicals (Figure 2). The study of DFF's synthesis, reactivity, and applicationspromotes sustainable processes and innovative material development with broad impacts.
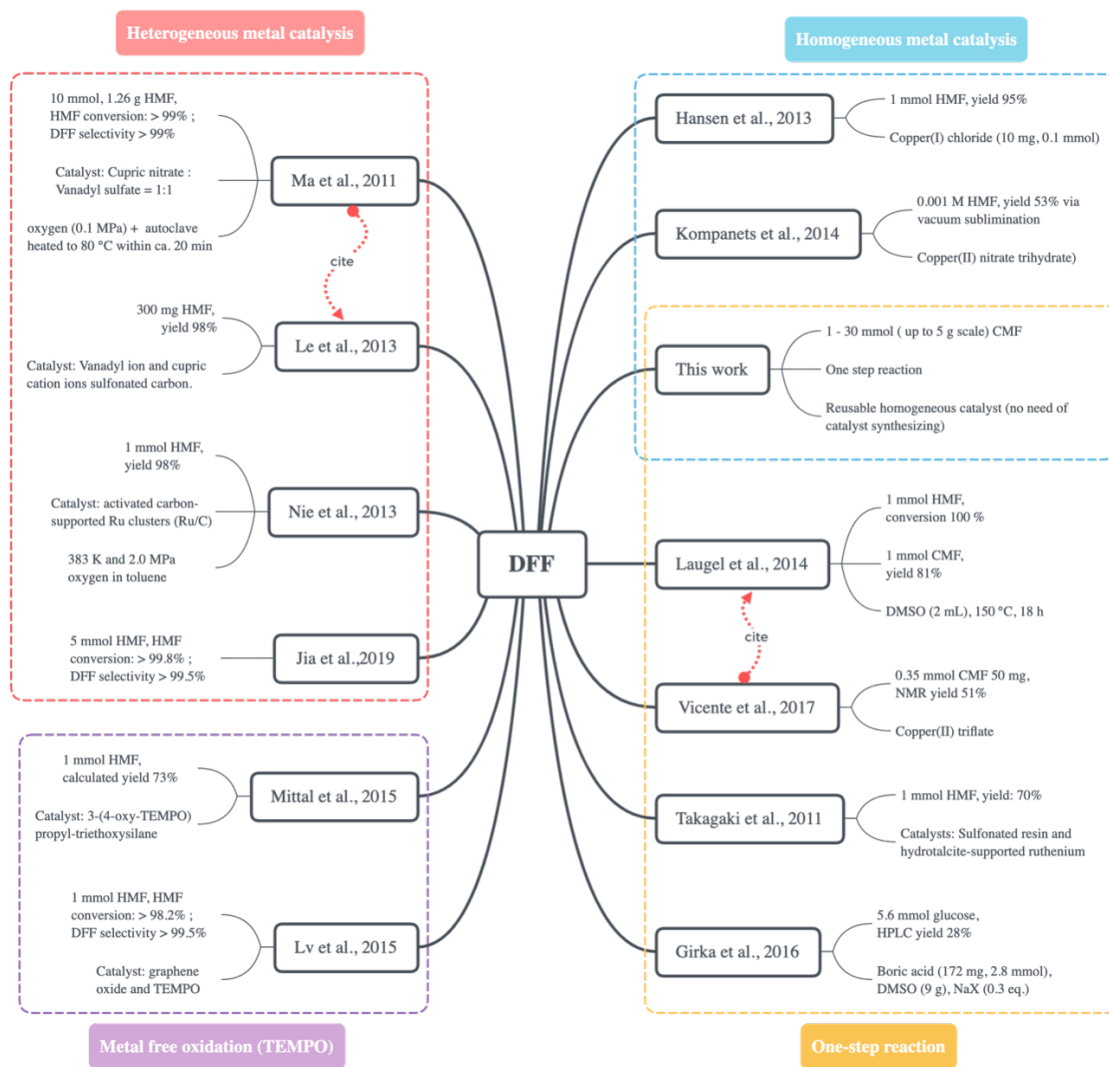
Figure 1.4: Graphical literature map describing DFF synthesis.

Several methods have been described for synthesizing DFF from 5-(hydroxymethyl)furfural (HMF) via selective oxidation, and these are summarized in Figure 1.4. Initial investigations into homogeneous metal catalysis resulted in a 42% DFF yield (Hansen et al., 2013). Another HMF oxidation using with N-hydroxyphthalimide and $Cu(NO)_3)_2 \cdot 3H_2O$ achieved a 53% DFF yield (Kompanets et al., 2014).

Efforts to enhance DFF yield later shifted towards heterogeneous metal catalyst
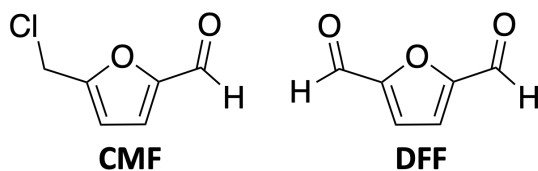
Figure 1.5: Structure of 5-(chloromethyl)furfural (CMF) and 2,5-diformylfuran (DFF).

systems, showing more promise. Notably, a combination of copper(II) nitrate and vanadyl sulfate resulted in 99% conversion of HMF on a 10 mmol scale (oxidant: oxygen gas), though the isolated yield was unspecified (Ma et al., 2011). A catalyst involving sulfonated carbon with surface-bound cupric ions achieved a 98% yield in DFF oxidation (oxidant: oxygen gas) at 140 °C for 4 hours (Le et al., 2013). Incorporating metals like Ru onto activated carbon achieved a 96% yield HMF at 383 K (Nie et al., 2013). Metal-free oxidation methods, primarily using TEMPO, achieved a maximum isolated yield of 50.2% (Mittal et al., 2014). Optimization of this method using a 3-(4-oxy-TEMPO)propyl-triethoxysilane (bis(acetoxy) iodo]benzene (BAIB) catalyst in an oxygen-rich environment) increased the HPLC yield to 73% (Mittal et al., 2015). Another case involving TEMPO oxidation (co-oxidant oxygen gas), employing graphene oxide to increase the catalyst's surface area, achieved a conversion of more than 98.2% and a selectivity to DFF of more than 99.5%, although the isolated yield was not mentioned (Lv et al., 2015).

Recent developments have explored a one-step reaction approach predominantly on a small scale (1 mmol HMF). Oxidation with sodium bromide and DMSO at 150 °C for 18 hours gave an 81% yield (Laugel et al., 2014). Various catalyst systems building upon this DMSO oxidation method have been explored with glucose. The most notable yield, calculated by HPLC 28% under conditions of NaBr, formic acid and a reaction time of 17 hours (Girka et al., 2016). Another one-step synthesis involved the reaction of CMF with copper(II) triflate in acetonitrile at 160 °C under microwave irradiation,

resulting in an NMR yield of 51% (Vicente et al., 2017). The catalyst combination of a sulfonated resin and hydrotalcite-supported ruthenium achieved a yield of 70% with a selectivity of 82% (Takagaki et al., 2011). Despite these advancements, the primary limitation in the current landscape of DFF synthesis is its confinement to small scales (1-3 mmol). Scalability poses significant challenges, and larger-scale reactions generally yield poor results.

1.3 Summary of Work during Ph.D.

Throughout my doctoral research, diverse facets of green chemistry have been explored (Scheme 1). These have encompassed the repurposing of waste plastic bottles by nanocompositing with cellulose nanocrystals which are conveniently sourced from wastes such as rice straw or wood pulp (Chapter 2). Additionally, work in this thesis also involves the characterization of sustainable organic dyes, with a focus on evaluating and comparing their color fastness (Chapter 3). Finally, an integral component of the research here was the optimization of DFF synthesis, with the overarching goal of establishing an efficient and more environmentally friendly synthetic route (Chapter 4).
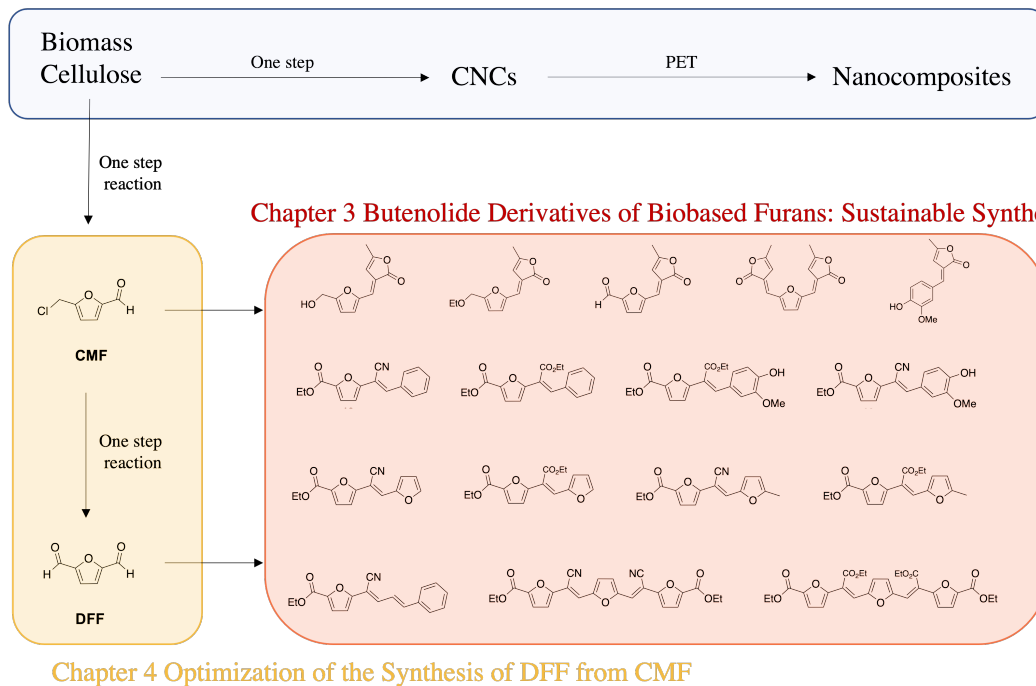
Scheme 1: Summary of work in this thesis.

References

Revol, J.-F., Godbout, L., Dong, X.-M., Gray, D. G., Chanzy, H., & Maret, G. (1994). Chiral nematic suspensions of cellulose crystallites; phase separation and magnetic field orientation. *Liquid Crystals*, *16*(1), 127–134.

Dong, X. M., Revol, J.-F., & Gray, D. G. (1998). Effect of microcrystallite preparation conditions on the formation of colloid crystals of cellulose. *Cellulose*, *5*, 19–32.

Yu, H., Qin, Z., Liang, B., Liu, N., Zhou, Z., & Chen, L. (2013). Facile extraction of thermally stable cellulose nanocrystals with a high yield of 93% through hydrochloric acid hydrolysis under hydrothermal conditions. *Journal of Materials Chemistry A*, *1*(12), 3938–3944.

Camarero Espinosa, S., Kuhnt, T., Foster, E. J., & Weder, C. (2013). Isolation of thermally stable cellulose nanocrystals by phosphoric acid hydrolysis. *Biomacromolecules*, *14*(4), 1223–1230.

Braun, B., Dorgan, J. R., & Hollingsworth, L. O. (2012). Supra-molecular ecobionanocomposites based on polylactide and cellulosic nanowhiskers: Synthesis and properties. *Biomacromolecules*, *13*(7), 2013–2019.

Spinella, S., Maiorana, A., Qian, Q., Dawson, N. J., Hepworth, V., McCallum, S. A., Ganesh, M., Singer, K. D., & Gross, R. A. (2016). Concurrent cellulose hydrolysis and esterification to prepare a surface-modified cellulose nanocrystal decorated with carboxylic acid moieties. *ACS Sustainable Chemistry & Engineering*, *4*(3), 1538–1550.

Mahmoud, K. A., Mena, J. A., Male, K. B., Hrapovic, S., Kamen, A., & Luong, J. H. (2010). Effect of surface charge on the cellular uptake and cytotoxicity of fluorescent labeled cellulose nanocrystals. *ACS applied materials & interfaces*, *2*(10), 2924–2932.

Endes, C., Mueller, S., Kinnear, C., Vanhecke, D., Foster, E. J., Petri-Fink, A., Weder, C., Clift, M. J., & Rothen-Rutishauser, B. (2015). Fate of cellulose nanocrystal aerosols deposited on the lung cell surface in vitro. *Biomacromolecules*, *16*(4), 1267–1275.

Yang, X., Bakaic, E., Hoare, T., & Cranston, E. D. (2013). Injectable polysaccharide hydrogels reinforced with cellulose nanocrystals: Morphology, rheology, degradation, and cytotoxicity. *Biomacromolecules*, *14*(12), 4447–4455.

Wang, K., Nune, K., & Misra, R. (2016). The functional response of alginate-gelatin-nanocrystalline cellulose injectable hydrogels toward delivery of cells and bioactive molecules. *Acta biomaterialia*, *36*, 143–151.

Chen, Q., Garcia, R. P., Munoz, J., Pérez de Larraya, U., Garmendia, N., Yao, Q., & Boccaccini, A. R. (2015). Cellulose nanocrystals bioactive glass hybrid coating as bone substitutes by electrophoretic co-deposition: In situ control of mineralization of bioactive glass and enhancement of osteoblastic performance. *ACS applied materials & interfaces*, *7*(44), 24715–24725.

Shi, Z., Tang, J., Chen, L., Yan, C., Tanvir, S., Anderson, W. A., Berry, R. M., & Tam, K. C. (2015). Enhanced colloidal stability and antibacterial performance of silver nanoparticles/cellulose nanocrystal hybrids. *Journal of Materials Chemistry B*, *3*(4), 603–611.

Wang, S., Sun, J., Jia, Y., Yang, L., Wang, N., Xianyu, Y., Chen, W., Li, X., Cha, R., & Jiang, X. (2016). Nanocrystalline cellulose-assisted generation of silver nanoparticles for nonenzymatic glucose detection and antibacterial agent. *Biomacromolecules*, *17*(7), 2472–2478.

Dong, S., & Roman, M. (2007). Fluorescently labeled cellulose nanocrystals for bioimaging applications. *Journal of the American Chemical Society*, *129*(45), 13810–13811.

Schyrr, B., Pasche, S., Voirin, G., Weder, C., Simon, Y. C., & Foster, E. J. (2014). Biosensors based on porous cellulose nanocrystal–poly (vinyl alcohol) scaffolds. *ACS applied materials & interfaces*, *6*(15), 12674–12683.

Dong, S., Cho, H. J., Lee, Y. W., & Roman, M. (2014). Synthesis and cellular uptake of folic acid-conjugated cellulose nanocrystals for cancer targeting. *Biomacromolecules*, *15*(5), 1560–1567.

Akhlaghi, S. P., Tiong, D., Berry, R. M., & Tam, K. C. (2014). Comparative release studies of two cationic model drugs from different cellulose nanocrystal derivatives. *European Journal of Pharmaceutics and Biopharmaceutics*, *88*(1), 207–215.

Wang, H., He, J., Zhang, M., Tam, K. C., & Ni, P. (2015). A new pathway towards polymer modified cellulose nanocrystals via a "grafting onto" process for drug delivery. *Polymer Chemistry*, *6*(23), 4206–4209.

Benhamou, A., Boussetta, A., Grimi, N., Idrissi, M. E., Nadifiyine, M., Barba, F. J., & Moubarik, A. (2022). Characteristics of cellulose fibers from opuntia ficus indica cladodes and its use as reinforcement for pet based composites. *Journal of Natural Fibers*, *19*(13), 6148–6164.

Kiziltas, A., Gardner, D. J., Han, Y., & Yang, H.-S. (2011). Thermal properties of microcrystalline cellulose-filled pet–ptt blend polymer composites. *Journal of thermal analysis and calorimetry*, *103*(1), 163–170.

Talla, A. F., Erchiqui, F., & Godard, F. (2011). Thermal properties and stability of pet-hemp fibres composites. *Proceedings of the 19th International Conference on Composite Materials*.

Li, G., Wang, J., Hou, D., Bai, Y., & Liu, H. (2016). Fabrication and performance of pet mesh enhanced cellulose acetate membranes for forward osmosis. *Journal of Environmental Sciences*, *45*, 7–17.

Qin, F., Fang, Z., Zhou, J., Sun, C., Chen, K., Ding, Z., Li, G., & Qiu, X. (2019). Efficient removal of cu2+ in water by carboxymethylated cellulose nanofibrils: Performance and mechanism. *Biomacromolecules*, *20*(12), 4466–4475.

Lei, W., Fang, C., Zhou, X., Yin, Q., Pan, S., Yang, R., Liu, D., & Ouyang, Y. (2018). Cellulose nanocrystals obtained from office waste paper and their potential application in pet packing materials. *Carbohydrate Polymers*, *181*, 376–385.

Desmaisons, J., Gustafsson, E., Dufresne, A., & Bras, J. (2018). Hybrid nanopaper of cellulose nanofibrils and pet microfibers with high tear and crumpling resistance. *Cellulose*, *25*, 7127–7142.

Field, N. D., & Song, S. S. (1984). Blends of poly (ethylene terephthalate) and cellulose. *Journal of Polymer Science: Polymer Physics Edition*, *22*(1), 101–106.

Field, N. D., & Chien, M.-C. (1985). Poly (ethylene terephthalate)/cellulose blends. *Journal of applied polymer science*, *30*(5), 2105–2113.

Mascal, M. (2015). 5-(chloromethyl)furfural is the new hmf: Functionally equivalent but more practical in terms of its production from biomass. *ChemSusChem*, *8*(20), 3391–3395.

Mascal, M. (2019). 5-(chloromethyl)furfural (cmf): A platform for transforming cellulose into commercial products. *ACS Sustainable Chemistry & Engineering*, *7*(6), 5588–5601.

Hansen, T. S., Sádaba, I., García-Suárez, E. J., & Riisager, A. (2013). Cu catalyzed oxidation of 5-hydroxymethylfurfural to 2,5-diformylfuran and 2,5-furandicarboxylic acid under benign reaction conditions. *Applied Catalysis A: General*, *456*, 44–50.

Kompanets, M., Kushch, O., Litvinov, Y. E., Pliekhov, O., Novikova, K., Novokhatko, A., Shendrik, A., Vasilyev, A., & Opeida, I. (2014). Oxidation of 5-hydroxymethylfurfural to 2,5-diformylfuran with molecular oxygen in the presence of n-hydroxyphthalimide. *Catalysis Communications*, *57*, 60–63.

Ma, J., Du, Z., Xu, J., Chu, Q., & Pang, Y. (2011). Efficient aerobic oxidation of 5-hydroxymethylfurfural to 2,5-diformylfuran, and synthesis of a fluorescent material. *ChemSusChem*, *4*(1), 51–54.

Le, N.-T., Lakshmanan, P., Cho, K., Han, Y., & Kim, H. (2013). Selective oxidation of 5-hydroxymethyl-2-furfural into 2,5-diformylfuran over vanadyl ion and copper(ii) ion immobilized on sulfonated carbon catalysts. *Applied Catalysis A: General*, *464*, 305–312.

Nie, J., Xie, J., & Liu, H. (2013). Efficient aerobic oxidation of 5-hydroxymethylfurfural to 2,5-diformylfuran on supported ru catalysts. *Journal of catalysis, 301*, 83–91.

Mittal, N., Nisola, G. M., Malihan, L. B., Seo, J. G., Lee, S.-P., & Chung, W.-J. (2014). Metal-free mild oxidation of 5-hydroxymethylfurfural to 2,5-diformylfuran. *Korean Journal of Chemical Engineering, 31*, 1362–1367.

Mittal, N., Nisola, G. M., Seo, J. G., Lee, S.-P., & Chung, W.-J. (2015). Organic radical functionalized sba-15 as a heterogeneous catalyst for facile oxidation of 5-hydroxymethylfurfural to 2,5-diformylfuran. *Journal of Molecular Catalysis A: Chemical, 404*, 106–114.

Lv, G., Wang, H., Yang, Y., Deng, T., Chen, C., Zhu, Y., & Hou, X. (2015). Graphene oxide: A convenient metal-free carbocatalyst for facilitating aerobic oxidation of 5-hydroxymethylfurfural into 2,5-diformylfuran. *Acs Catalysis, 5*(9), 5636–5646.

Laugel, C., Estrine, B., Le Bras, J., Hoffmann, N., Marinkovic, S., & Muzart, J. (2014). Sodium Bromide DMSO-Induced Synthesis of 2,5-Diformylfuran from Fructose or 5-(Hydroxymethyl) furfural. *ChemCatChem, 6*(5), 1195–1198.

Girka, Q., Estrine, B., Hoffmann, N., Le Bras, J., Marinković, S., & Muzart, J. (2016). Simple efficient one-pot synthesis of 5-hydroxymethylfurfural and 2,5-diformylfuran from carbohydrates. *Reaction Chemistry & Engineering, 1*(2), 176–182.

Vicente, A. I., Coelho, J. A., Simeonov, S. P., Lazarova, H. I., Popova, M. D., & Afonso, C. A. (2017). Oxidation of 5-chloromethylfurfural (cmf) to 2,5-diformylfuran (dff). *Molecules, 22*(2), 329.

Takagaki, A., Takahashi, M., Nishimura, S., & Ebitani, K. (2011). One-pot synthesis of 2,5-diformylfuran from carbohydrate derivatives by sulfonated resin and hydrotalcite-supported ruthenium catalysts. *ACS Catalysis, 1*(11), 1562–1565.

2 Trifluoroacetic Acid as an Effective Dispersing Medium for Cellulose Nanocrystals

2.1 Introduction

Cellulose nanocrystals (CNCs) serve as a sustainable platform for a variety of cutting-edge technical applications including in biomedical engineering (Mahmoud et al., 2010), antimicrobial/antiviral systems (Mahmoud et al., 2010), tissue engineering (Domingues et al., 2014), biosensors (Dong and Roman, 2007), drug/gene delivery (Akhlaghi et al., 2014), and the energy and electronics sector (Chen et al., 2018). Their abundance, unique morphology, low toxicity, low density, high modulus, chirality, ability to self-assemble, and versatility for chemical manipulation suggest that the current applications are only the beginning of a nascent nanotechnological revolution based around these materials.

The standard method of generating uniform CNCs from cellulose or pre-treated pulps involves partial hydrolysis with 64% aqueous sulfuric acid at 45 °C for up to 2 h followed by quenching into water. The CNCs produced by this process are partially sulfated (*ca.* one sulfate half-ester for every 2-3 surface anhydroglucose units) (Chaka, 2022; Reid et al., 2017) which aids dispersion of the particles in aqueous media. Yields however are moderate, and the method is water-intensive, involves laborious purification steps, and generates sulfuric acid waste that cannot be easily recycled. A common alternative is hydrolysis with aqueous hydrochloric acid, which has been tested across a range of concentrations and reaction intensities. This approach has the major advantage of leaving the surface of the CNC unmodified. Multiple studies from the mid-20th century and onward point to rapid initial hydrolysis of amorphous or "defect" regions, leaving behind a crystalline material that proceeds to hydrolyze

more slowly, first to cellodextrins (Zhang & Lynd, 2003), and ultimately to glucose. Regardless of the severity of the process, the degree of polymerization quickly plateaus to values in a range between 150-300, pointing to a possible explanation for the origin of CNCs by the so-called fringed-fibrillar model, although the details of the mechanism remain a matter of debate (Kontturi, 2018).

Recently, Kontturi and coworkers described a remarkably simple, mild, and efficient method for producing high-quality CNCs by the action of gaseous hydrogen chloride on cellulose in the form of commercial filter paper (Kontturi et al., 2016). Hydrolysis takes place by means of ambient water that is absorbed onto the cellulose surface, and the yield of nanocrystalline cellulose approaches quantitative. The process has been upgraded from being conducted in a vacuum desiccator to a dedicated reactor that uses pressurized hydrogen chloride, which decreases the reaction time from 12-24 hours to 1.5 hours (Pääkkönen et al., 2018).

As discussed in Chapter 1, a mainstream application of nanocellulose is the production of nanocomposites with polymers (Gomri et al., 2022). In nature, the archetypal polymer composite is generated between cellulose and lignin, which are chemically connected via ether, ester, and glycosidic bonds (Tarasov et al., 2018). However, the challenge associated with generating composites of cellulose with synthetic materials is the lack of functional compatibility and therefore weak interfacial adhesion, particularly with hydrophobic polymers. Various cellulose surface modification schemes have been developed in order to address this matter (Siró & Plackett, 2010). Such practices, however, significantly increase the complexity of the overall process and the cost of the resulting material. One common approach involves 2,2,6,6-tetramethyl-piperidine-1-oxyl radical (TEMPO)-mediated oxidation of cellulose, which results in up to 50% of the surface anhydroglucose 6-OH groups being oxidized to the glucuronic acids, enabling the formation of stable nanoparticle suspensions in water (Saito et

al., 2007; Lin et al., 2011). Likewise, CNCs with highly sulfated surfaces are able to form dilute suspensions in water or wet, polar organic solvents like DMF and DMSO (Viet et al., 2007). As an alternative to this approach, many investigators have turned to physico-chemical means to intersperse various forms of cellulose with a range of polymers, which include solution casting, melt-processing, and electrospinning (Kargarzadeh et al., 2017). The general use of such methods however often involves specialized homogenization techniques and high temperatures (250 °C).

Polyethylene terephthalate (PET) is one of the highest volume commercial thermoplastics due to its strength, thermal stability, chemical resistance, transparency, and barrier properties. However, its crystallinity, low wettability, and poor adhesive properties make blending with cellulose a challenge. Hence, decorating the cellulose surface with hydrophobic groups, usually alkyl esters and ethers, has proved useful in working around this problem (Chaka, 2022; Huang et al., 2015). While the literature on native cellulose-PET composite production is highly relevant and bears detailed discussion at this point, the intersection of answer sets between the terms "PET" and "cellulose" in *Chemical Abstracts* gives a large number of hits that cannot all be addressed here. For convenience, a graphical overview of selected works has been produced which can be found in Figure 1.3 along with the related literature.

Finally, despite the advances in the production of CNCs, their suspension in common organic media for the purposes of composite generation remains a challenge (Lorenz et al., 2017). Ultimately, for industrial-scale applications, the objective would be to achieve a dispersion of native CNCs in an organic solvent without having to modify the surface. To date, the only method, to our knowledge, which has seen some measure of success involves prolonged (72 h) sonication of CNCs in concentrated aqueous formic acid (Kontturi et al., 2016; Van den Berg et al., 2007). In this Chapter, we describe the instantaneous formation of metastable suspensions of CNCs in trifluo-

roacetic acid, a volatile organic solvent that is miscible with most organic solvents as well as water. Aging the mixtures leads to stable dispersions with associated changes in viscosity and transparency as the CNCs increasingly deflocculate and the surface of the nanocrystal is partially trifluoroacylated.

2.2 Experimental

2.2.1 Cellulose Nanocrystal Production

CNCs were prepared using the gaseous hydrogen chloride method described by Kontturi and coworkers (Kontturi et al., 2016). The resulting fine white powder was found to instantaneously form opaque suspensions on mixing with anhydrous trifluoroacetic acid (TFA) at a CNC loading of 20 mg mL^{-1}. Samples for spectroscopic analysis were prepared by suspending CNCs (200 mg) in TFA (10 mL) and quenching into water (200 mL) after 1 min, 30 min, 1 h, 6 h, 12 h, 24 h, 48 h, and 72 h. The resulting precipitates were filtered and washed with deionized water and then ether. The solids were dried under vacuum overnight prior to analysis. Mass recovery in all cases was in the range of 90-100%.

2.2.2 Composite Film Preparation

Pieces of colorless PET (2-5 mm square, 900 mg) sourced from a commercial water bottle were washed with ethanol and air-dried. To this was added CNCs (100 mg) and the mixture was stirred in TFA (10 mL) for either 24, 48, or 72 h. The resulting homogeneous suspensions were poured into a glass dish in a fume hood and films were seen to form as the TFA evaporated over the course of about 30 min. Deionized water (20 mL) was then added to wash out any remaining TFA and the resulting white films were collected and dried between several layers of tissue paper for 2 h under a load of

5 kg, followed by air drying in a fume hood overnight. Control films containing only PET were produced by stirring the samples of the same PET (900 mg) in TFA (10 mL) for the same periods of time and drying under the same conditions. A second control group was generated by stirring cellulose nanocrystals (100 mg) in TFA (10 mL) for either 24, 48, or 72 h and then adding the PET pieces (900 mg) in the last 5 min of the time period.

2.2.3 Transmission Electron Microscopy (TEM) and Atomic Force Microscopy (AFM) Imaging

TEM imaging was performed on a JEOL 1230 transmission electron microscope operating at 100 kV accelerating voltage. CNC-TFA suspensions (2.5 µL) collected at various time points were diluted to 0.0005 wt% with fresh TFA, deposited onto glow-discharged carbon-coated TEM grids, and negatively stained with 2% uranyl acetate solution for 5 min. AFM imaging was performed on an Asylum Research atomic force microscope with a silicon probe (f = 70 KHz) in tapping mode at a scan rate of 0.8 Hz/second. CNC-TFA suspensions (2.5 µL) were diluted to 0.0005 wt% with fresh TFA and deposited onto freshly clipped mica substrates.

2.2.4 Thermogravimetric Analysis (TGA)

TGA data were measured using a Shimadzu TGA-50 thermogravimetric analyzer. Precipitated solids (5 mg) from CNC-TFA suspensions collected at various time points were characterized under nitrogen from room temperature to 450 °C at a heating rate of 10 °C min^{-1}.

2.2.5 Fourier Transform Infrared Spectroscopy (FT-IR)

FTIR spectra were measured on a Nicolet 6700 FTIR spectrophotometer (Thermo Electron Corporation) with 4 cm^{-1} resolution. Precipitated solids (5 mg) from CNC-TFA suspensions collected at various time points were analyzed in KBr wafers.

2.2.6 Cross Polarization-Magic Angle Spinning Nuclear Magnetic Resonance Spectroscopy (CP-MAS NMR)

Solid-state ^{13}CP-MAS NMR was carried out on a Bruker AVANCE 500 MHz spectrometer equipped with an 11.7 Tesla wide bore magnet. 1.0 g of precipitated solids from CNC-TFA suspensions were used for all measurements.

2.2.7 Surface Electron Microscopy (SEM) and Brunauer-Emmett-Teller (BET) Adsorption Isotherm Analysis

SEM was performed using a Hitachi S-4100 T scanning electron microscope. A dry composite film (900 mg, CNC:PET=1:10, 10 mL TFA, aged 72 h) and a control film (900 mg PET, 10 mL TFA, aged 72 h) were coated with gold and imaged. BET data was collected using a Micromeritics ASAP2020 Absorption Analyzer. The films were degassed at room temperature (RT) for 18 h prior to analysis.

2.2.8 X-ray Diffraction (XRD)

XRD measurements were performed on a D8 ADVANCE powder diffractometer. The diffracted intensity of Cu radiation (40 kV and 25 mA) was measured in a 2θ range between 10° and 80°.

2.3 Results and Discussion

2.3.1 Production of CNC suspensions

It was found that over the course of 72 h, the initially turbid, free-flowing suspensions of CNCs and TFA became increasingly viscous and gradually clarified (Figure 2.1). Suspensions at early time points were initially homogeneous but proved to be metastable and showed a gradual settling behavior, which could be delayed by heating at 60 °C. The mixture remained fully homogenous after 2 h and slowly began to clarify (Table 1).
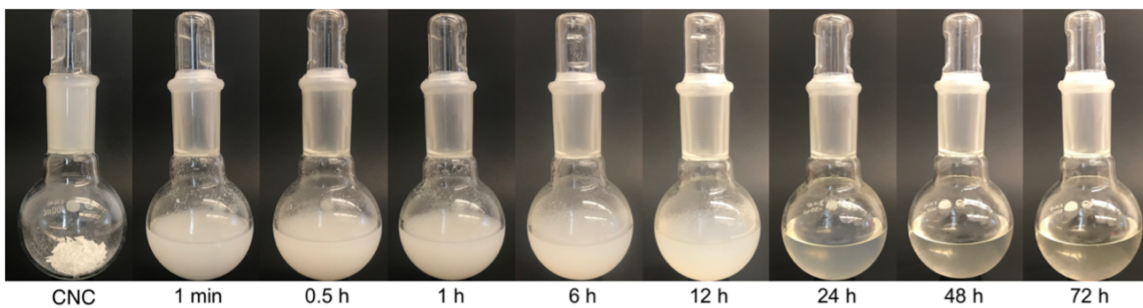

Figure 2.1: The CNC sample and suspensions of CNCs (200 mg) in TFA (10 mL) at the stated time points.

A CNC sample (3 mg) stirred in TFA (3 mL) for 24 h was used for measurement of the Tyndall effect (Stainmesse et al., 1995), which was observed at each stated time point from 0 min to 5 days. A red laser beam showed no settling behavior in a 24-hour CNC-TFA mixture (Figure 2.2). After another 24-hour period, the effect diminished, and was virtually absent after 5 days, indicating no particles larger than 50 nm remained in the suspension.

Table 1: Settling behaviors of cellulose nanocrystals in TFA at RT and 60 °C vs time.

	5 min	15 min	30 min	1 h	2h	4h	6h	12h
RT	<10 min	<10 min	<10 min	>10 min	NS	NS	NS	ST
60 °C	<10 min	>10 min	>10 min	>30 min	NS	NS	NS	ST
NS = no settling observed, ST = no settling and semi-transparent								
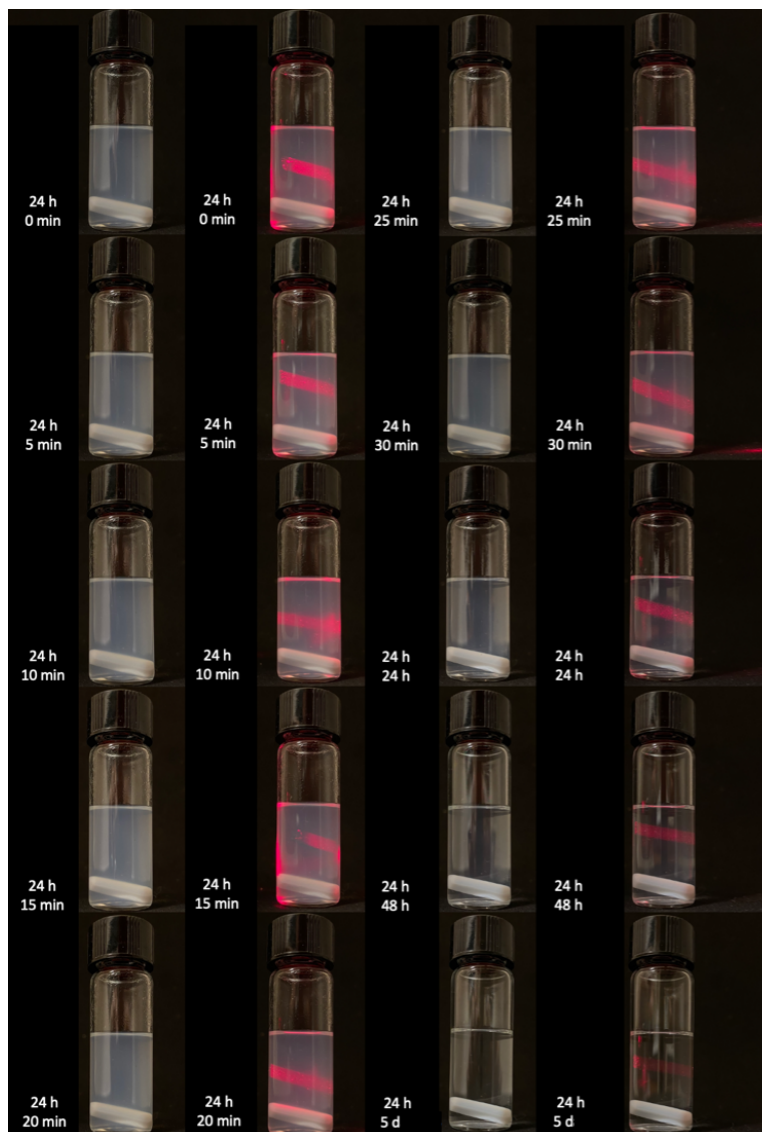
Figure 2.2: CNC-TFA suspension Tyndall Effect observations. Samples were stirred for 24 h. The bottom number refers the amount of time after stirring was stopped, at which point the observation was made.

2.3.2 TEM and AFM Analysis

In the TEM, bundles of CNCs are observed at t=0 and subsequent early time points. Over the duration of the aging process, needle-shaped nanocrystals (length 145 ±43 nm; width 10 ±2 nm) were clearly seen separating from the bundles (Figure 2.3). Results from AFM imaging (Figure 2.4) generally agreed with the TEM results and showed both aggregates and the same needle-shaped CNCs (thickness 10.8 ±4 nm).
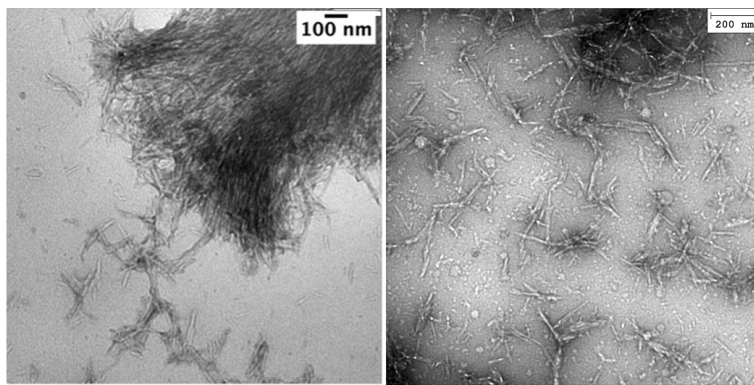

Figure 2.3: TEM images of aggregates of CNCs at t = 12 h (left) and individual, needle-like CNCs at t = 24 h (right).
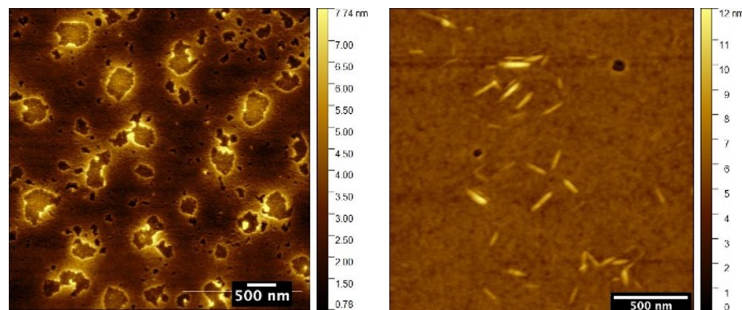

Figure 2.4: AFM images of CNCs at t = 0 h and individual (left), needle-like CNCs at t = 72 h (right).

2.3.3 Thermogravimetric Analysis

For TGA measurements (Figures 2.5 & 2.6), analysis of a freshly prepared CNC sample was used as a control. This is differentiated from the t = 0 sample, which had been suspended in TFA and quenched with deionized water after 1 min and isolated. Thermal degradation was evaluated from the first derivatives (midpoint) and from the tangents (onset, endset) of the weight loss curves (Figure 2.5 & Table 2). For the native CNC and t = 0 samples, initial minor weight loss up to 100 °C can be attributed to volatilization of adsorbed water. These two samples then underwent decomposition at the midpoint of the curves at ca. 340 °C, consistent with that of pure cellulose (Ramiah, 1970). Samples that were precipitated from TFA after 0.5 h up to 72 h showed increasingly pronounced mass losses between room temperature and the onset of decomposition. Samples from 0.5 h to 24 h underwent two-stage thermal decompositions. In comparison, the t = 48 h and 72 h samples again had single-stage decompositions, but over a broader range and with a midpoint ca. 50 °C lower than the native CNC and t = 0 samples. While the second stage decomposition of the t = 0.5 h, 1 h, 6 h, and 12 h samples roughly correlated to those of the control and t = 0 samples, the first stage had an onset of decomposition between 240-250 °C. This supports the IR and NMR data (Section 2.4.1) which indicate that the CNCs are being modified by increasing acylation with time. The intermediate samples at t = 0.5, 1, 6, and 12 h appear to contain two populations of CNCs; those that largely resemble native cellulose and follow the thermal decomposition path of the control samples, and those that approximately follow the thermal decomposition paths of t = 48 h and 72 h samples.
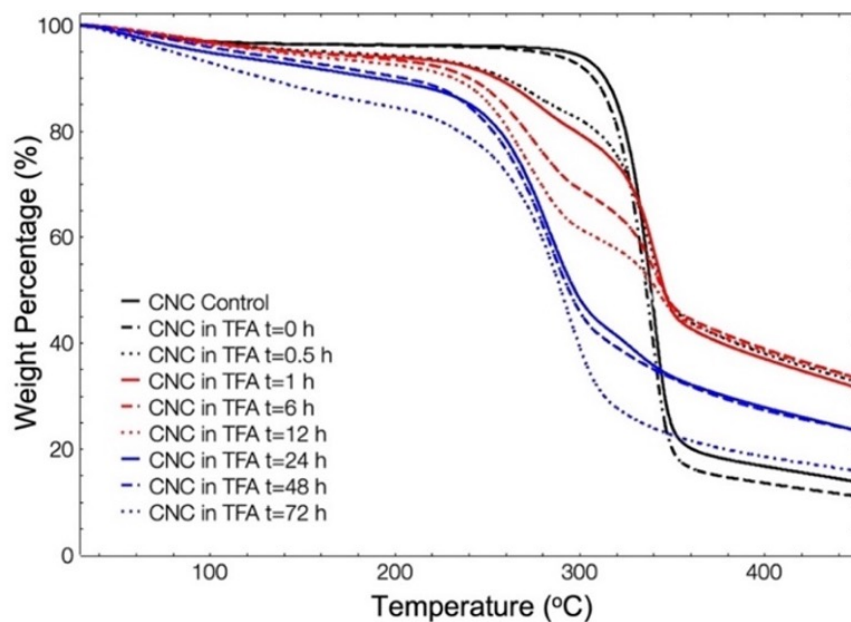
Figure 2.5: TGA curves for CNC samples isolated from suspensions in TFA at the stated time points.
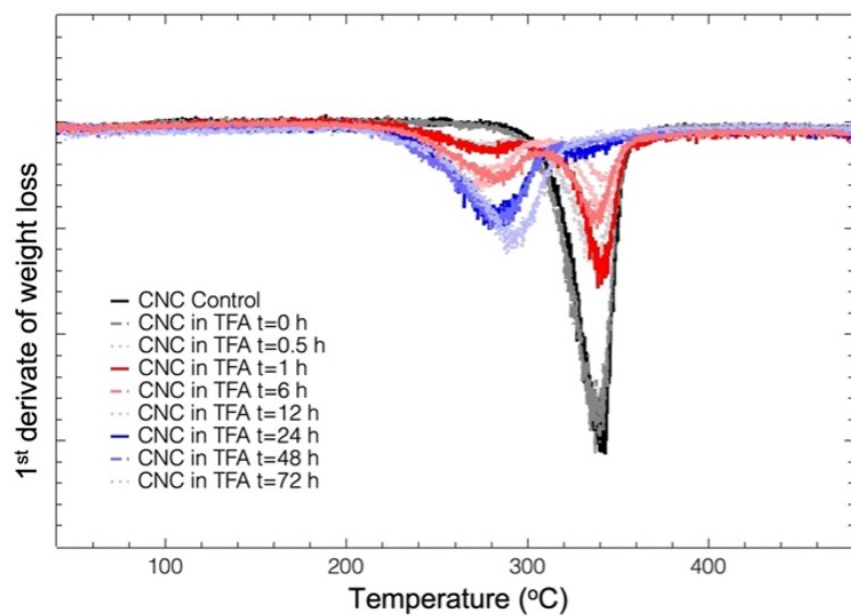

Figure 2.6: TGA derivatives for CNC samples isolated from suspensions in TFA at the stated time points.

Table 2: Thermal analysis of CNC samples isolated from suspensions in TFA at the stated time points. To = onset time; Tm = midpoint time, Te = endpoint time.

Time (h)	Stage 1		Stage 2			Weight Loss
	To1 (°C)	Tm1 (°C)	To2 (°C)	Tm2 (°C)	Te (°C)	(%)
CNC	–	–	324	341	350	90
0	–	–	320	340	348	93
0.5	248	–	322	337	350	73
1.0	245	–	329	341	351	75
1.5	254	285	327	337	347	78
6.0	244	275	329	341	350	72
12.0	244	273	332	342	352	78
24.0	256	–	–	284	309	83
48.0	252	–	–	284	313	81
72.0	264	–	–	291	315	88

It is known that bulk cellulose will form solutions in TFA over the course of several hours to several days, depending on the degree of crystallinity (Hasegawa et al., 1992; Geddes, 1956). However, it is not the cellulose itself, but C6-O-trifluoroacetylated cellulose that ultimately dissolves (Salin et al., 1993). The reaction is autocatalytic due to the high acidity of TFA (pka $\approx$ 0.5 in H_2O), and we observe the same phenomenon here at the crystal surface on extended standing of the suspensions. Along these lines, we were particularly intrigued by a report which found that cotton linter cellulose was decrystallized in TFA at a higher rate at 0 °C than at 25 °C (Zhao et al., 2007). We accordingly repeated our standard dispersion test (Section 2.2.1) on our CNCs at 0 °C. However, we saw no improvement in the ability of TFA to form suspensions at this temperature; in fact, as expected, the settling time was somewhat reduced. Although bulk cellulose (sisal) – PET nanocomposites have been prepared by electrospinning solutions of the two components in TFA (Santos et al., 2015), as far as we are aware, what we describe above is the first example of the use of CNCs in this context. Selected literature in this area is covered in Section 1.1.2 under Method: TFA.

2.4   Thermogravimetric Analysis of CNC-PET Composites

In the TGA of CNC-PET composite films, the degradation temperature increased slightly from 450 °C (original PET film) to 460 °C (CNC-PET film) (Table 3). However, whether the PET was stirred with cellulose for the entire time duration or only for the last 5 min, all CNC-PET films exhibited an early thermal degradation (261-288 °C) which differed both from control cellulose and control PET. Comparing the solid and dashed lines of the same color (Figure 2.7), when PET and CNCs were stirred together for the entire stated time duration, the product exhibited better stability than when PET was added in the last 5 min of the time period (dashed). This may be explained by the hypothesis that cellulose, or the water associated with it, nucleates the crystallization of the PET (Field & Chien, 1985). When nanocellulose (this study) was used instead of microcrystalline cellulose (literature), this appears to enhance the nucleation process and lead to higher thermal stability apparently due to higher crystallinity.
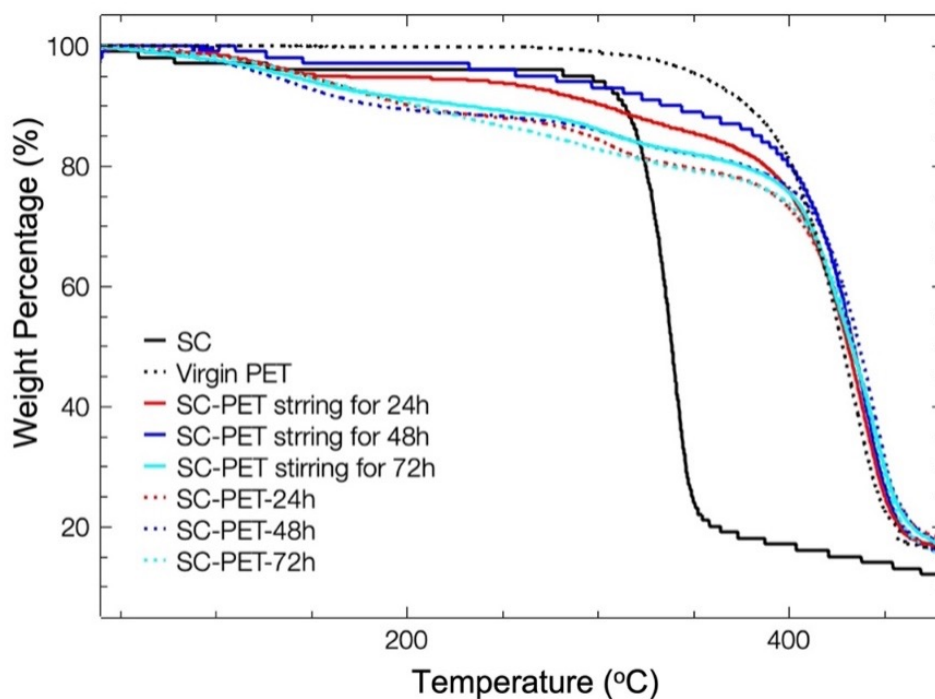
Figure 2.7: TGA curves for (1) solid black line: control CNC (SC); (2) dashed black line: bulk PET; (3) solid red line: control CNC + PET stirred together in TFA 24 h; (4) solid blue line: control CNC + PET stirred together in TFA 48 h; (5) solid cyano line: control CNC + PET stirred together in TFA 72 h; (6) dashed red line: control CNC in TFA 24 h with PET added in last 5 min; (7) dashed blue line: control CNC in TFA 48 h with PET added in last 5 min; (8) dashed cyano line: control CNC in TFA 72 h with PET added in last 5 min.

Table 3: Thermal analysis of TGA curves for CNC/PET film at the stated time points. SC control: the control group of cellulose nanocrystals only; Group 1-3: CNC-PET stirred together 24 h, 48 h, and 72 h; Group 4-6: SC-24h, 48h, 72h, stirred with PET for 5 min. To = onset temperature; Tm = midpoint temperature, Te = endpoint temperature

	To 1 (°C)	To 2 (°C)	Tm (°C)	Te (°C)
SC Control	NA	324	341	350
Virgin PET	NA	389	433	450
Group 1	261	409	442	458
Group 2	268	413	442	457
Group 3	283	405	444	458
Group 4	280	407	444	458
Group 5	288	419	445	459
Group 6	NA	413	444	458

2.4.1 Spectroscopic Analysis

Figure 2.8 shows stacked FT-IR spectra for CNCs in TFA at various time points. Characteristic peaks in all samples can be seen at 3433 cm^{-1}, 2898 cm^{-1}, and 1643 cm^{-1} for cellulose O-H stretching, C-H stretching, and O-H bending, respectively. The peaks found in the fingerprint region for the control CNC sample are also virtually superposable on literature spectrum of microcrystalline cellulose (Jia et al., 2011; Kassanov et al., 2017). The new peak at 1785 cm^{-1}, which is just observable in the t = 6 h sample and clearly visible at 72 h, is characteristic of the C=O function of a trifluoroacetate ester. Stacked CP-MAS ^{13}C-NMR plots of the control sample and the t = 72 h sample (Figure 2.9) also show new peaks for the trifluoroacetate ester C=O group at 160.1 ppm and the CF_3 quartet at 115.3 ppm. These peaks are consistent with literature NMR data for trifluoracylated cellulose (Hasegawa et al., 1992).
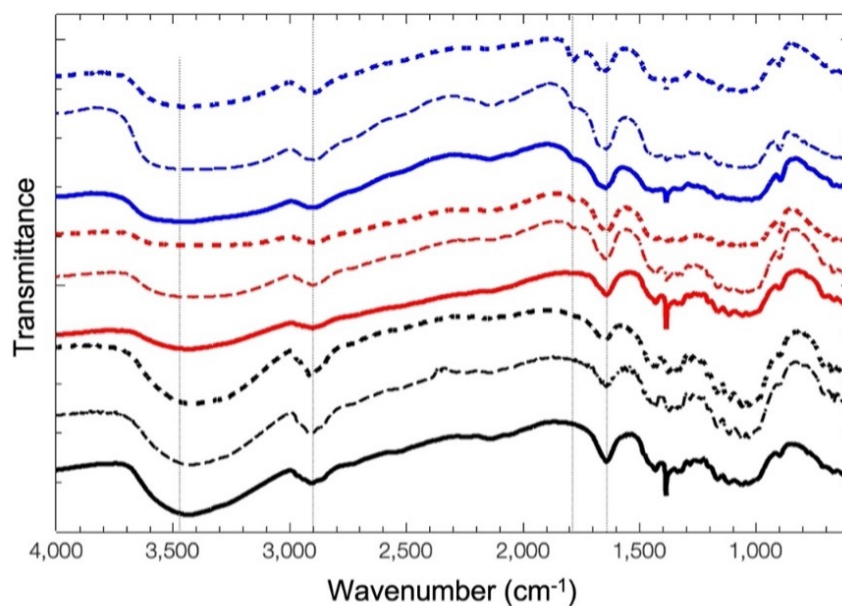
Figure 2.8: FT-IR spectra of control (black solid), t = 0 min (black single dashed), 0.5 h (black double dashed), 1 h (red solid), 6 h (red single dashed), 12 h (red double dashed), 24 h (blue solid), 48 h (blue single dashed), and 72 h (blue double dashed) CNC suspensions in TFA.
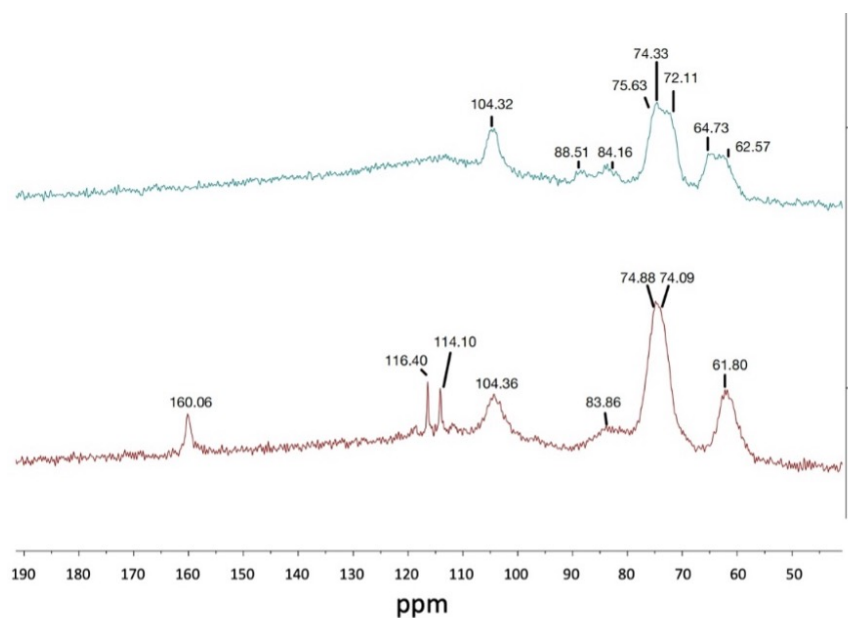

Figure 2.9: Solid-state CP-MAS 13C-NMR spectra of the control CNC sample (top) and t = 72 h sample isolated from the suspension in TFA (bottom).

33

2.4.2 X-Ray Diffraction Analysis

The evolution of the crystallinity of the CNCs with increasing suspension time in TFA was evaluated by XRD. Figure 2.10 shows the characteristic 2θ peak of control CNCs at 22.5°, which corresponds to the [002] crystal plane. This peak is observed to decrease with increasing time in TFA suspension, while a peak at 20.4°, which is reminiscent of the characteristic peak for cellulose trifluoroacetate (Cunha et al., 2007) grows in. The position of this peak indicates increased plane separation in the crystal, and its broadening suggests an inhomogeneous composition and/or increased disorder (Segal et al., 1959).
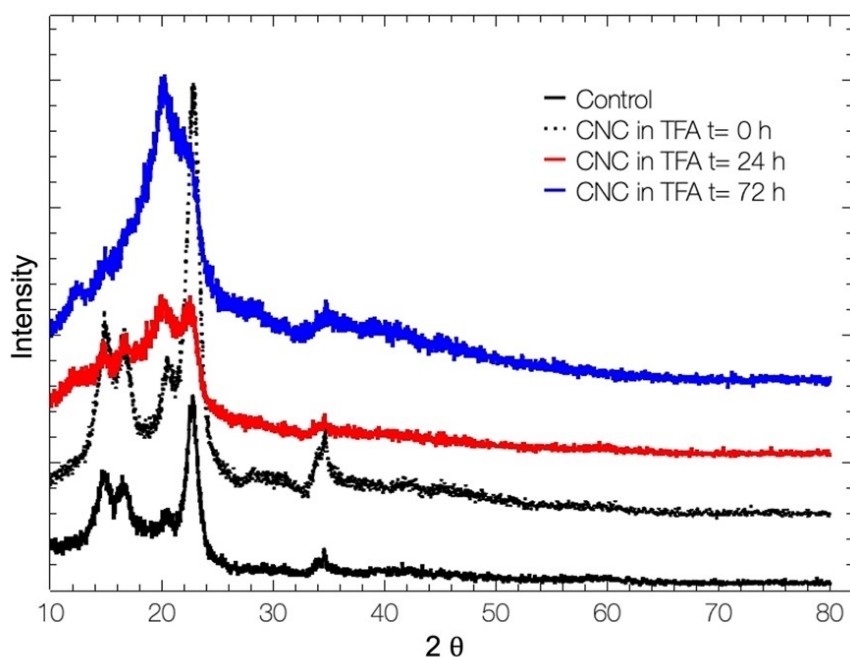

Figure 2.10: XRD patterns of the control group CNCs and those stirred in TFA for 0, 24 and 72 h.

2.4.3 SEM and BET Analysis of CNC-PET Composites

When CNC-PET composite films were prepared using the above-described method (Section 2.2.2), both the composite and the PET control that had been cast from TFA

showed porous structures (Figure 2.11 & 2.12). This made it difficult to measure contact angles since water droplets gradually absorbed into the dry films (Supplementary Data Table 4). However, measuring drop evolution over the same time periods allowed us to determine a significant increase in hydrophilicity of the films that contained CNCs compared to the control PET (Figures 2.13 & 2.14). It was also observed that the cellulose-PET composite films absorbed more water than the porous PET film (Tables 4 & 5).
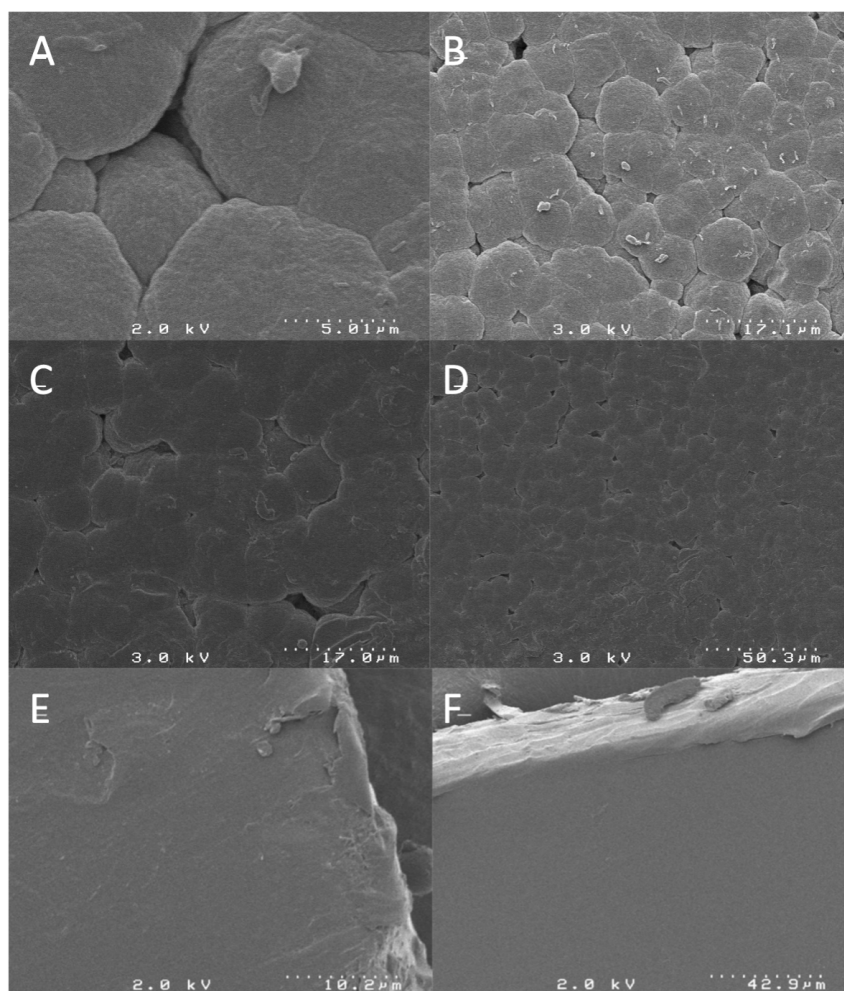
Figure 2.11: A and B: SEM images of a film produced from a 1:10 CNC:PET suspension in TFA aged 72 h. C and D: SEM images of a film produced from a solution of PET in TFA aged 72 h. E and F: SEM images of the surface of the PET used to produce the composite and solution films imaged above. Magnifications are indicated by the scale bars.

Porosimetry analysis (Figure 2.12) showed that the surface areas of the above cellulose-PET and the film produced from a solution of PET in TFA were the same, within experimental error, at 11.9 and 12.5 m^2/g, respectively. The pore size distribution is shown in Figure 2.12, which indicates that compositing PET with cellulose has no significant effect on overall porosity.
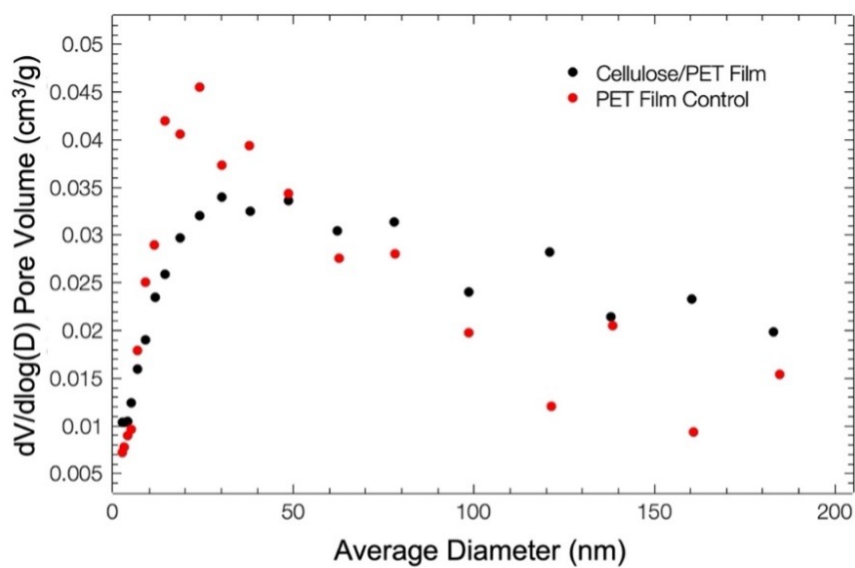
Figure 2.12: BET surface analysis of cellulose/PET film (red) and control PET film (black).

Films were pressed between tissue paper under a loading of 3 kg for 5 min to remove excess surface water and weighed (W_{wet}). Films were then dried in a fume hood at room temperature for 72 h to obtain the dry weight (W_{dry}). Water content was calculated based on the below formula:

$$\textbf{Water Content}\% = \frac{W_{wet} - W_{dry}}{W_{dry}} * 100\% \tag{1}$$

Table 4: Water content of porous cellulose/PET films and porous PET controls.

	CNC:PET	Water/Wet film % (Average)	Water/Wet film % (SD)
Cellulose/PET 24 h	1:10	64.8	1.6
PET control 24 h	–	54.0	3.7
Cellulose/PET 48 h	1:10	63.6	2.7
PET control 48 h	–	48.8	1.6
Cellulose/PET 72 h	1:10	64.1	2.4
PET control 72 h	–	47.5	1.6

Contact angles of dried films were measured using a VCA Optima instrument. Deionized water (3 mL) was added dropwise to the surface of the film. Images were captured with a high-resolution camera and contact angles were measured using AutoFAST imaging software. A timer set for 120 seconds was used during image capture. Data were recorded at intervals of 0 seconds, 60 seconds, and 120 seconds.
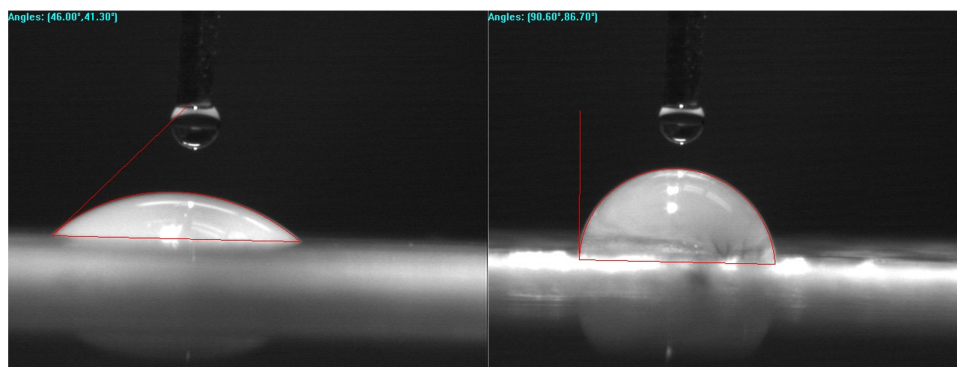

Figure 2.13: Contact angle measurements of 72 h CNC-PET film (left) and same for the control (right).

Table 5: Contact angle measurement data of CNC-PET films and control PET films over 4 min. Group 1, 3, 5: Cellulose/PET – 24 h, 48 h, and 72 h; group 2, 4, 6: PET – 24 h, 48 h, and 72 h.

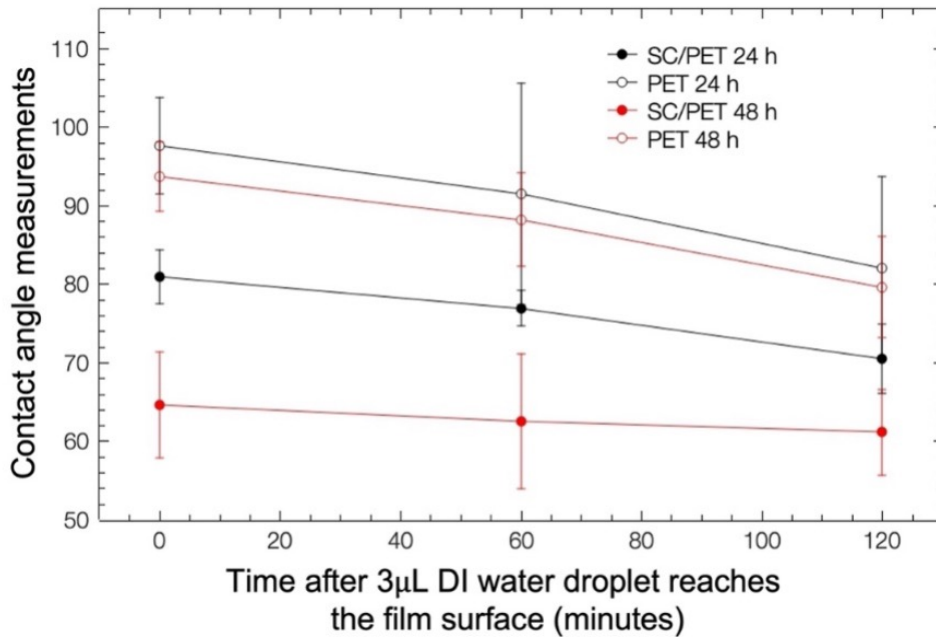| Seconds		1	2	3	4	5	6
0	Average	80.9	97.6	64.6	93.7	47.7	88.1
0	SD	3.4	6.1	6.8	4.4	4.0	1.8
60	Average	76.9	91.5	62.5	88.2	44.5	74.2
60	SD	2.3	14.1	8.6	5.9	2.6	1.4
120	Average	70.5	82	61.1	79.6	39.9	61.8
120	SD	4.4	11.7	5.5	6.4	5.1	5.9

Figure 2.14: Contact angle measurements of CNC-PET films and control PET films versus time.

2.5 Conclusions

The data presented here show that native CNCs can be physically dispersed in TFA and re-isolated essentially unchanged if precipitated out within a short period of time. Applications that require CNCs to be suspended in an organic medium can take

advantage of the outstanding dispersing properties and CNC suspension stabilizing potential of TFA, as well as its high volatility (bp 72 °C) and water miscibility, which enables easy removal from samples by evaporation or washing. Aging the CNC-TFA suspensions gradually adds trifluoroacetyl groups on the CNC surface with accompanying changes in rheology and transparency, which may be useful in applications where a more hydrophobic CNC is of interest. This study only addressed the nanocompositing of CNCs with PET, which was achieved by simple mixing of a CNC suspension with a solution of PET in TFA, then washing the resulting films. Nevertheless, the method should be useful for combining any organic-soluble polymer with unfunctionalized native cellulose.

2.6 Continued Work

A related project in the group involves the dissolution of cellulose (cotton, microcrystalline cellulose, or pine sawdust) in super-concentrated ($\geq$ 42% w/w) hydrochloric acid (which is prepared by bubbling HCl gas into 37% (w/w) HCl at a temperature of -40 °C).

Various sources of cellulose were dissolved in super-concentrated HCl solutions at temperatures ranging from -20 °C to room temperature over different time periods. In particular, cotton (pure cellulose) completely dissolved within 10 min (Figure 2.15) and was filtered through a sintered funnel. The filtrate was then quenched with DI water to precipitate the cellulose, which was collected as a white powdery solid after filtration and drying.
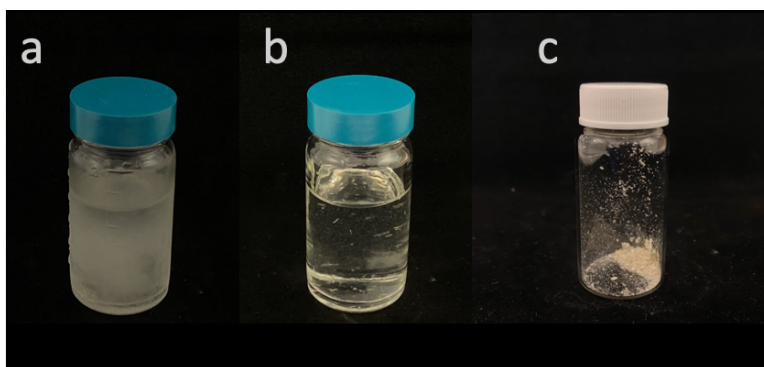
Figure 2.15: a) Cotton in concentrated HCl (42% w/w) at 0 min; b) Cotton in concentrated HCl (42% w/w) at 10 min; c) Cellulose recovered by reprecipitation of the solution in b) by the addition of water.

We plan to apply this technique to the composite powders described in Section 1.1.2 in order to remove the cellulose by dissolution in the super-concentrated HCl solution and recovering the PET by filtration. The remaining solid would be pure PET powder, which is normally obtained by grinding samples of PET cooled with liquid nitrogen. This study is currently underway.

2.7   Acknowledgements

References

Mahmoud, K. A., Mena, J. A., Male, K. B., Hrapovic, S., Kamen, A., & Luong, J. H. (2010). Effect of surface charge on the cellular uptake and cytotoxicity of fluorescent labeled cellulose nanocrystals. *ACS applied materials & interfaces*, *2*(10), 2924–2932.

Domingues, R. M., Gomes, M. E., & Reis, R. L. (2014). The potential of cellulose nanocrystals in tissue engineering strategies. *Biomacromolecules*, *15*(7), 2327–2346.

Dong, S., & Roman, M. (2007). Fluorescently labeled cellulose nanocrystals for bioimaging applications. *Journal of the American Chemical Society*, *129*(45), 13810–13811.

Akhlaghi, S. P., Tiong, D., Berry, R. M., & Tam, K. C. (2014). Comparative release studies of two cationic model drugs from different cellulose nanocrystal derivatives. *European Journal of Pharmaceutics and Biopharmaceutics*, *88*(1), 207–215.

Chen, W., Yu, H., Lee, S.-Y., Wei, T., Li, J., & Fan, Z. (2018). Nanocellulose: A promising nanomaterial for advanced electrochemical energy storage. *Chemical Society Reviews*, *47*(8), 2837–2872.

Chaka, K. T. (2022). Extraction of cellulose nanocrystals from agricultural by-products: A review. *Green Chemistry Letters and Reviews*, *15*(3), 582–597.

Reid, M. S., Villalobos, M., & Cranston, E. D. (2017). Benchmarking cellulose nanocrystals: From the laboratory to industrial production. *Langmuir*, *33*(7), 1583–1598.

Zhang, Y.-H. P., & Lynd, L. R. (2003). Cellodextrin preparation by mixed-acid hydrolysis and chromatographic separation. *Analytical biochemistry, 322*(2), 225–232.

Kontturi, E. (2018). Supramolecular aspects of native cellulose: Fringed-fibrillar model, leveling-off degree of polymerization and production of cellulose nanocrystals. *Cellulose science and technology: chemistry, analysis, and applications*, 263.

Kontturi, E., Meriluoto, A., Penttilä, P. A., Baccile, N., Malho, J.-M., Potthast, A., Rosenau, T., Ruokolainen, J., Serimaa, R., Laine, J., et al. (2016). Degradation and crystallization of cellulose in hydrogen chloride vapor for high-yield isolation of cellulose nanocrystals. *Angewandte Chemie International Edition, 55*(46), 14455–14458.

Pääkkönen, T., Spiliopoulos, P., Knuts, A., Nieminen, K., Johansson, L.-S., Enqvist, E., & Kontturi, E. (2018). From vapour to gas: Optimising cellulose degradation with gaseous hcl. *Reaction Chemistry & Engineering, 3*(3), 312–318.

Gomri, C., Cretin, M., & Semsarilar, M. (2022). Recent progress on chemical modification of cellulose nanocrystal (cnc) and its application in nanocomposite films and membranes-a comprehensive review. *Carbohydrate Polymers, 294*, 119790.

Tarasov, D., Leitch, M., & Fatehi, P. (2018). Lignin–carbohydrate complexes: Properties, applications, analyses, and methods of extraction: A review. *Biotechnology for biofuels, 11*(1), 1–28.

Siró, I., & Plackett, D. (2010). Microfibrillated cellulose and new nanocomposite materials: A review. *Cellulose, 17*, 459–494.

Saito, T., Kimura, S., Nishiyama, Y., & Isogai, A. (2007). Cellulose nanofibers prepared by tempo-mediated oxidation of native cellulose. *Biomacromolecules, 8*(8), 2485–2491.

Lin, N., Huang, J., Chang, P. R., Feng, J., & Yu, J. (2011). Surface acetylation of cellulose nanocrystal and its reinforcing function in poly (lactic acid). *Carbohydrate Polymers*, *83*(4), 1834–1842.

Viet, D., Beck-Candanedo, S., & Gray, D. G. (2007). Dispersion of cellulose nanocrystals in polar organic solvents. *Cellulose*, *14*, 109–113.

Kargarzadeh, H., Mariano, M., Huang, J., Lin, N., Ahmad, I., Dufresne, A., & Thomas, S. (2017). Recent developments on nanocellulose reinforced polymer nanocomposites: A review. *Polymer*, *132*, 368–393.

Huang, J., Chen, Y., & Chang, P. R. (2015). Surface modification of cellulose nanocrystals for nanocomposites. *Surface Modification of Biopolymers*, 258–290.

Lorenz, M., Sattler, S., Reza, M., Bismarck, A., & Kontturi, E. (2017). Cellulose nanocrystals by acid vapour: Towards more effortless isolation of cellulose nanocrystals. *Faraday Discussions*, *202*, 315–330.

Van den Berg, O., Capadona, J. R., & Weder, C. (2007). Preparation of homogeneous dispersions of tunicate cellulose whiskers in organic solvents. *Biomacromolecules*, *8*(4), 1353–1357.

Stainmesse, S., Orecchioni, A. .-., Nakache, E., Puisieux, F., & Fessi, H. (1995). Formation and stabilization of a biodegradable polymeric colloidal suspension of nanoparticles. *Colloid and Polymer Science*, *273*, 505–511.

Ramiah, M. (1970). Thermogravimetric and differential thermal analysis of cellulose, hemicellulose, and lignin. *Journal of applied polymer science*, *14*(5), 1323–1337.

Hasegawa, M., Isogai, A., Onabe, F., & Usuda, M. (1992). Dissolving states of cellulose and chitosan in trifluoroacetic acid. *Journal of applied polymer science*, *45*(10), 1857–1863.

Geddes, A. (1956). Interaction of trifluoroacetic acid with cellulose and related compounds. *Journal of Polymer Science*, *22*(100), 31–39.

Salin, B., Cemeris, M., & Malikova, O. (1993). Trifluoroacetic acid as a solvent for the synthesis of cellulose estersÐ3: Synthesis of mixed cellulose esters. *Khim Drev*, *5*, 3–7.

Zhao, H., Holladay, J. E., Kwak, J. H., & Zhang, Z. C. (2007). Inverse temperature-dependent pathway of cellulose decrystallization in trifluoroacetic acid. *The Journal of Physical Chemistry B*, *111*(19), 5295–5300.

Field, N. D., & Chien, M.-C. (1985). Poly (ethylene terephthalate)/cellulose blends. *Journal of applied polymer science*, *30*(5), 2105–2113.

Jia, N., Li, S.-M., Ma, M.-G., Zhu, J.-F., & Sun, R.-C. (2011). Synthesis and characterization of cellulose-silica composite fiber in ethanol/water mixed solvents. *BioResources*, *6*(2), 1186–1195.

Kassanov, B., Wang, J., Fu, Y., & Chang, J. (2017). Cellulose enzymatic saccharification and preparation of 5-hydroxymethylfurfural based on bamboo hydrolysis residue separation in ionic liquids. *RSC advances*, *7*(49), 30755–30762.

Cunha, A. G., Freire, C. S., Silvestre, A. J., Neto, C. P., Gandini, A., Orblin, E., & Fardim, P. (2007). Characterization and evaluation of the hydrolytic stability of trifluoroacetylated cellulose fibers. *Journal of colloid and Interface Science*, *316*(2), 360–366.

Segal, L., Creely, J. J., Martin Jr, A., & Conrad, C. (1959). An empirical method for estimating the degree of crystallinity of native cellulose using the x-ray diffractometer. *Textile research journal*, *29*(10), 786–794.

3 Butenolide Derivatives of Biobased Furans: Sustainable Synthetic Dyes

3.1 Introduction

3.1.1 Introduction to Dyes

Industrial dyes and pigments are almost exclusively derived from petrochemicals. The production for example of azo dyes, the largest class of organic colorants, relies on polyaromatic scaffolds from coal tar refining. Although many petroleum-based materials can be recycled, 100% of dyes end up in landfills, with all of their fossil carbon, ca. one million tons globally on an annual basis, ultimately emerging as carbon dioxide in the atmosphere (Carmen and Daniela, 2012). An answer to this issue from the sustainability movement has been to promote the use of plant-based dyes (Kasiri and Safapour, 2014). However, these products are expensive, suffer from generally inferior coloring performance, and many have poor substantivity, requiring metal mordants as fixatives, most of which ends up as effluent. Finally, natural dyes are low yield crops with high land, water, energy, and agrochemical burdens. Alternative microbiologically produced colorants embody creative alternatives to botanical dyes, (Newsome et al., 2014; Rose et al., 2018) although production limitations would suggest this is not a comprehensive solution to the problem.

Despite the large market for organic dyes, sustainable chemistry research has primarily targeted fuels and polymers, and virtually no reports of renewable synthetic colorants have appeared to date. The work described below thus represents an approach to introducing a new major chemical commodity to sustainable practice, i.e. biobased synthetic dyes.

3.1.2 CMF and its Derivatives

5-(Chloromethyl)furfural (CMF) **1** is a carbohydrate-derived renewable platform molecule that is considered to be a disruptive innovation in the field of green chemistry (Mascal, 2015, 2019). Equivalent to 5-(hydroxymethyl)furfural (HMF) **2** in its synthetic versatility, CMF **1** can be produced in high yield directly from raw biomass, while HMF **2** is only practically derived from fructose (van Putten et al., 2013).
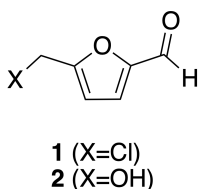

1 (X=Cl)
2 (X=OH)

Figure 3.1: Structure of CMF **1** and HMF **2**.

CMF **1** first appeared in the literature in 1901, when Henry Fenton (of Fenton's reagent fame) (Pignatello et al., 2006) described its production in low yields by treatment of sugars or cellulose with HCl (Fenton and Gostling, 1901). The Mascal group has significantly enhanced synthetic access to CMF and has been actively developing derivative markets with commercial potential, so we were intrigued by the description of an early investigation into the chemistry of halomethylfurfurals that borrowed from Fenton's work, in which treatment of 5-(bromomethyl)furfural (BMF) with barium carbonate in hot water resulted in the isolation of "a beautiful yellow... compound, which usually crystallizes in canary-yellow needles." (Cooper and Nuttall, 1911). The proposed formula was $C_{11}H_{10}O_4$, and yields were described as variable without being specified. No structural assignment was made, although it was suggested that the product could be the result of the reaction of BMF with levulinic acid, the latter of which is a known decomposition product of HMF **2**.

3.1.3   This Work

This chapter describes the study of CMF-based compounds containing strong chromophores that lead to bright colors in the yellow to red region of the visible spectrum. All synthesized dye compounds underwent characterization using UV-vis spectroscopy and were subsequently applied to standard fabrics, consisting of eight different fabric types, for dyeing tests. The wash fastness of all fabrics was assessed using the AATCC standard washing test. The comparison of color before and after washing was determined by color scanning under standard illumination conditions.

3.2   Experimental

3.2.1   Materials

All reagents and solvents were purchased from Millipore-Sigma. Multi-fiber test fabric consisting of cellulose acetate, cotton, polyamide type 66 (nylon), polyester, polyacrylic, silk, viscose, and worsted wool was purchased from Fisher Scientific. All dye compounds were prepared as previously described (Saska et al., 2019; Miao et al., 2023).

3.2.2   Spectroscopy

UV-visible spectra were measured on a Thermo Scientific Evolution 600 UV-vis spectrophotometer across a wavelength range of 200 – 600 nm. Fluorescence spectra were recorded on an Agilent Cary Eclipse fluorescence spectrophotometer.

3.2.3   Fabric Strip Dyeing

Formalin (250 mg) was added to deionized water (50 mL) and the mixture was stirred at 60 °C for 2 min. Phenol (150 mg), ammonium sulfate (100 mg), and the appropriate dye (50 mg) were added with stirring and the multi-fiber strip was introduced. The

dye bath was kept at 60 °C for another 15 min and then the pH was adjusted to 4-5 by the dropwise addition of acetic acid. The temperature of the bath was slowly increased (2 °C min^{-1}) until it reached 90 °C and kept at that temperature for 60 min. The temperature was then reduced to 60 °C and kept there for an additional 15 min. Finally, the bath was cooled to room temperature and the strip was removed, rinsed with deionized water three times, and allowed to dry overnight.

3.2.4   Wash Fastness Test

Colorfastness was measured using the AATCC Test Method 61 (Colorfastness to Laundering: Accelerated). Multi-fiber strips were dyed with all synthesized dye molecules. The detergent solution was prepared by dispersing AATCC reference detergent into deionized (DI) water at concentration = 0.37 wt%. After preheating 200 mL of the detergent solution to 40 °C in a 500 mL container, dyed fabric was introduced into the bath. The temperature inside the bath was maintained at 40 °C with vigorous stirring. The washed multi-fiber strip was then rinsed with DI water at 40 °C three times and dried in air overnight.
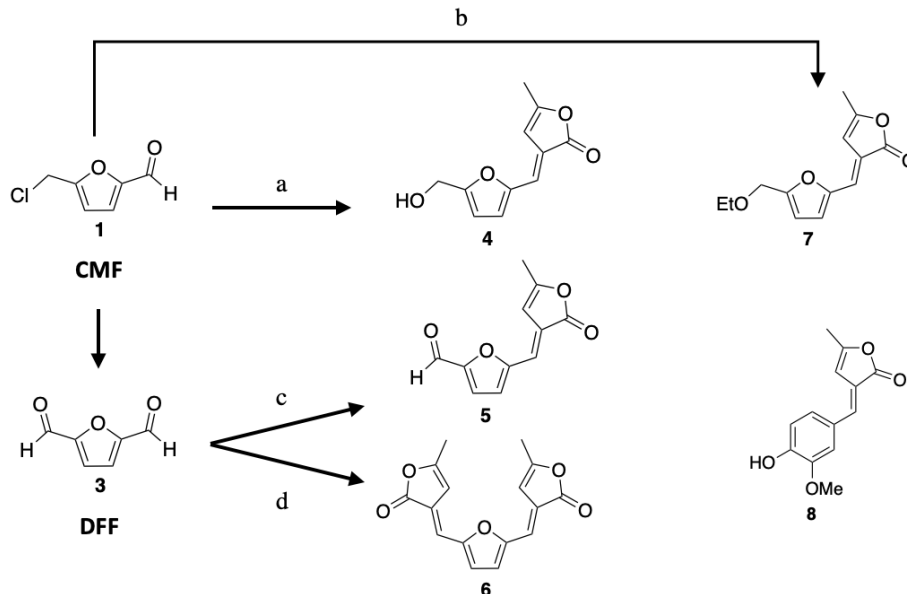
3.2.5   Color Scans

A Color-Eye® 7000A spectrophotometer (GretagMacbeth™, New Windersor, NY) was used to measure color changes before and after the wash fastness test.

## 3.3   Results and Discussions

3.3.1   Synthesis

The investigated dyes were synthesized in the Mascal group by Jan Saska, Haoqian Miao, Huitao Lin, Zheng Li, and others. The work involved either the direct deriva-

Scheme 2: Synthetic dyes from CMF and its derivatives. a, angelica lactone, 1,4-dioxane/water, Mn_2O_3, reflux 2 h, 87%; b, angelica lactone, ethanol, Mn_2O_3, reflux 2 h, 85%; c, angelica lactone, 80 °C, 1 h, 87%; d, angelica lactone, 1,4-dioxane, Mn_2O_3, reflux 2h, 82%. For CMF to DFF conversion, see Chapter 4.

tization of CMF **1** or the oxidation of CMF to DFF **3** using the Kornblum reaction as reported (Laugel et al., 2014) and subsequent derivatization. Thus, CMF **1** reacts with angelica lactone under aqueous conditions in the presence of Mn_2O_3 to yield **4** in 87% yield. Using ethanol as the solvent for the reaction gave the corresponding ethoxy derivative **7**, also in high yield (85%). Likewise, DFF **3** can be condensed with angelica lactone under mild conditions to yield a monoadduct **5**, or under more forcing conditions to give bis-adduct **6** as a deep red solid. Angelica lactone also reacts under the same conditions with other biobased aldehydes, for example vanillin, which gave bright yellow product **8** (Saska et al., 2019).

In recent work, the Mascal group electrochemically fixed carbon dioxide into the CMF derivative ethyl 5-(chloromethyl)furan-2-carboxylate **9** and then esterified the resulting acid to give ethyl 5-(carbethoxymethyl)furan-2-carboxylate **10**. Alternatively,
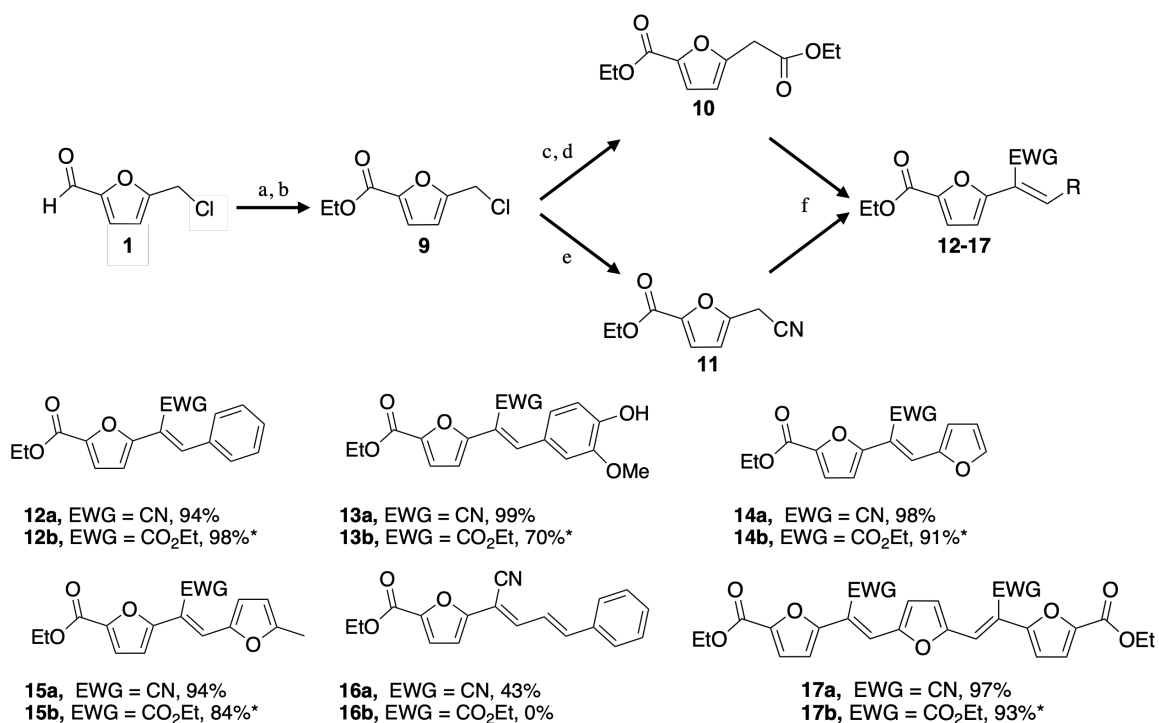
Scheme 3: Synthesis of ethyl 5-(chloromethyl)furan-2-carboxylate **9**, malonate ester **10**, and furylogous cyanoacetate ester **11**. Reagents and conditions: a. t-BuOCl, rt, 24 h; b. EtOH, 50 °C, 6 h, 82% over two steps; c. –2.7 V (vs. Fc/Fc$^+$), Ag/Al, 2 F mol^{-1}, 75%; d. EtOH, H$_2$SO$_4$, 40 °C, 12 h, 93%; e. NaCN, DMF, 0 °C, 0.25 h, 100%; f. RCHO, EtOH, piperidine 80 °C 12-72 h.

the chlorine in **9** could be displaced by cyanide to give the corresponding nitrile **11**. The Knoevenagel condensation was employed with **10** and **11**, resulting in arylidene derivatives with benzaldehyde and a range of biobased aldehydes to give derivatives **12**-**16**. A two-fold Knoevenagel reaction on DFF **3** yielded double Knoevenagel produts **17 a** and **b** in high yield (Miao et al., 2023). The strategy presented a versatile approach for obtaining strong chromophores from renewable sources, expanding the potential applications of sustainable dyes.

3.3.2   UV-vis and Fluorescence

While compound **5** had a similar absorption spectrum to that of **4**, its TLC spot showed evidence of fluorescence under UV light. Indeed, excitation of **5** at 389 nm gave a strong fluorescence peak at 497 nm (Figure 3.2). The extensive conjugation in **6** led to bathochromic shift compared to **5**, with molar absorptivities of 3.086 and $3.097 \times 10^4 \mathrm{M}^{-1}\mathrm{cm}^{-1}$ at 451 and 475 nm, respectively, values well within the range of commercial disperse dyes (Taniguchi & Lindsey, 2018).
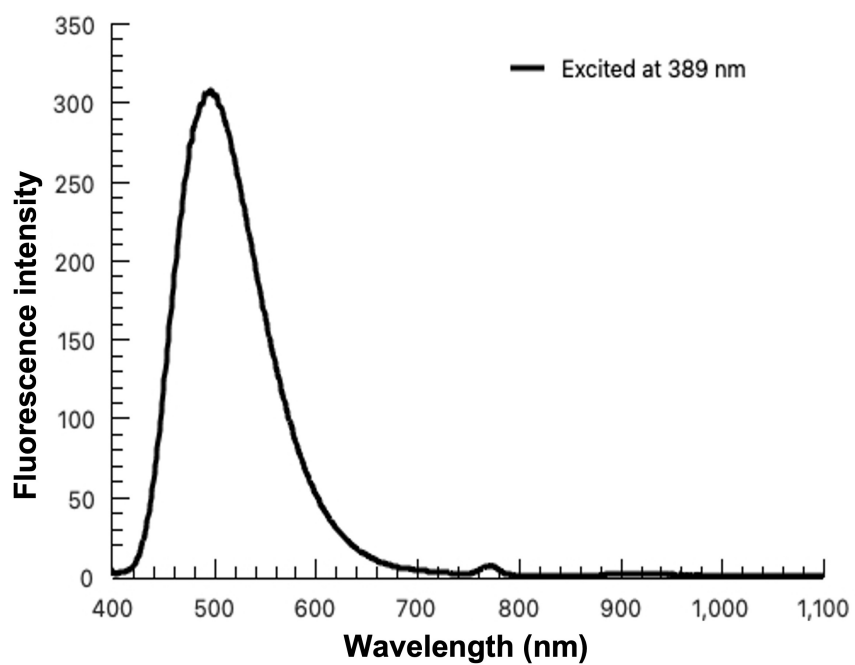
Figure 3.2: Fluorescence spectrum of compound **5** recorded upon excitation at 389 nm.
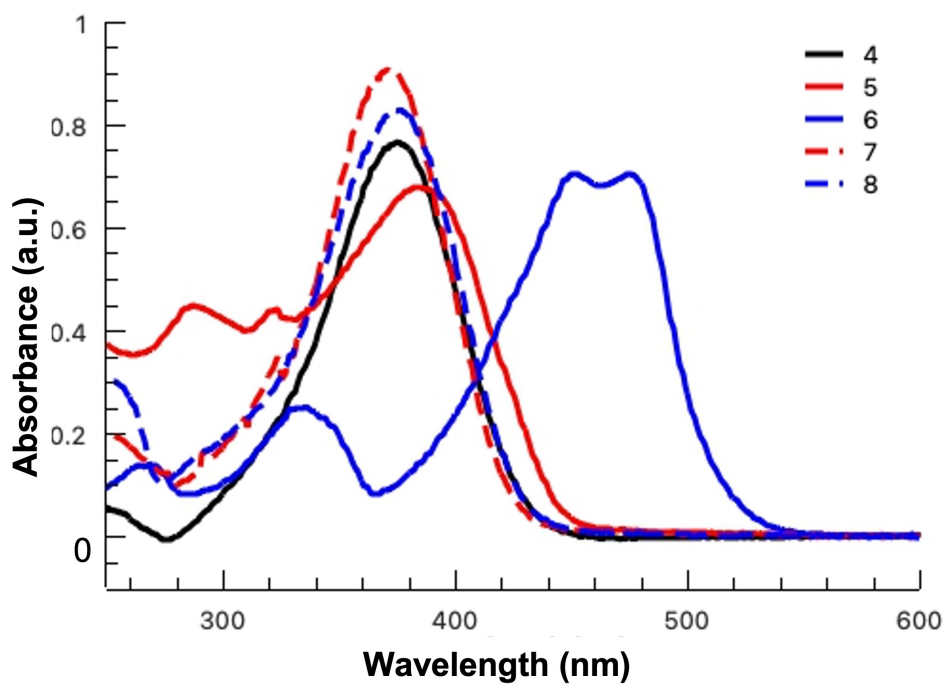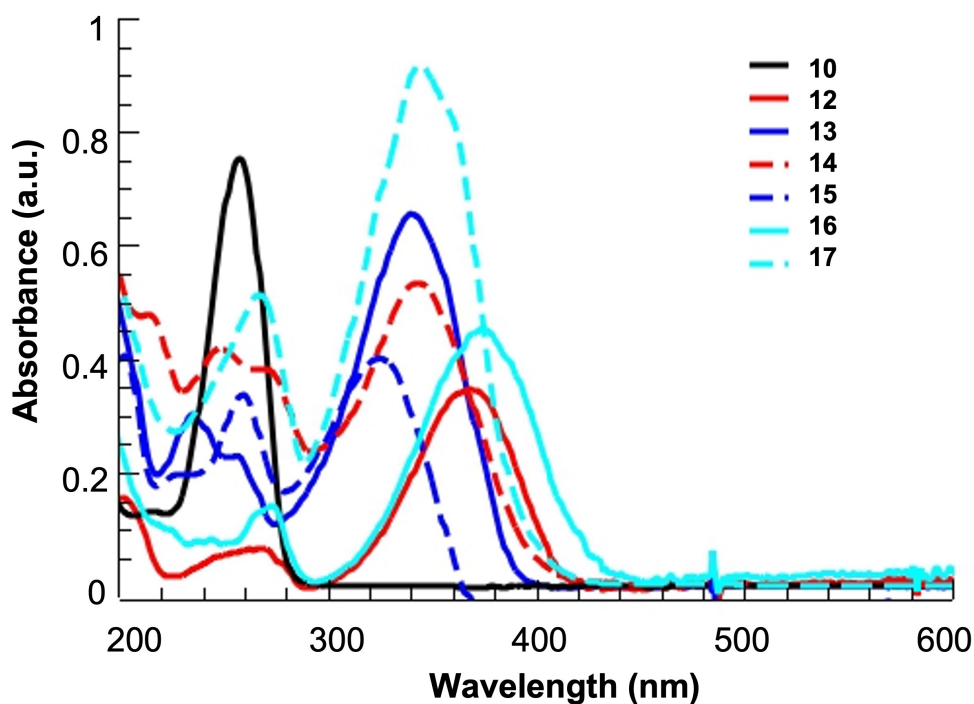

Figure 3.3: UV-vis spectra of compounds **4-8**.

Figure 3.4: UV-vis spectra of compounds **10**, **12b**, **13b**, **14a**, **15a**, **16a**, and **17a**.

The highly conjugated products from the reactions in Scheme 3 had bright colors ranging from yellow to red, where the maximum peak absorptions for **12-17** were observed to fall in the range of 340-452 nm. The chromophores in **17a** and **17b** produced by the two-fold condensation in particular showed a vibrant red/orange color.

The shift in the maximum absorption peak (λ_{max}) in a UV-vis spectrum is influenced by the extent of π bond conjugation in a molecule, with extended conjugation leading to a redshift (towards longer wavelengths) or reduced conjugation causing a blueshift (towards shorter wavelengths). This phenomenon is associated with changes in the electronic transitions within the molecule. In this study, when the electron-withdrawing group changed from ester to cyano, all compounds exhibited longer maximum wavelengths (λ_{max}). Positions of shifts in absorption can be seen in Table 6.

Table 6: UV Maximum Absorption Peaks for **4-8** and **12-17**.

Compound	Maximum Absorption Peak (nm)
4	374
5	385
6	451 & 475
7	372
8	378
12a	341
12b	325
13a	378
13b	344
14a	368
14b	344
15a	382
15b	354
16a	374
17a	451
17b	430

3.3.3 Applications

We carried out preliminary dyeing tests of **4-8**, **13b**, **15b**, and **17b** using a multifabric strip consisting of cellulose diacetate, cotton, nylon 6-6, Dacron 54 polyester, Dralon polyacrylic, silk, viscose, and wool. A standard aqueous dyeing procedure was used, involving the dyes (1 mg mL^{-1}), a dispersing agent (formalin), accelerator (phenol), and fixative (ammonium sulfate). The dyes colored all of the fabrics except cellulose and viscose (regenerated cellulose) with colors that varied from yellow (**4**, **7**, **8**, **13b**, **15b**, and **17b**) to canary (**5**) to orange (**6**).

Figure 3.5: Fabrics dyed by CMF derivatives, from left to right: **4**, **5**, **6**, **7**, and **8**

The evaluation of wash fastness is a critical aspect of assessing the stability and practicality of dyes on different fabrics. In this study, the standard test method AATCC 61 was employed to rigorously examine the wash fastness of the dyed fabrics, providing a reliable and reproducible metric. AATCC 61 is widely recognized as the industry standard for determining the colorfastness of textiles to domestic and commercial laundering procedures. By subjecting the fabrics to washing cycles, the standard method simulates real-world conditions and allows for a comprehensive evaluation of how well the synthetic dyes adhere to the textile substrates.

The synthetic dye compounds, in the form of finely ground powders, undergo particle dispersion in a liquid medium facilitated by dispersing agents, resulting in a homogeneous mixture of fine dye particles capable of penetrating fibers. The application to fibers, achieved through the method of immersion, involves the adhesion of these dispersed dye particles on to the fiber surface. Crucial for ensuring durable

wash fastness is the penetration of the dye into the fiber structure, a process facilitated by the application of gentle heat (60 °C), particularly in the cases of nylon, wool, and Dacron 54 polyester. The synthesized dyes in this study demonstrated a high affinity for most of the tested fibers, forming chemical bonds that contribute to their wash fastness. The permanence of dye color is attributed to the resistance of these bonds to cleavage during washing.

To quantitatively evaluate the colors before and after washing, we utilized a Color-Eye® 7000A spectrophotometer, an instrument for precise color measurement. The results from the measurements are presented in the CIELAB system, a simplified mathematical approximation to a uniform color space composed of perceived color differences (Hill et al., 1997). The perceived lightness L* by a standard observer is assumed to follow the intensity of a color stimulus according to a cubic root law CIE1986a (a color space system). The lightness L*, green-red coordinates a*, and blue-yellow coordinates b* are used to define a color (Figure 3.6).
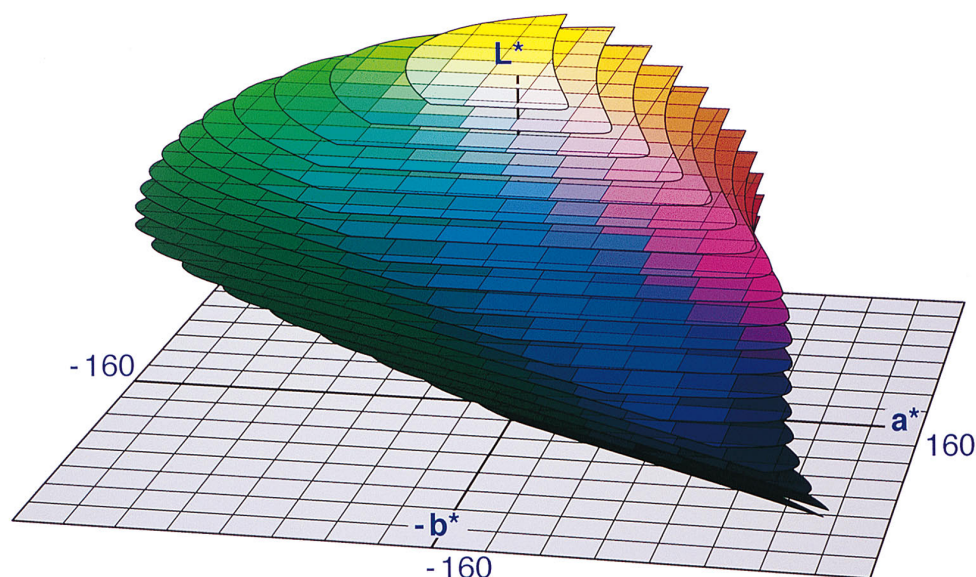

Figure 3.6: CIELAB optimal color space composed of planes of constant lightness L*, green-red coordinates a*, and blue-yellow and coordinates b* (Hill et al., 1997).

Any color represented in the rectangular coordinate system of axes L*, a*, b* can alternatively be expressed in terms of polar coordinates with the perceived lightness L* and the chroma,

$$\Delta C_{ab}* = \sqrt{a^{*2} + b^{*2}} \tag{2}$$

and hue angle,

$$h_{ab} = tan^{-1}(\frac{b*}{a*}) \tag{3}$$

The total difference between the two colors is given in terms of L*, a*, b* by the formula

$$\Delta E_{ab} = \sqrt{\Delta L^{*2} + \Delta a^{*2} + \Delta b^{*2}} \tag{4}$$

Here, we used one group of comparisons as an example; more results are listed in appendix (A). Groups labeled with D denote dyed fabric, while those labeled with W denote washed fabric. From Table 7, all groups exhibit very close results in ΔEab, indicating very little color difference between the dyed or washed samples. All fabrics were compared under standard illuminant D65, which is a standardized light source used in color science and imaging. It represents a spectrum of light that simulates average daylight with a correlated color temperature of approximately 6500 Kelvin. D65 is commonly used as the reference illuminant for many colorimetric measurements, such as those made in photography, printing, and display technologies. It provides a standardized basis for comparing colors and ensuring consistency across different viewing conditions and environments.

For a better illustration of the color difference, the color scanned by the spectropho-

Table 7: Nylon dyed and washed with compounds **4**, **5**, and **6**. The fabrics were scanned and the results are presented in the CIELAB color space.

Fabric	Compound	ΔL^*	Δa^*	Δb^*	ΔC^*	ΔH^*	ΔEab
Nylon	D4	-11.08	2.18	42.32	41.32	-9.38	62.42
Nylon	W4	-12.92	3.03	42.78	41.83	-9.49	63.22
Nylon	D5	-25.77	24.84	61.53	65.14	-12.62	97.98
Nylon	W5	-23.76	22.71	59.24	62.24	-12.30	93.66
Nylon	D6	-23.34	34.64	64.99	72.40	-13.51	108.59
Nylon	W6	-23.70	31.72	64.07	70.25	-13.25	105.44

tometer was used to obtain the accurate position in the L*, a*, and b* coordinates in the color space. This representation allows for the identification and visualization of the specific color associated with the given coordinates, as illustrated in Figure 3.7. The reflection spectra (Figure 3.8) also showed that the two spectra, before and after washing, were well overlaid.
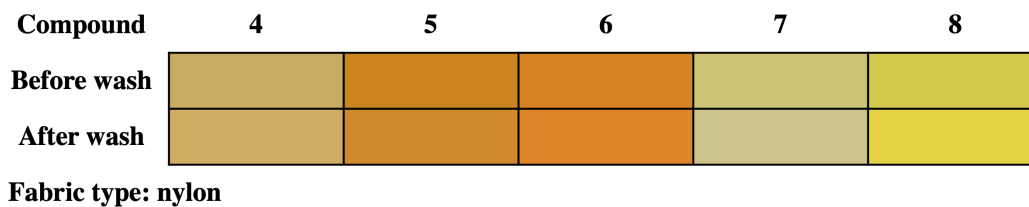
Figure 3.7: A comparison of color reflectance on nylon dyed using compounds **4-8**. The presented colors were scanned under standard illuminant D65 from the dry fabrics before and after washing.
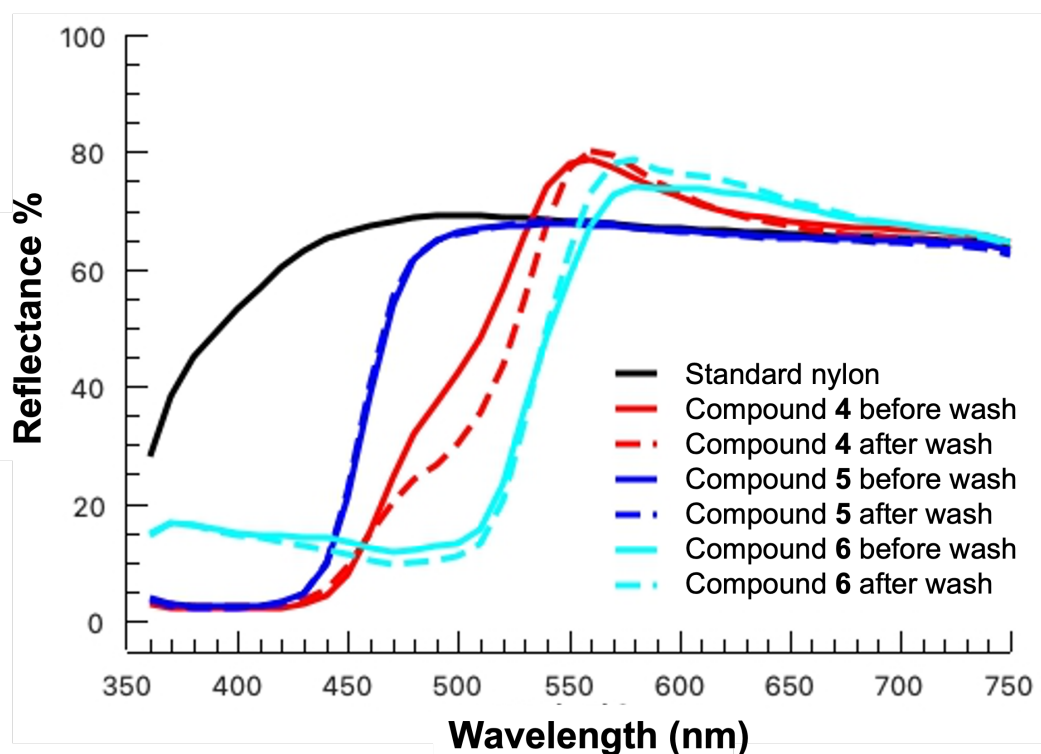
Figure 3.8: Reflectance spectra of nylon dyed using compounds **4**, **5**, and **6**. Color scanned under standard illuminant D65 from the dry fabrics before and after washing.

3.4 Conclusions

In summary, although various classes of sustainably sourced industrial products have been described in the literature, to our knowledge, no synthetic dyes produced entirely from biomass-derived platform molecules had been reported. It was our intention to introduce the concept of biobased synthetic dyes that bore neither the stigma of derivation from petrochemicals nor the drawbacks of natural colorants. The method described here is versatile and could, in principle, be applied to any naturally occurring aromatic aldehyde. The potential of CMF to deliver renewable solutions for commercial markets was showcased in terms of industrially relevant synthetic colorants, in this case, exploiting Knoevenel-type reactivity between a furylogous malonate or a furylogous

cyanoacetate and biomass-derived aldehydes, with no strong bases or harsh conditions involved. The products had bright colors ranging from yellow to the red region of the spectrum and were shown to demonstrate good color performance and colorfastness on selected fabrics. The prospect of producing 100% renewable textiles, where both the synthetic fibers and dyes are biobased, is thus within reach. Preliminary analysis showed good color performance and substantivity and, combined with more sustainably produced synthetic fabrics, the potential to unlock new markets in 100% sustainable wearables is in view.

3.5   Acknowledgements

References

Kasiri, M. B., & Safapour, S. (2014). Natural dyes and antimicrobials for green treatment of textiles. *Environmental chemistry letters*, *12*(1), 1–13.

Newsome, A. G., Culver, C. A., & Van Breemen, R. B. (2014). Nature's palette: The search for natural blue colorants. *Journal of Agricultural and Food Chemistry*, *62*(28), 6498–6511.

Rose, P. M., Cantrill, V., Benohoud, M., Tidder, A., Rayner, C. M., & Blackburn, R. S. (2018). Application of anthocyanins from blackcurrant (ribes nigrum l.) fruit waste as renewable hair dyes. *Journal of Agricultural and Food Chemistry*, *66*(26), 6790–6798.

Mascal, M. (2015). 5-(chloromethyl)furfural is the new hmf: Functionally equivalent but more practical in terms of its production from biomass. *ChemSusChem*, *8*(20), 3391–3395.

Mascal, M. (2019). 5-(chloromethyl)furfural (cmf): A platform for transforming cellulose into commercial products. *ACS Sustainable Chemistry & Engineering*, *7*(6), 5588–5601.

van Putten, R.-J., Van Der Waal, J. C., De Jong, E., Rasrendra, C. B., Heeres, H. J., & de Vries, J. G. (2013). Hydroxymethylfurfural, a versatile platform chemical made from renewable resources. *Chemical reviews*, *113*(3), 1499–1597.

Pignatello, J. J., Oliveros, E., & MacKay, A. (2006). Advanced oxidation processes for organic contaminant destruction based on the fenton reaction and related chemistry. *Critical reviews in environmental science and technology*, *36*(1), 1–84.

Fenton, H. J. H., & Gostling, M. (1901). Lxxxv.—derivatives of methylfurfural. *Journal of the Chemical Society, Transactions*, *79*, 807–816.

Cooper, W. F., & Nuttall, W. H. (1911). Some reactions of omega bromomethylfurfuraldehyde. *Journal of the Chemical Society, Transactions*, *99*, 1193–1200.

Saska, J., Li, Z., Otsuki, A. L., Wei, J., Fettinger, J. C., & Mascal, M. (2019). Butenolide derivatives of biobased furans: Sustainable synthetic dyes. *Angewandte Chemie International Edition*, *58*(48), 17293–17296.

Miao, H., Ling, H., Wei, J., & Mascal, M. (2023). Furylogous nucleophile chemistry for the preparation of renewable dyes. *ACS Sustainable Chemistry & Engineering*, *11*(4), 1502–1507.

Laugel, C., Estrine, B., Le Bras, J., Hoffmann, N., Marinkovic, S., & Muzart, J. (2014). Sodium Bromide DMSO-Induced Synthesis of 2,5-Diformylfuran from Fructose or 5-(Hydroxymethyl) furfural. *ChemCatChem*, *6*(5), 1195–1198.

Taniguchi, M., & Lindsey, J. S. (2018). Database of absorption and fluorescence spectra of> 300 common compounds for use in photochem cad. *Photochemistry and photobiology*, *94*(2), 290–327.

Hill, B., Roger, T., & Vorhagen, F. W. (1997). Comparative analysis of the quantization of color spaces on the basis of the cielab color-difference formula. *ACM Transactions on Graphics (TOG)*, *16*(2), 109–154.

4   Optimization of the Synthesis of 2,5-Diformylfuran from 5-(Chloromethyl)furfural

4.1   Introduction

4.1.1   Biomass Derivatives

5-(Chloromethyl)furfural (CMF) is derived from renewable sources like agricultural waste. The significance of CMF lies in its utility as a biobased platform molecule, and its derivatives are the subject of keen interest for renewable chemistry researchers (Mascal, 2015, 2019). Similarly, 2,5-diformylfuran, or DFF, is also a compound derived from biomass that offers potential applications across multiple fields. Specifically, its two formyl groups are synthetically versatile, making it a useful precursor for a range of products. For example, the polymerization of DFF yields tunable materials, including resins (Amarasekara et al., 2009) and polyimines (Xiang et al., 2013). We therefore sought to add value to DFF as a biobased platform by exploring its synthesis, reactivity, and applications.

4.1.2   Current Synthesis of 2,5-Diformylfuran

A number of methods are available for synthesizing DFF from 5-(hydroxymethyl)furfual (HMF) via selective oxidation of the OH group, both involving homogeneous and heterogeneous metal catalysis and metal-free oxidation. These are summarized in a graphic presentation of the relevant literature in Figure 4.1.

Although most of preparations of DFF in the literature start from HMF, it is generally considered that the production of HMF directly from biomass is problematic, and the typical synthesis using fructose is expensive and controversial due to the use of food to make chemicals (Fischer et al., 2009). Laugel et al. therefore developed
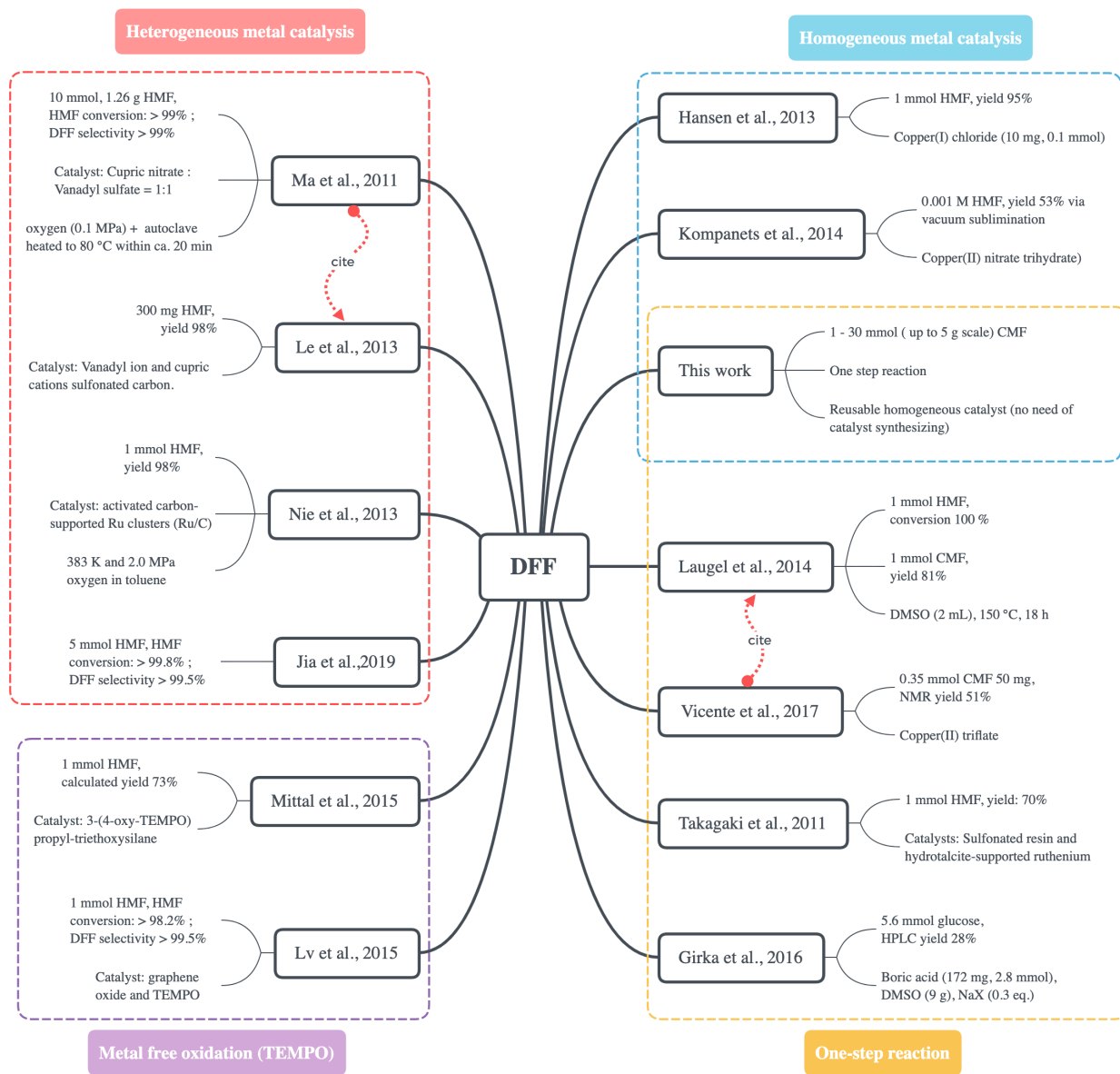
Figure 4.1: Graphical literature map describing DFF synthesis.

an effective synthesis of DFF via Kornblum reaction of CMF with DMSO. High temperatures (150 °C) and extended reaction times (18 hours) are however necessary for this method (Laugel et al., 2014), and we found that attempts to scale the reaction beyond 0.5 mmol led to low yields. Since a major part of the work in this thesis involves the use of DFF (Chapter 3), we undertook a project to synthesize DFF from CMF on a multigram scale without the use of Kornblum chemistry.

4.1.3 This Work

This chapter focuses on the synthesis of DFF directly from CMF by oxidation using bismuth(III) nitrate pentahydrate. This method was originally devised in the Mascal group by postdoc Dr. Saikat Dutta. It is further developed in this thesis, where the reaction parameters are systematically explored, ranging from small-scale experiments up to a 2 g scale, assessing its prospective application ultimately for industrial-scale production. The concept is rendered in Scheme 4, where CMF is oxidized by nitrate ion, which is reduced to lower oxides of nitrogen. The resulting bismuth oxide by product can be converted back into bismuth nitrate, making bismuth the carrier and nitric acid the formal oxidant. Direct reaction of CMF with nitric acid has been described, however this leads to over-oxidation to give 2,5-furandicarboxylic acid in moderate yield (Brasholz et al., 2011).

4.2 Methodology

4.2.1 Materials

Bismuth(III) nitrate pentahydrate, 70% nitric acid, dichloromethane (DCM), 1,2-dichloroethane (DCE), methanol, ethanol, diethyl ether, hexane, ethyl acetate, and toluene were all purchased from Sigma Aldrich.
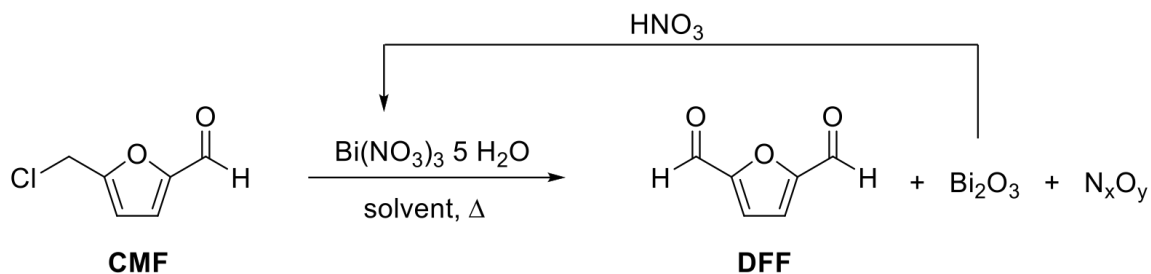
Scheme 4: Preparation of DFF from CMF with bismuth(III) nitrate pentahydrate and recycle of bismuth(III) oxide product back to bismuth(III) nitrate.

4.2.2 Synthetic Method

CMF was introduced into a round-bottom flask together with the stated solvent (if any) and the mixture was stirred vigorously. Bismuth(III) nitrate pentahydrate was introduced portion-wise. The rate of addition was adjusted to minimize gas evolution. Following the stated heating period, the reaction mixtures were allowed to cool to room temperature.

4.2.3 Purification

Simple extraction: The pale yellow solid reaction mixtures were pulverized using a glass rod. The resulting powders were then stirred in the stated solvents (as detailed in the extraction study in Section 4.3.2) under the given conditions. After this, the mixtures were filtered. The filtrates were collected and the solvent was evaporated under reduced pressure. The resulting solid products were left to dry overnight under vacuum.

Continuous extraction: The reaction mixtures were transferred into a Soxhlet apparatus. The solid was extracted by circulating solvent for the stated period. The extracts were dried using magnesium sulfate and the solvent was evaporated under reduced pressure. The resulting solid products were dried overnight under vacuum.

Chromatography: Crude mixtures obtained from reactions were subjected to chromatographic separation using a Biotage flash chromatography system using a silica gel stationary phase. Methanol (MeOH) and dichloromethane (DCM) in a ratio of 1:99 was the mobile phase. The chromatographic process was monitored using UV detection at wavelengths of 254 nm and 280 nm. Fractions containing the desired products were collected and the solvent was subsequently evaporated under reduced pressure to give solid products. These products were dried overnight under vacuum.

Sublimation: The reaction mixtures were transferred into a sublimation apparatus and heated at 85 °C under high vacuum overnight. The sublimed product was collected by carefully scratching it off the cold finger. The collected product was then dried overnight under vacuum.

4.2.4   Characterization

The crude reaction products were analyzed by ^{1}H and ^{13}C NMR in deuterated chloroform at 400 and 100 MHz, respectively. For GCMS analysis, a 1 mg sample was dissolved in 10 mL of solvent and the mixture was filtered through a 0.4-micrometer PTFE filter. The resulting solution was then introduced into an AGILENT 6890N/5973 gas chromatography-mass spectrometry (GC-MS) instrument. Melting points were determined using an MPA120 automated melting point system.

4.3   Results and Discussion

4.3.1   Preliminary Results

The method as originally devised by Dr. Saikat Dutta consisted of the oxidation of 1.0 g of CMF with 2.7 g (0.8 eq.) bismuth(III) nitrate pentahydrate at 80 °C with vigorous stirring in the absence of solvent. The crude reaction mixture was washed with DCM

and the solvent was evaporated to give DFF (0.66 g, 5.3 mmol, 72%), which appeared to be clean by NMR. This work was followed up by Dr. Boqiong Lu, who obtained similar results by mixing of CMF with bismuth(III) nitrate pentahydrate at room temperature. On standing, she noted a red-brown gas being evolved from the mixture, even in the absence of heating. The preliminary yield of DFF (by mass) was about 80%. Later, questions were raised about the actual purity of these samples, and it was clear that the method would benefit from further development and more careful analysis.
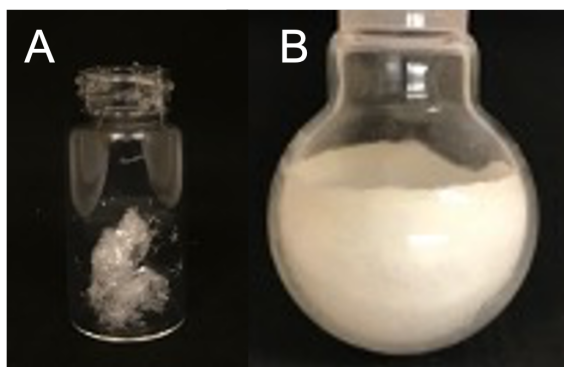
Figure 4.2: Photos of DFF samples isolated by, a. sublimation, b. extraction followed by rotary evaporation.

4.3.2 Empirical Studies

CMF was subjected to the above oxidation protocol under a wide range of reaction conditions involving the following variables: the raio of CMF to bismuth(III) nitrate pentahydrate, temperature, solvent, and reaction time. Given the exothermic nature of this reaction, it was recognized that scaling would involve additional challenges.

4.3.2.1 Small-Scale Oxidation of DFF: Exploring Reactions on Less than 1 Gram Scale

a. Solvent Effect

The synthesis of DFF from CMF at a scale below 1 gram involved the introduction

of CMF into a flask heated at the stated reaction temperature with the stated reaction solvent and the portionwise addition of bismuth(III) nitrate pentahydrate. The evolution of red-brown nitrogen dioxide gas could be observed throughout the addition, controlling the rate of which allowed for moderating the reaction process. Additional solvent was introduced to further moderate the reaction, while continuing to monitor the production of nitrogen dioxide. Under the optimal conditions, the bismuth(III) nitrate pentahydrate (0.73 equiv., 0.40 g) was carefully added to 1 mmol of CMF (0.16 g) (Table 8), the CMF at 60 °C over the course of 5 minutes. When nitrogen dioxide evolution became too vigorous, the rate of addition was slowed. During the reaction, the mixture transitions from a viscous brown-black to pale yellow, later becoming very viscous. As the viscosity increases, stirring with a glass rod becomes necessary. Following a preliminary solvent screening, a comparative evaluation of the better solvents (DCE, DCM, and chloroform, Table 8, Trials 1-3) was undertaken. It was shown that DCE (boiling point 84 °C) was the optimal solvent, returning up to a 95% mass yield of crude product.

   b. Reaction Time

   At sub-gram scales, an optimized mass yield of 95% of crude product could be achieved as described above using 5 mL of DCE with stirring at 60 °C for 2 hours (Table 8 Trial 1). It is worth noting that shorter reaction times or inadequate temperature control resulted in incomplete CMF conversion, particularly when the mixture reached high viscosity. As the scale was increased (Trial 5) under similar conditions, the reaction yield was observed to decrease with increasing reaction time. After 1 hour, the mass yield was 75%, but it dropped to 48% after 5 hours (Table 8, Trials 5-7). This was accompanied by an observable darkening of the mixture which was likely due to the increased exothermicity of the reaction.

   Several strategies were employed to address the exothermicity issue at larger scales.

Table 8: Synthesis of DFF from CMF at scales less than 1 gram

	CMF (g)	Eq. Ratioa	Solvent in total (mL)	Temperature (°C)	Time (h)	Mass Yield %
1	0.16	0.73	DCE 5 mL	60	1	95
2	0.15	0.80	DCM 5 mL	60	1	69
3	0.17	0.73	Chloroform 5 mL	60	1	89
4	0.47	0.75	DCE 5 mL	70-80	2	92
5	0.72	0.73	DCE 20 mL	60-80	1	75
6	0.82	0.73	DCE 20 mL	60-80	3	64
7	0.83	0.73	DCE 20 mL	60-80	5	48
8*	0.70	0.74	DCE 20 mL	60-80	1.5	60
* Addition of 1 mL 70% concentrated nitric acid.						
a. Molar ratio of bismuth(III) nitrate pentahydrate to CMF.						

These included pre-mixing CMF with the solvent prior to introduction into the reaction flask. During the heating, bismuth(III) nitrate pentahydrate was also added over an extended period of time (from 0.2 g per minute to 0.07 g per minute). The optimal time range for addition is shown in Figure 4.3.
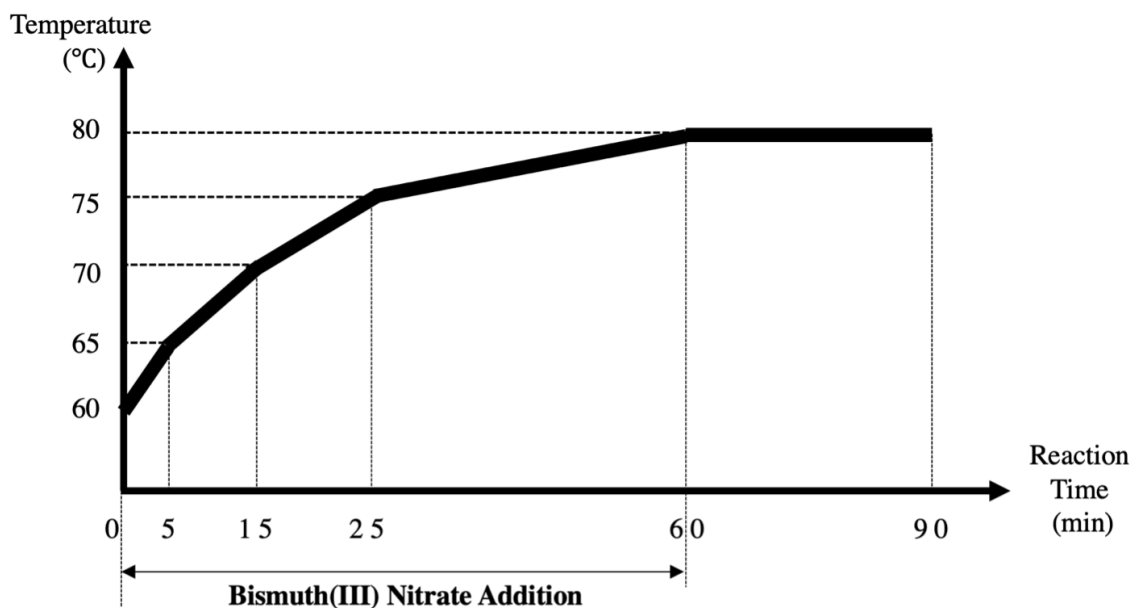
Figure 4.3: The optimal temperature curve for the addition of bismuth(III) nitrate pentahydrate to CMF, with five additions of 20% of the total each time.

4.3.2.2 DFF Oxidation at the 1 Gram Scale: Optimization and Yield Evaluation

a. Air Purging

In the transition to from a sub-gram scale to a 1 gram CMF scale (Table 9), the addition of bismuth(III) nitrate pentahydrate posed additional challenges. Under the optimal conditions, introducing 1.89 equiv. (8.0 g) of bismuth(III) nitrate pentahydrate with stirring at 70-80 °C over 1.5 hours resulted in a mass yield of 82% (Trials 1 & 2). To achieve this, the reaction was continually purged with air to dissipate excess heat (Trials 3 & 4). However, the reaction was not very reproducible due to its exothermicity.

b. Addition of Nitric Acid

On a sub-gram scale (Table 8, Trial 8), the addition of concentrated nitric acid to the reaction mixture resulted in a reasonably good mass yield (approximately 60%). However, when 1 mL of concentrated nitric acid was added on the 1 gram scale with stated amount of bismuth(III) nitrate pentahydrate (Table 9 Trials 6 & 7), the yield dropped to 44% after an hour of stirring, further dropping to 32% overnight. This reduction in yield may be the result of the presence of water and possibly overheating. High viscosity during the later stages of the reaction further impeded oxidation.

c. Premixing with Celite

In other attempts to prevent overheating, instead of adding solvent, celite (2 g) was mixed with the CMF (1.07 g). Bismuth(III) nitrate pentahydrate (0.75 equiv., 2.72 g) was then added and the reaction was allowed to proceed for 20 minutes without heating. While this approach did not yield significantly better results (32% mass yield), it appeared to provide a more moderate reaction environment that did not necessitate vigilant monitoring (Table 9 Trials 8 & 9). Finally, the use of diglyme solvent was also tested (boiling point 162 °C), which kept the reaction in a liquid state during the exothermic phase. However, this strategy also did not lead to an improved

Table 9: Synthesis of DFF from CMF at a ca. 1 g scale

	CMF (g)	CMF (mmol)	Eq. Ratio[a]	Solvent in Total (mL)	Temperature (°C)	Time (h)	Mass Yield %
1	1.2625	8.73	1.89	DCE 5 mL	70-80	1.5	82
2	1.1258	8.83	1.87	DCE 5 mL	60-80	1.5	83
3	1.3187	9.12	1.79	DCE 5 mL	70-80	1.5[b]	93
4	1.1682	8.08	1.79	DCE 5 mL	60-80	1.5[b]	92
5	1.0637	7.39	1.79	DCE 5 mL	60-80	1.5[b]	51
6*	1.3885	9.59	0.88	DCE 5 mL	60-80	1	44
7*	1.3864	9.61	0.69	DCE 5 mL	60-80	overnight	33
8	1.0680	7.39	1.20	Celite 2 g	60-80	1	28
9	1.0763	7.45	0.75	Celite 2 g	60-80	0.5	32
10	0.9614	6.65	1.97	Diglyme 5 mL	60-80	6[c]	44
11	1.0023	6.93	1.79	Celite 2 g	60-80	1.5	trace[d]
* Addition of 1 mL 70% concentrated nitric acid; a. Molar ratio of bismuth(III) nitrate pentahydrate to CMF; b. air purge; c. an open beaker; d. sublimination							

yield (Trial 10).

4.3.2.3. DFF Oxidation at the 2 Gram Scale: Scaling Up and Performance Assessment

It was observed that some DFF was embedded within the solid residue after filtration of the 1 g scale reactions, suggesting the need for improved isolation. A series of 2 g scale reactions (approximately 40 trials) were conducted, from which 10 are selected here for detailed discussion (Table 10).

a. Sensitivity of the Reaction

Trial 1 (Table 10) simply involved the doubling of all quantities of the 1 g scale reaction while maintaining the best conditions from Table 9. Introducing acetonitrile (ACN) during the extraction process appeared to have a beneficial effect. A DCM-ACN solvent mixture was thus found to be optimal for the extraction. It was however observed that, at this scale, the reaction mixture solidified rapidly after the exotherm

Table 10: Synthesis of DFF with CMF at a ca. 2 g scale

	CMF (g)	CMF (mmol)	Eq. Ratio^a	DCE (mL)	Temp (°C)	Time (h)	Extraction	Mass Yield %
1	1.9100	13.21	1.64	20	80	2^b	DCM & ACN	83
2*	1.9327	13.37	1.65	20	80	2^b	DCM & ACN	82
3*	3.0550	21.13	1.66	60	80	2^b	DCM & ACN	55
4*	3.0445	21.06	1.66	60	80	2^b	DCM & ACN	78
5*	2.0900	14.16	1.80	60	80	2^b	DCM & ACN	20
6*	2.1672	14.99	1.80	60	80	2^b	DCM & ACN	83
7*	1.8686	12.93	1.59	20	80	2^c	Toluene 24 h^e	59
8*	3.3592	23.24	1.62	20	80	2^c	DCM 6 h^e	36
9*	3.1857	22.04	1.66	20	80	2^c	DCM 36 h^e	62
10	5.3900	37.29	1.60	50	80	12^d	DCM & ACN	53

* Addition of 2 mL 70% concentrated nitric acid;
a. Molar ratio of bismuth(III) nitrate pentahydrate to CMF;
b. air purge;
c. in an open beaker;
d. sonication; e. continuous extraction

subsided, reducing the efficacy of heat removal by air purging The exothermic process persisted over 1 h, and continuous air purging was maintained until the conclusion of the exothermic process. Trial 2 included 2 mL of concentrated nitric acid in an attempt to keep the reaction from solidifying. Using the same purification method, both trials (Trials 1 & 2) gave similar mass yields of 83% and 82% respectively. However, on attempting to repeat the reaction under the optimized conditions (Trials 3-6), different yields were obtained. This clearly shows that the reaction has reproducibility issues. It was observed that when gas evolution became erratic, CMF decomposition was observable, with a color change from pale yellow to black within seconds, and heating at the 2 gram scale was more difficult to control due to the greater exotherm.

b. Extraction Study

Due to the difficulty of removing the DFF product and any unreacted CMF from the residue after filtration, isolating these components at the 1 g scale was challenging. This

problem was magnified in reactions at 2 g scale and beyond. Continuous extractions were carried out in an attempt to resolve this issue. However, this led to impurities being co-extracted with the DFF on extended extraction. Screening showed that the best solvent for this process was DCM (Table 10, Trials 7-9). Sonication was also applied during the extraction in trial 12 but did not improve yield.

Summary of the Empirical Study

Throughout the experiments spanning from sub-gram scale to a 2 gram scale, we employed various strategies to address issues related to exothermicity and product isolation. Despite our best efforts, yields proved to be difficult to reproduce.

4.3.3 Mass Yield and Molar Yield Determination

Since it was challenging to remove the impurities from the crude reaction products, we attempted direct sublimation. A 1 gram scale DFF reaction (Table 9, trial 11) yielded a small amount (0.2 g) of sublimed DFF crystals. It was unclear whether sublimation was failing to separate all of the product from the reaction mixture or if the yield of pure product was intrinsically low. However, upon employing an internal NMR standard (1,4-dioxane), the purity of the sublimed DFF from the same batch revealed differences. Sublimed DFF crystals from the same batch had appeared to have different purities (see appendix Figure S3-S5 for NMR spectra with internal standard).

In a 2 g reaction (Table 10, trial 6), the mass yield was 83% and the product appeared to have a clean NMR. However, this DFF sample was found to be only 59% pure by NMR integration against an internal standard. It is unclear what the nature of the impurity is, but it is NMR-silent, suggesting it could be a highly heterogeneous, polymeric resin by-product. Furans are well known to decompose into resins. We then chromatographed the crude product using a Biotage flash chromatography

system under UV-vis monitoring (254 and 280 nm). The fractions containing DFF were collected and the purity was determined by NMR with an internal standard. Unfortunately, the chromatographed product was also shown to be impure.

4.4   Conclusions

In this chapter, the transformation of CMF to DFF by oxidation with bismuth(III) nitrate pentahydrate was explored across a wide range of conditions and scales. The results initially suggested a potential mass yield of up to 95% on sub-gram scales. However, the observed mass yields did not correspond to pure product, and attempts to isolate pure DFF using this method were unsuccessful. When attempting to scale up the process, the reaction showed poor reproducibility and yields were low, which was mainly due to the challenges associated with reaction temperature control, as well as increased difficulties in product isolation. In the end, a reproducible method for CMF oxidation to DFF using bismuth nitrate could not be established. It may be that further work on this process, focused on better dispersion of the reactants in a medium that can moderate the exotherm and avoid runaway reactions, could lead to better outcomes.

4.5   Acknowledgments

References

Mascal, M. (2015). 5-(chloromethyl)furfural is the new hmf: Functionally equivalent but more practical in terms of its production from biomass. *ChemSusChem*, *8*(20), 3391–3395.

Mascal, M. (2019). 5-(chloromethyl)furfural (cmf): A platform for transforming cellulose into commercial products. *ACS Sustainable Chemistry & Engineering*, *7*(6), 5588–5601.

Amarasekara, A. S., Green, D., & Williams, L. D. (2009). Renewable resources based polymers: Synthesis and characterization of 2,5-diformylfuran–urea resin. *European Polymer Journal*, *45*(2), 595–598.

Xiang, T., Liu, X., Yi, P., Guo, M., Chen, Y., Wesdemiotis, C., Xu, J., & Pang, Y. (2013). Schiff base polymers derived from 2,5-diformylfuran. *Polymer international*, *62*(10), 1517–1523.

Fischer, G., Hizsnyik, E., Prieler, S., Shah, M., & Van Velthuizen, H. (2009). Biofuels and food security.

Laugel, C., Estrine, B., Le Bras, J., Hoffmann, N., Marinkovic, S., & Muzart, J. (2014). Sodium Bromide DMSO-Induced Synthesis of 2,5-Diformylfuran from Fructose or 5-(Hydroxymethyl) furfural. *ChemCatChem*, *6*(5), 1195–1198.

Brasholz, M., von Känel, K., Hornung, C. H., Saubern, S., & Tsanaktsidis, J. (2011). Highly efficient dehydration of carbohydrates to 5-(chloromethyl) furfural (cmf), 5-(hydroxymethyl) furfural (hmf) and levulinic acid by biphasic continuous flow processing. *Green Chemistry*, *13*(5), 1114–1117.

Hansen, T. S., Sádaba, I., García-Suárez, E. J., & Riisager, A. (2013). Cu catalyzed oxidation of 5-hydroxymethylfurfural to 2,5-diformylfuran and 2,5-

furandicarboxylic acid under benign reaction conditions. *Applied Catalysis A: General*, *456*, 44–50.

Kompanets, M., Kushch, O., Litvinov, Y. E., Pliekhov, O., Novikova, K., Novokhatko, A., Shendrik, A., Vasilyev, A., & Opeida, I. (2014). Oxidation of 5-hydroxymethylfurfural to 2,5-diformylfuran with molecular oxygen in the presence of n-hydroxyphthalimide. *Catalysis Communications*, *57*, 60–63.

Le, N.-T., Lakshmanan, P., Cho, K., Han, Y., & Kim, H. (2013). Selective oxidation of 5-hydroxymethyl-2-furfural into 2,5-diformylfuran over vanadyl ion and copper(ii) ion immobilized on sulfonated carbon catalysts. *Applied Catalysis A: General*, *464*, 305–312.

Nie, J., Xie, J., & Liu, H. (2013). Efficient aerobic oxidation of 5-hydroxymethylfurfural to 2,5-diformylfuran on supported ru catalysts. *Journal of catalysis*, *301*, 83–91.

Jia, X., Ma, J., Wang, M., Du, Z., Lu, F., Wang, F., & Xu, J. (2014). Promoted role of $cu(no_3)_2$ on aerobic oxidation of 5-hydroxymethylfurfural to 2,5-diformylfuran over voso4. *Applied Catalysis A: General*, *482*, 231–236.

Jia, W., Du, J., Liu, H., Feng, Y., Sun, Y., Tang, X., Zeng, X., & Lin, L. (2019). An efficient approach to produce 2,5-diformylfuran from 5-hydroxymethylfurfural using air as oxidant. *Journal of Chemical Technology & Biotechnology*, *94*(12), 3832–3838.

Takagaki, A., Takahashi, M., Nishimura, S., & Ebitani, K. (2011). One-pot synthesis of 2,5-diformylfuran from carbohydrate derivatives by sulfonated resin and hydrotalcite-supported ruthenium catalysts. *ACS Catalysis*, *1*(11), 1562–1565.

Vicente, A. I., Coelho, J. A., Simeonov, S. P., Lazarova, H. I., Popova, M. D., & Afonso, C. A. (2017). Oxidation of 5-chloromethylfurfural (cmf) to 2,5-diformylfuran (dff). *Molecules*, *22*(2), 329.

Girka, Q., Estrine, B., Hoffmann, N., Le Bras, J., Marinković, S., & Muzart, J. (2016). Simple efficient one-pot synthesis of 5-hydroxymethylfurfural and 2,5-diformylfuran from carbohydrates. *Reaction Chemistry & Engineering, 1*(2), 176–182.

Mittal, N., Nisola, G. M., Malihan, L. B., Seo, J. G., Lee, S.-P., & Chung, W.-J. (2014). Metal-free mild oxidation of 5-hydroxymethylfurfural to 2,5-diformylfuran. *Korean Journal of Chemical Engineering, 31*, 1362–1367.

Mittal, N., Nisola, G. M., Seo, J. G., Lee, S.-P., & Chung, W.-J. (2015). Organic radical functionalized sba-15 as a heterogeneous catalyst for facile oxidation of 5-hydroxymethylfurfural to 2,5-diformylfuran. *Journal of Molecular Catalysis A: Chemical, 404*, 106–114.

Lv, G., Wang, H., Yang, Y., Deng, T., Chen, C., Zhu, Y., & Hou, X. (2015). Graphene oxide: A convenient metal-free carbocatalyst for facilitating aerobic oxidation of 5-hydroxymethylfurfural into 2,5-diformylfuran. *Acs Catalysis, 5*(9), 5636–5646.

5   Conclusions

In conclusion, this Ph.D. thesis has delved into diverse aspects of sustainable materials and synthetic methods, contributing to the burgeoning field of green chemistry. Chapter 2 explored the use of trifluoroacetic acid as an effective dispersing medium for cellulose nanocrystals (CNCs). This approach led to the production of a CNC-PET nanocomposite under mild conditions without specialized equipment, and also opens the door for further applications for non-surface modified CNCs.

Chapter 3 described the characterization and dyeing performance of sustainably produced colorants, as well as Knoevenagel products of carbethoxymethyl and cyanomethyl substituted furanoate esters. By making use of biobased resources, this work addresses the growing demand for sustainable alternatives in the dye industry.

Chapter 4 continues the thesis's focus on sustainability by working towards the synthesis of DFF, a key synthetic intermediate in Chapter 3, starting from CMF. This work focused on optimizing the oxidation of CMF with bismuth nitrate pentahydrate, ranging from the sub-gram scale up to the 2 gram scale, with a focus on addressing multiple confounding issues that resulted when the reaction was scaled.

In total, the thematically interconnected chapters of this thesis underscore the importance of the development of sustainable practices in chemical production and materials science. The research outcomes presented here not only expand the fundamental understanding of these systems but also contribute to practical solutions toward a more sustainable and environmentally conscious future.

A Appendix for Chapter 3: Butenolide Derivatives of Biobased Furans: Sustainable Synthetic Dyes

A.1 Results from Dye Tests
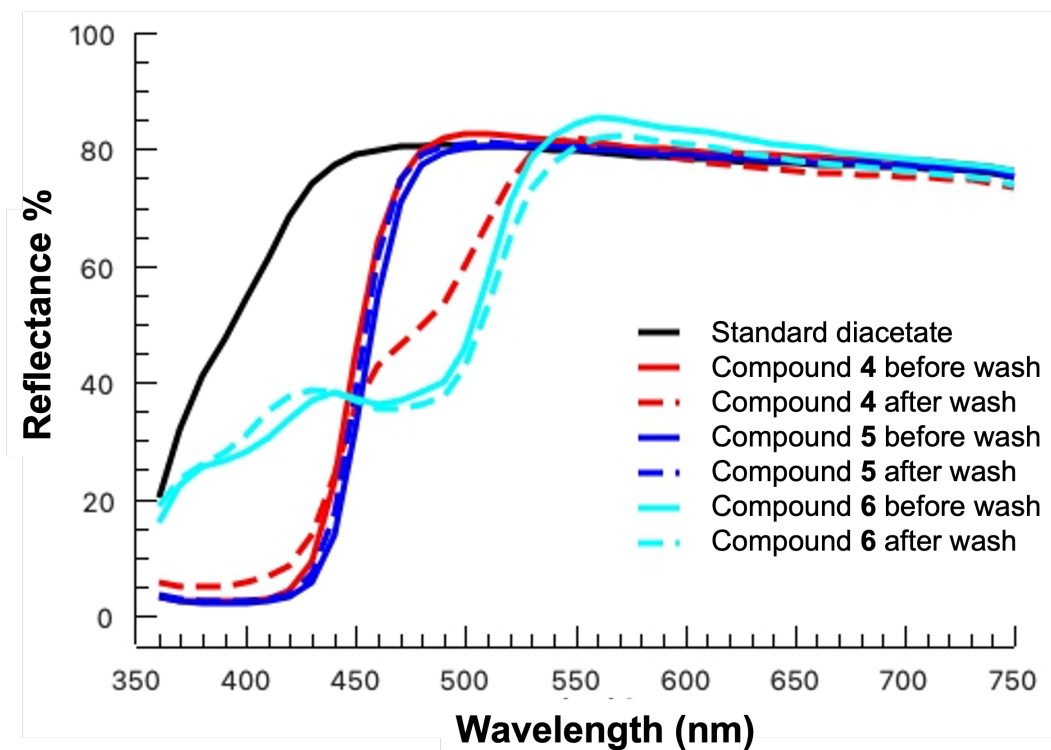
Figure S1: Reflectance spectra of cellulose diacetate dyed using compounds **4**, **5**, and **6**. Color scanned under standard illuminant D65 from the dry fabrics before and after washing.

Figure S2: A comparison of color reflectance on cellulose diacetate dyed using compounds **4-8**. The presented colors were scanned under standard illuminant D65 from the dry fabrics before and after washing.
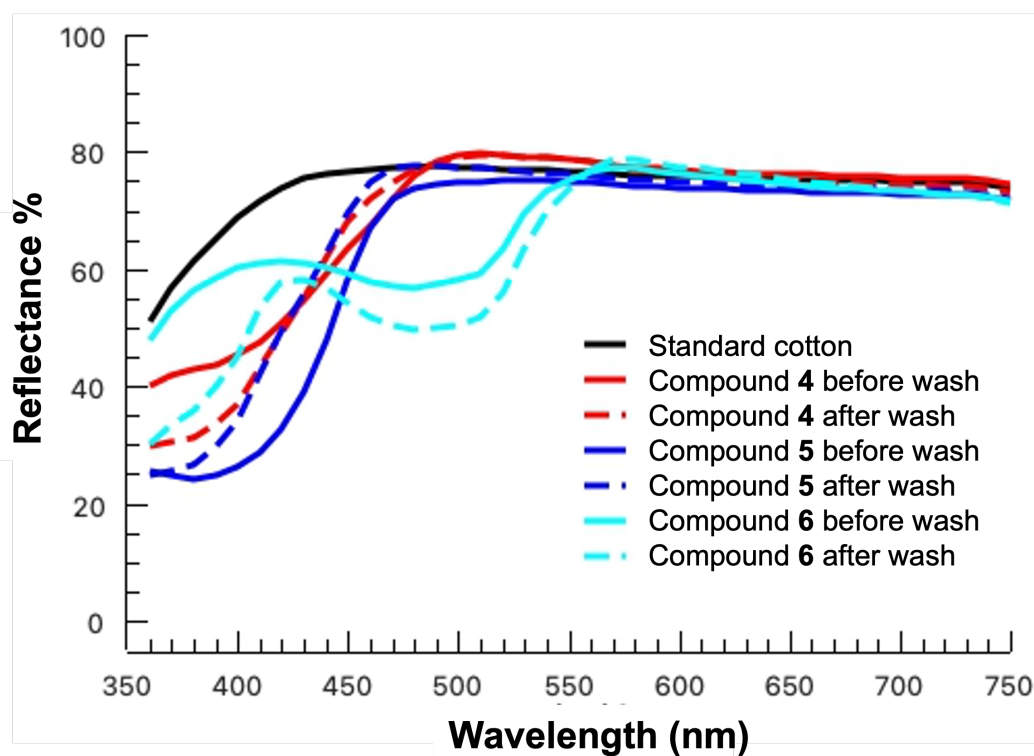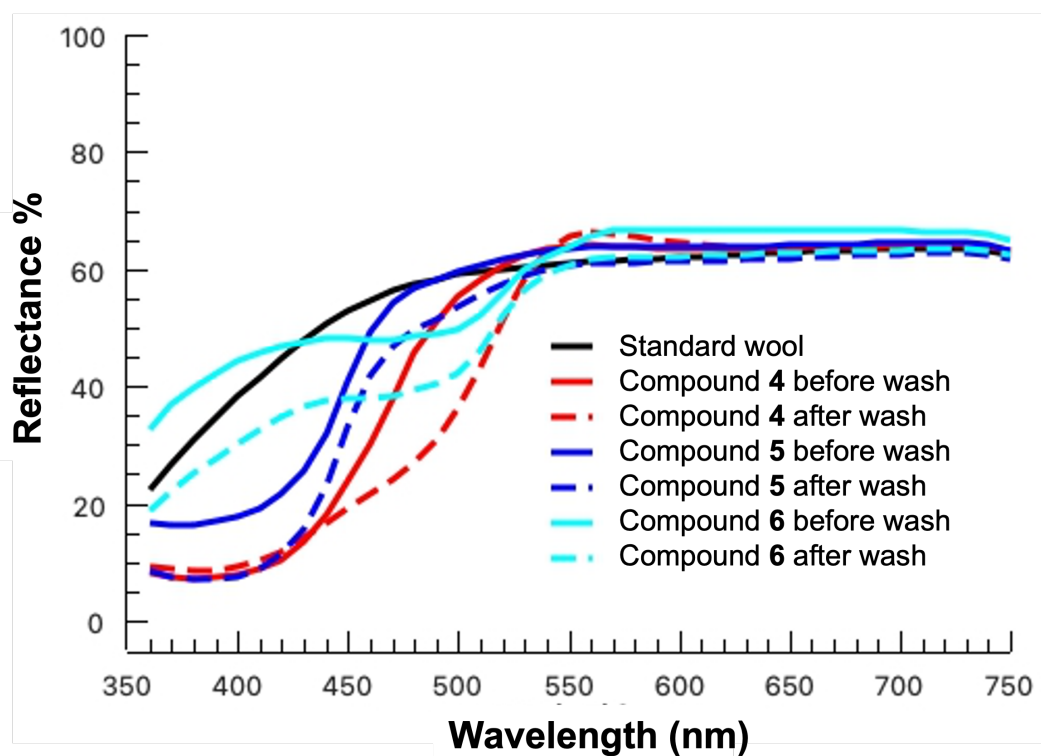
Figure S3: Reflectance spectra of cotton dyed using compounds **4**, **5**, and **6**, with colors scanned under standard illuminant D65 from the dry fabrics before and after washing.

Compound	4	5	6	7	8
Before wash					
After wash					

Fabric type: cotton

Figure S4: A comparison of color reflectance on cotton dyed using compounds **4-8**. The presented colors were scanned under standard illuminant D65 from the dry fabrics before and after washing.
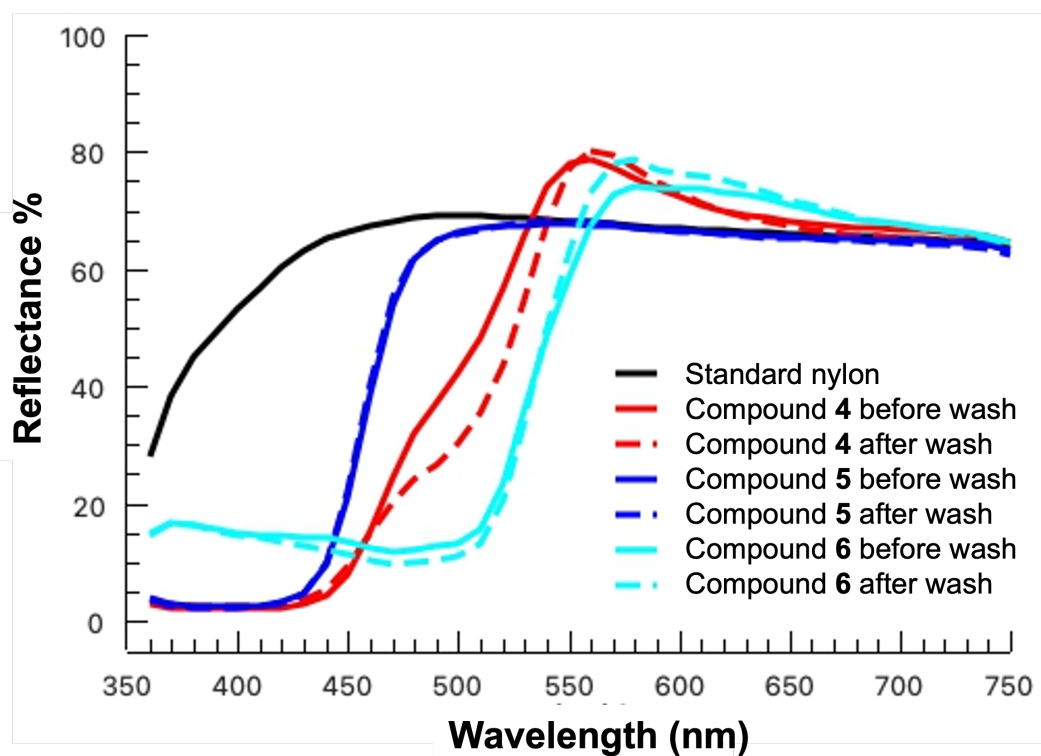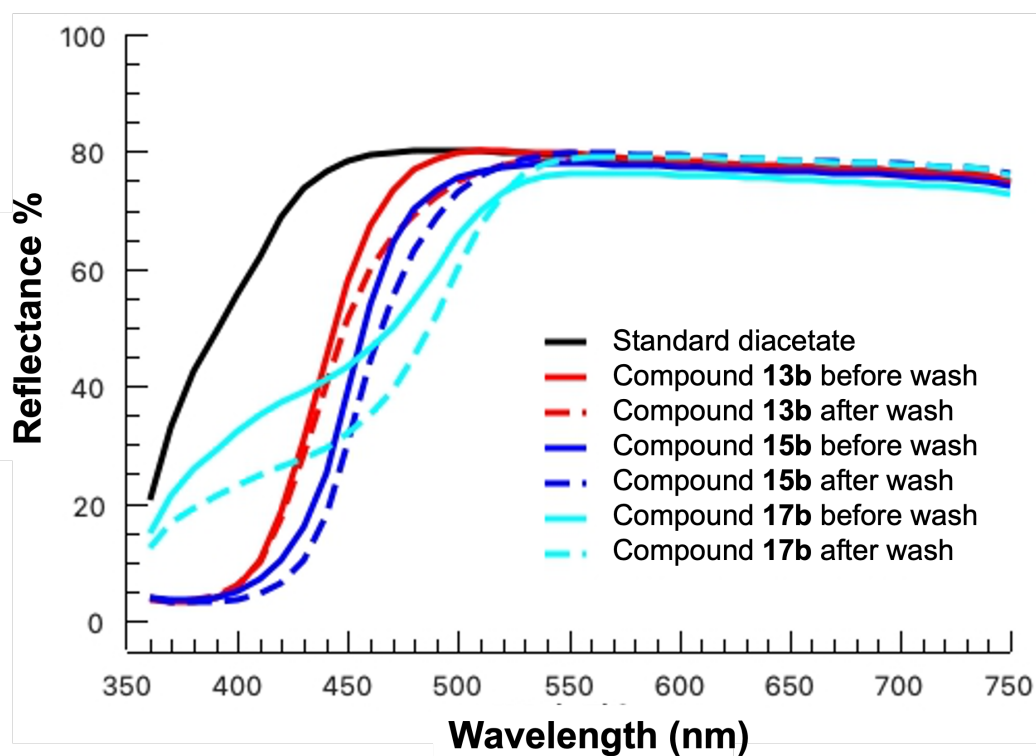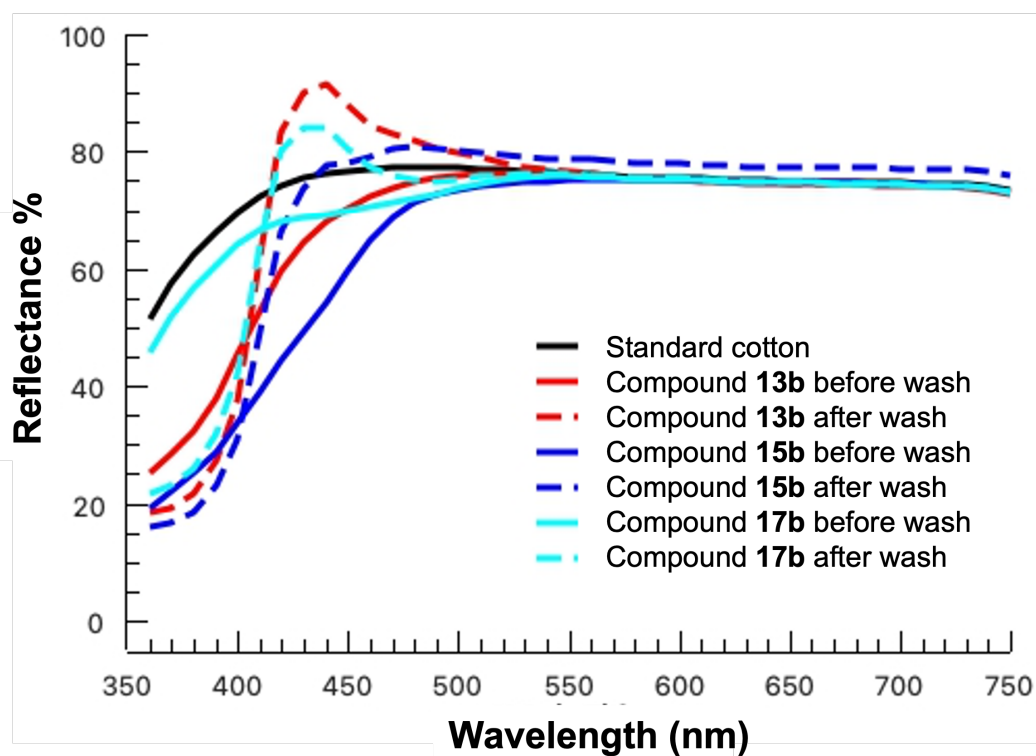
Figure S5: Reflectance spectra of nylon dyed using compounds **4**, **5**, and **6**. Color scanned under standard illuminant D65 from the dry fabrics before and after washing.

Compound	4	5	6	7	8
Before wash					
After wash					

Fabric type: nylon

Figure S6: A comparison of color reflectance on nylon dyed using compounds **4-8**. The presented colors were scanned under standard illuminant D65 from the dry fabrics before and after washing.
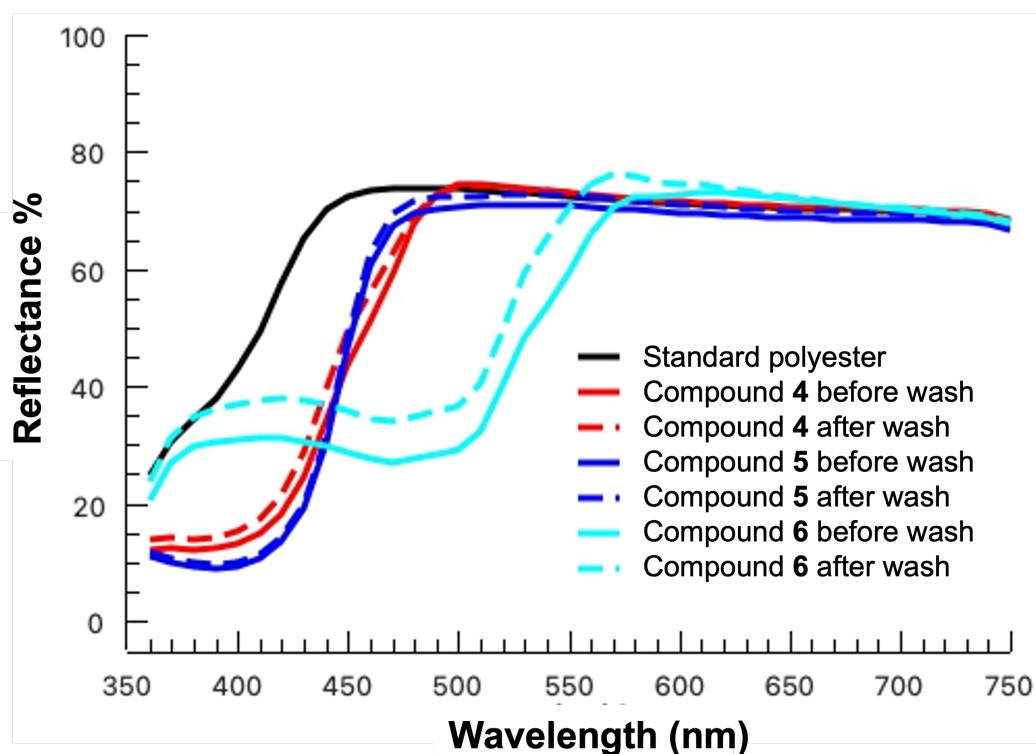
Figure S7: Reflectance spectra of Dacron 54 polyester dyed using compounds **4**, **5**, and **6**. Color scanned under standard illuminant D65 from the dry fabrics before and after washing.

Compound	4	5	6	7	8
Before wash					
After wash					

Fabric type: polyester

Figure S8: A comparison of color reflectance on Dacron 54 polyester dyed using compounds **4-8**. The presented colors were scanned under standard illuminant D65 from the dry fabrics before and after washing.
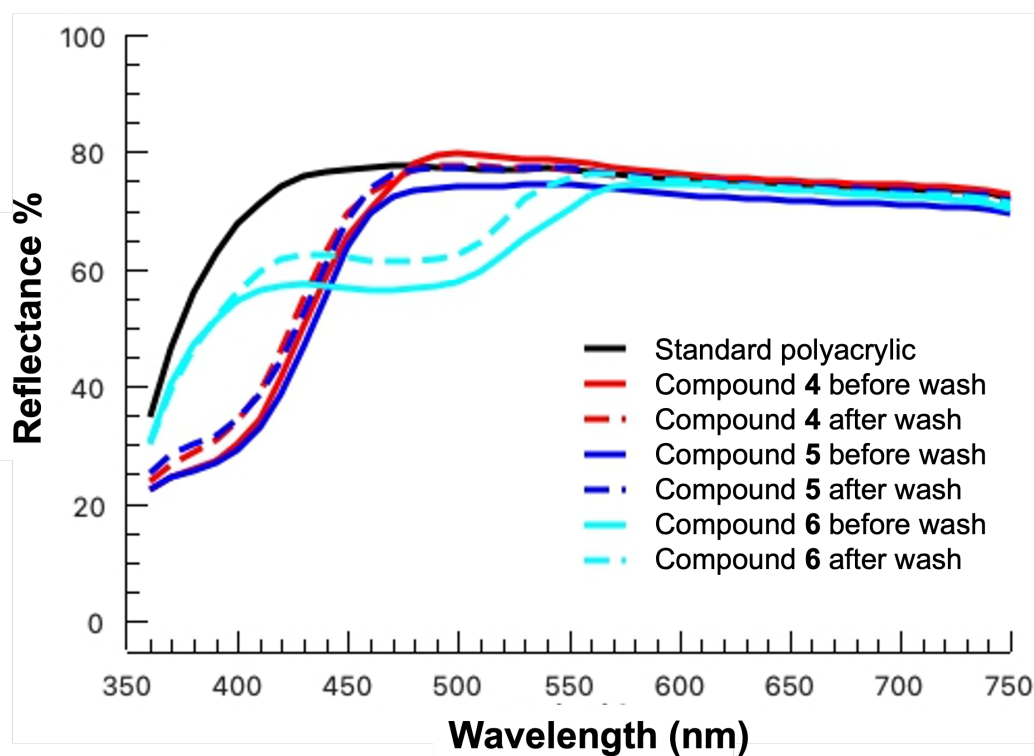
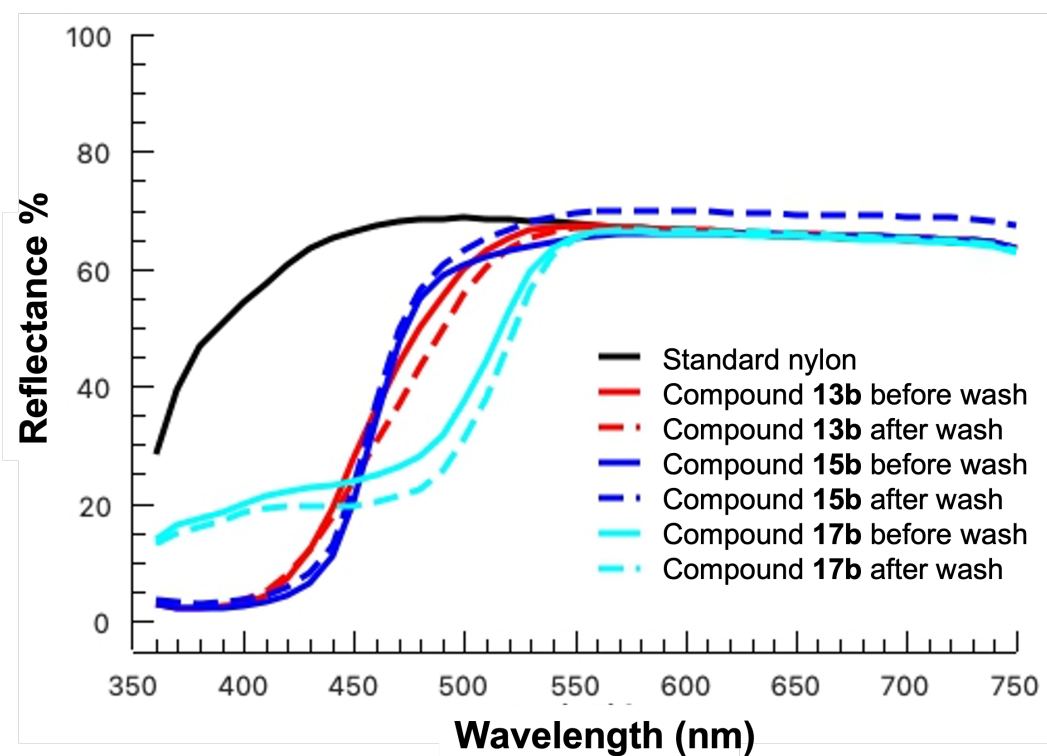Figure S9: Reflectance spectra of Dralon polyacrylic dyed using compounds **4**, **5**, and **6**. Color scanned under standard illuminant D65 from the dry fabrics before and after washing.

Figure S10: A comparison of color reflectance on Dralon polyacrylic dyed using compounds **4-8**. The presented colors were scanned under standard illuminant D65 from the dry fabrics before and after washing.
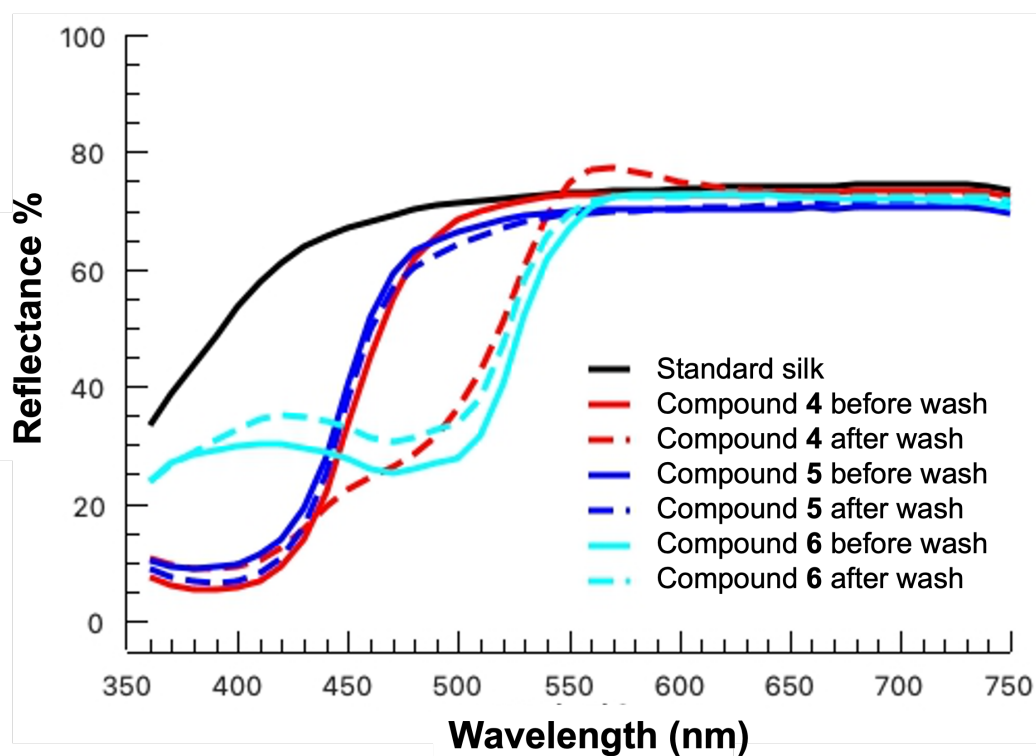
Figure S11: Reflectance spectra of silk dyed using compounds **4**, **5**, and **6**. Color scanned under standard illuminant D65 from the dry fabrics before and after washing.

Figure S12: A comparison of color reflectance on silk dyed using compounds **4-8**. The presented colors were scanned under standard illuminant D65 from the dry fabrics before and after washing.
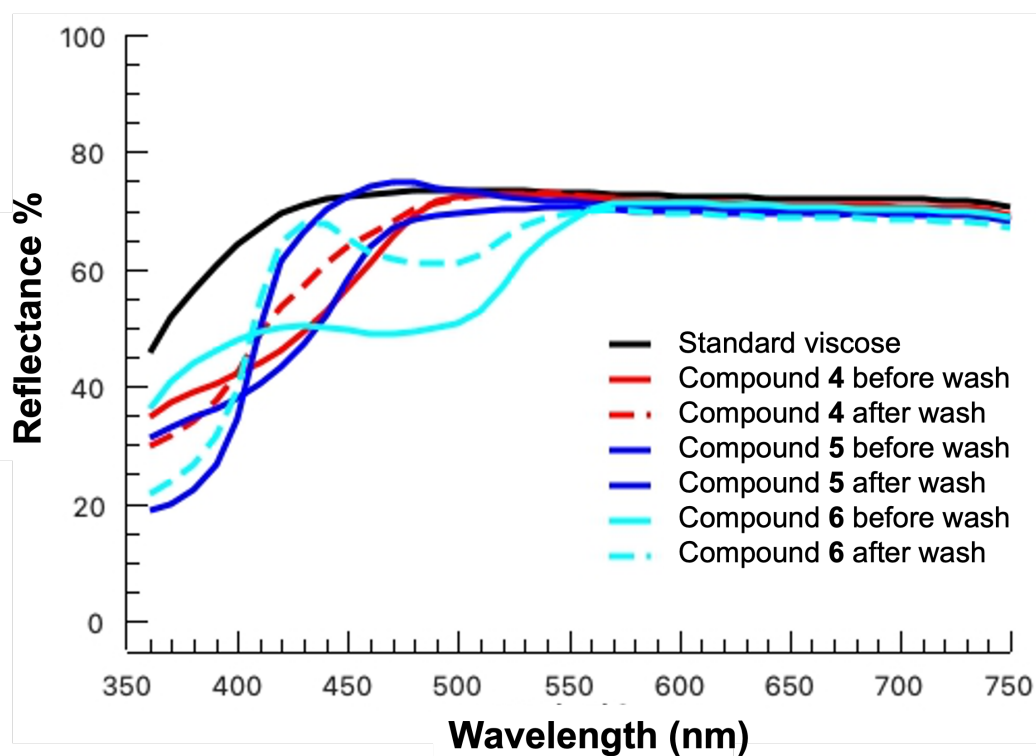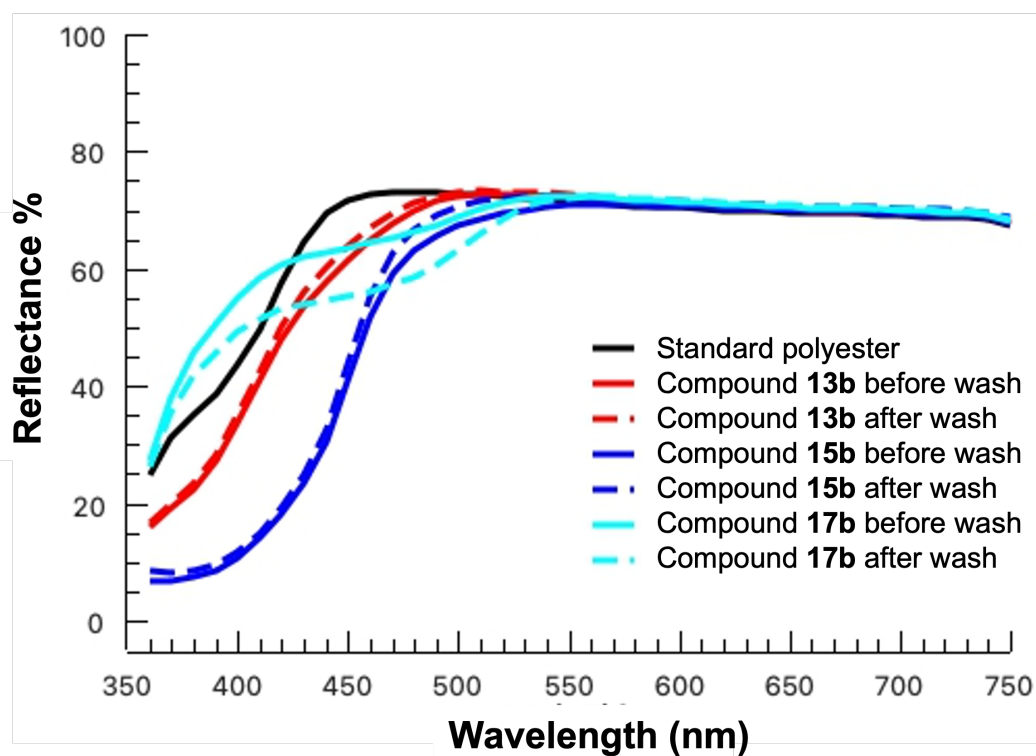
Figure S13: Reflectance spectra of viscose dyed using compounds **4**, **5**, and **6**. Color scanned under standard illuminant D65 from the dry fabrics before and after washing.

Compound	4	5	6	7	8
Before wash					
After wash					

Fabric type: viscose

Figure S14: A comparison of color reflectance on viscose dyed using compounds **4-8**. The presented colors were scanned under standard illuminant D65 from the dry fabrics before and after washing.
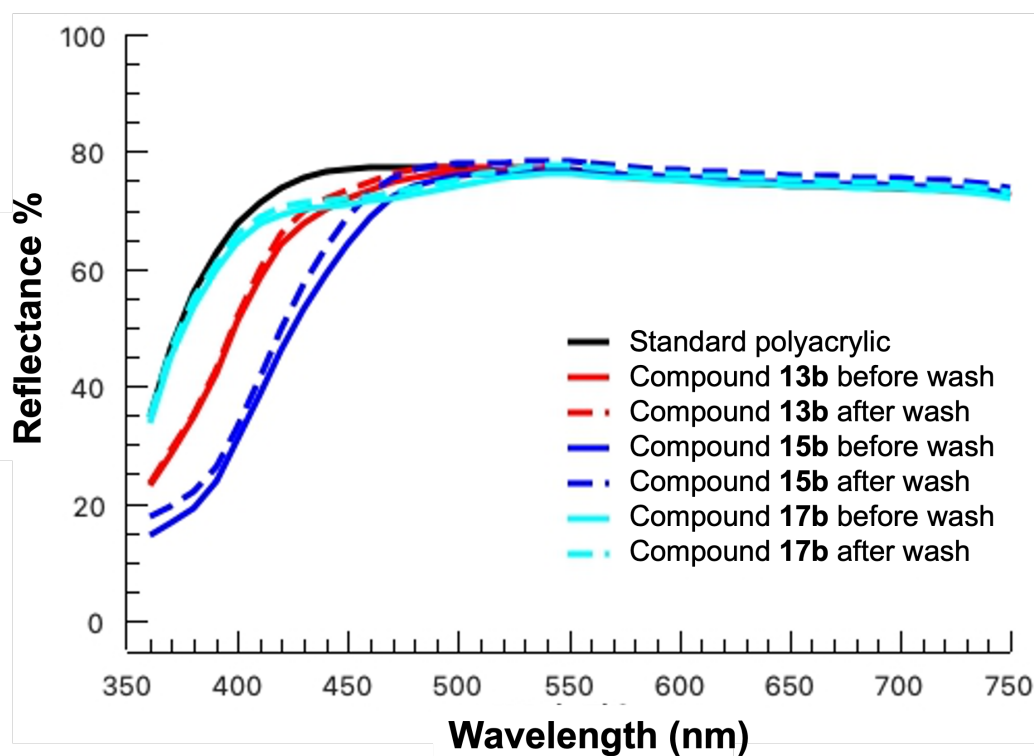
Figure S15: Reflectance spectra of wool dyed using compounds **4**, **5**, and **6**. Color scanned under standard illuminant D65 from the dry fabrics before and after washing.

Figure S16: A comparison of color reflectance on wool dyed using compounds **4-8**. The presented colors were scanned under standard illuminant D65 from the dry fabrics before and after washing.

Figure S17: Reflectance spectra of cellulose diacetate dyed using compounds **13b**, **15b**, and **17b**. Color scanned under standard illuminant D65 from the dry fabrics before and after washing.

Figure S18: A comparison of color reflectance on cellulose diacetate dyed using compounds **13b**, **15b**, and **17b**. The presented colors were scanned under standard illuminant D65 from the dry fabrics before and after washing.
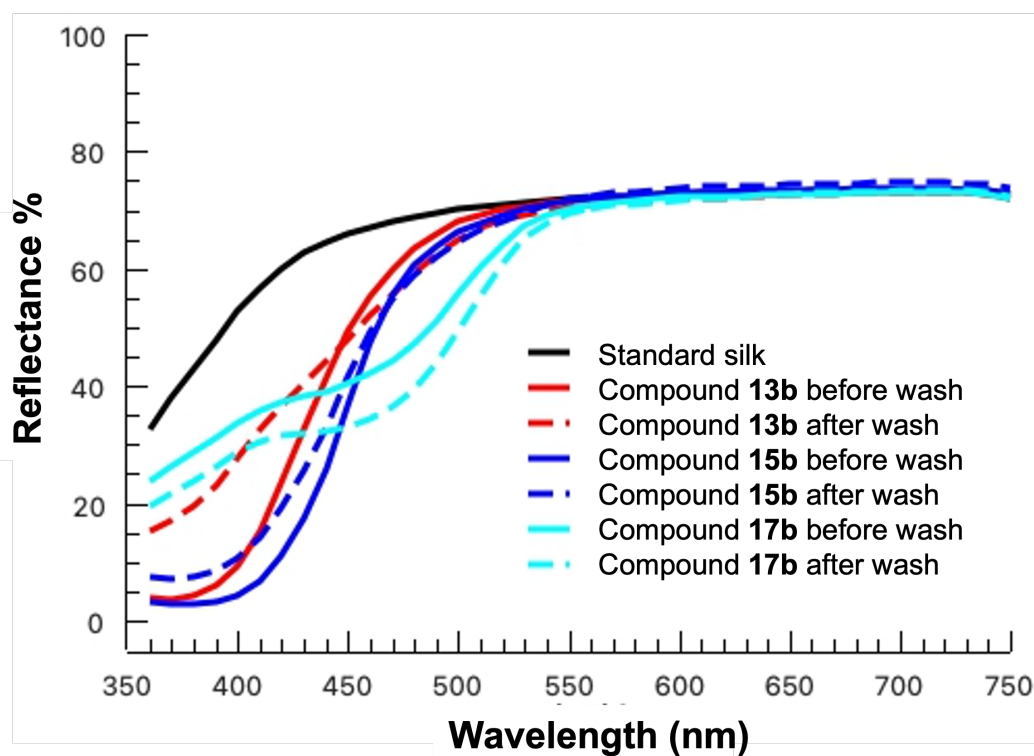
Figure S19: Reflectance spectra of cotton dyed using compounds **13b**, **15b**, and **17b**. Color scanned under standard illuminant D65 from the dry fabrics before and after washing.

Compound	13b	15b	17b
Before wash			
After wash			

Fabric type: cotton

Figure S20: A comparison of color reflectance on cotton dyed using compounds **13b**, **15b**, and **17b**. The presented colors were scanned under standard illuminant D65 from the dry fabrics before and after washing.

Figure S21: Reflectance spectra of nylon dyed using compounds **13b**, **15b**, and **17b**. Color scanned under standard illuminant D65 from the dry fabrics before and after washing.

Compound	13b	15b	17b
Before wash			
After wash			

Fabric type: nylon

Figure S22: A comparison of color reflectance on nylon dyed using compounds **13b**, **15b**, and **17b**. The presented colors were scanned under standard illuminant D65 from the dry fabrics before and after washing.

Figure S23: Reflectance spectra of Dacron 54 polyester dyed using compounds **13b**, **15b**, and **17b**. Color scanned under standard illuminant D65 from the dry fabrics before and after washing.

Compound	13b	15b	17b
Before wash			
After wash			

Fabric type: polyester

Figure S24: A comparison of color reflectance on Dacron 54 polyester dyed using compounds **13b**, **15b**, and **17b**. The presented colors were scanned under standard illuminant D65 from the dry fabrics before and after washing.
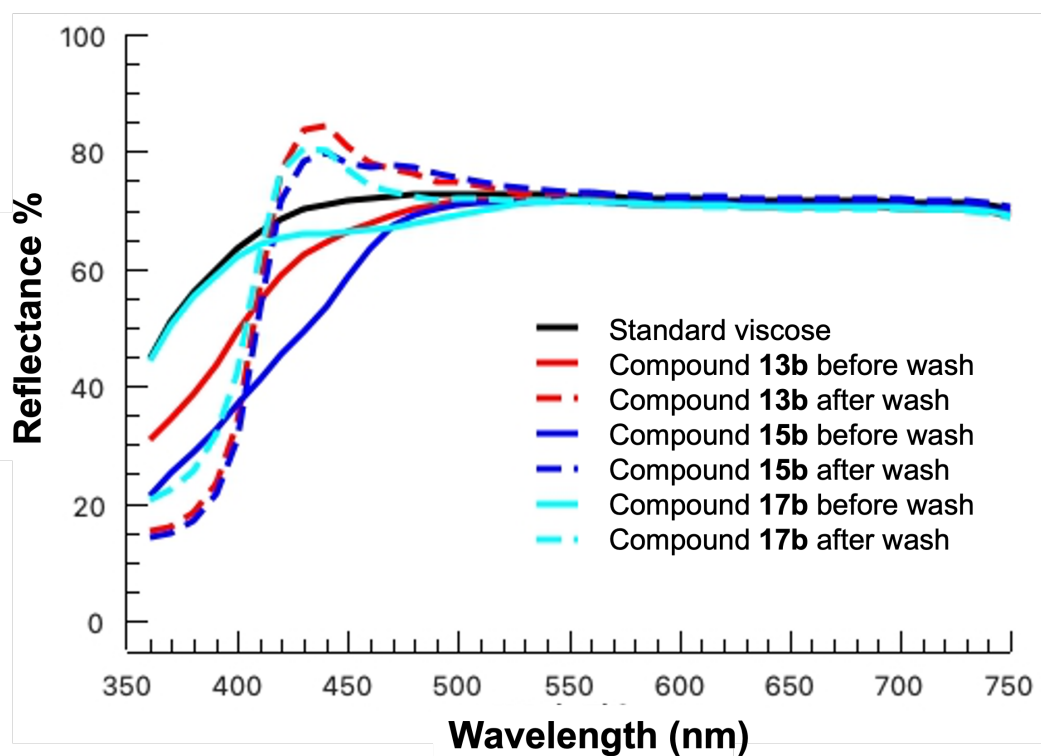
Figure S25: Reflectance spectra of Dralon polyacrylic dyed using compounds **13b**, **15b**, and **17b**. Color scanned under standard illuminant D65 from the dry fabrics before and after washing.

Compound	13b	15b	17b
Before wash			
After wash			

Fabric type: polyacrylic

Figure S26: A comparison of color reflectance on Dralon polyacrylic dyed using compounds **13b**, **15b**, and **17b**. The presented colors were scanned under standard illuminant D65 from the dry fabrics before and after washing.
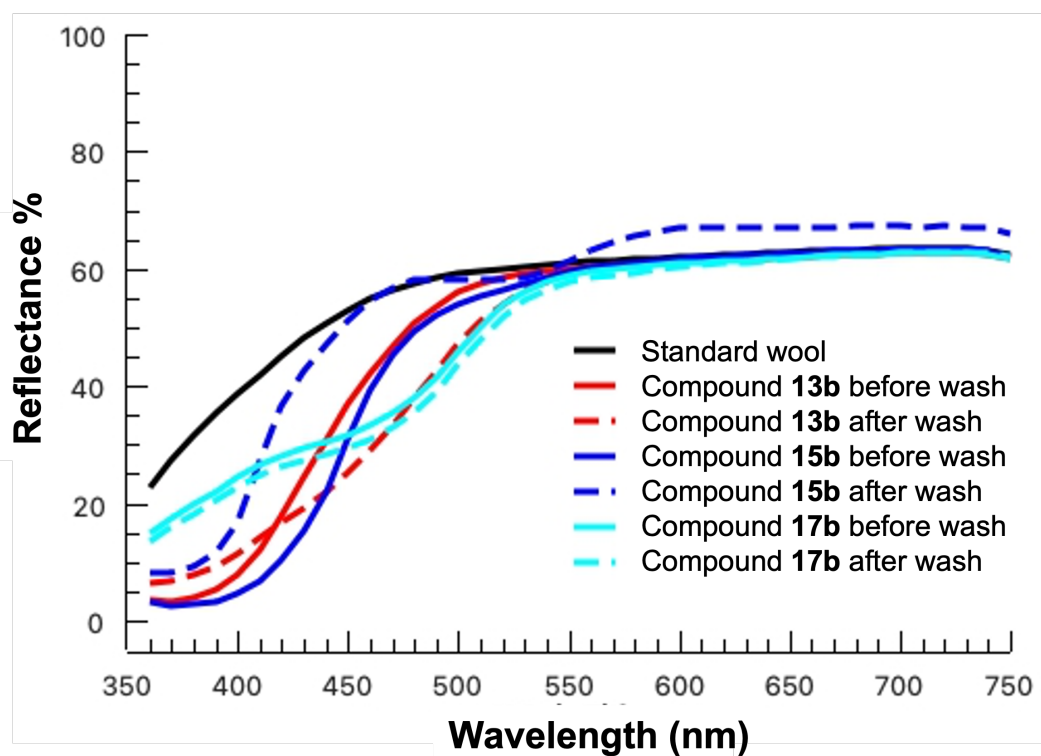
Figure S27: Reflectance spectra of silk dyed using compounds **13b**, **15b**, and **17b**. Color scanned under standard illuminant D65 from the dry fabrics before and after washing.

Figure S28: A comparison of color reflectance on silk dyed using compounds **13b**, **15b**, and **17b**. The presented colors were scanned under standard illuminant D65 from the dry fabrics before and after washing.

Figure S29: Reflectance spectra of viscose dyed using compounds **13b**, **15b**, and **17b**. Color scanned under standard illuminant D65 from the dry fabrics before and after washing.

Figure S30: A comparison of color reflectance on viscose dyed using compounds **13b**, **15b**, and **17b**. The presented colors were scanned under standard illuminant D65 from the dry fabrics before and after washing.

Figure S31: Reflectance spectra of wool dyed using compounds **13b**, **15b**, and **17b**. Color scanned under standard illuminant D65 from the dry fabrics before and after washing.

Figure S32: A comparison of color reflectance on wool dyed using compounds **13b**, **15b**, and **17b**. The presented colors were scanned under standard illuminant D65 from the dry fabrics before and after washing.

Table S1: Fabrics dyed and washed with compounds **4**, **5**, and **6**. The fabrics were scanned and the results were presented in the CIELAB color space. Diacetate: cellulose diacetate; Nylon: nylon 6-6; Polyester: Dacron 54 polyester.

Fabric	Compound	DL*	Da*	Db*	DC*	DH*	DEcmc
Diacetate	D4	-2.83	-7.55	36.15	36.83	-2.75	51.35
Diacetate	W4	-7.27	-0.94	36.97	36.77	-3.94	51.48
Diacetate	D5	-18.34	24.83	82.02	85.20	-9.16	119.31
Diacetate	W5	-16.12	19.23	75.02	77.00	-8.32	107.82
Diacetate	D6	-14.13	26.30	69.66	73.90	-9.12	103.64
Diacetate	W6	-15.70	23.95	65.24	68.94	-8.72	96.77
Cotton	D4	-0.06	-1.45	4.79	5.00	-0.21	7.49
Cotton	W4	0.80	1.21	-5.78	4.95	3.22	8.84
Cotton	D5	-2.52	-0.16	13.10	13.06	-1.03	19.61
Cotton	W5	-0.62	2.14	-1.39	1.68	-1.93	3.83
Cotton	D6	-2.69	4.40	8.49	9.38	-1.85	14.33
Cotton	W6	-0.52	5.48	-5.83	7.06	-3.76	11.97
Nylon	D4	-11.08	2.18	42.32	41.32	-9.38	62.42
Nylon	W4	-12.92	3.03	42.78	41.83	-9.49	63.22
Nylon	D5	-25.77	24.84	61.53	65.14	-12.62	97.98
Nylon	W5	-23.76	22.71	59.24	62.24	-12.30	93.66
Nylon	D6	-23.34	34.64	64.99	72.40	-13.51	108.59
Nylon	W6	-23.70	31.72	64.07	70.25	-13.25	105.44
Polyester	D4	-1.43	-3.77	13.96	14.25	-2.46	21.50
Polyester	W4	-0.82	-5.00	14.26	14.93	-2.33	22.47
Polyester	D5	-6.88	3.75	39.65	39.44	-5.54	59.26
Polyester	W5	-5.90	2.83	38.21	37.94	-5.36	57.01
Polyester	D6	-10.83	17.44	39.95	43.03	-6.95	64.92
Polyester	W6	-11.23	16.79	38.76	41.68	-6.83	62.92

Table S2: Fabrics dyed and washed with compounds **4**, **5**, and **6**. The fabrics were scanned and the results are presented in the CIELAB color space. Polyacrylic: Dralon polyacrylic.

Fabric	Compound	DL*	Da*	Db*	DC*	DH*	DEcmc
Polyacrylic	D4	0.15	-2.63	7.67	7.99	-1.34	11.89
Polyacrylic	W4	-0.24	-3.15	8.87	9.30	-1.43	13.80
Polyacrylic	D5	-1.38	-3.21	18.04	18.15	-2.57	26.89
Polyacrylic	W5	-0.96	-3.51	16.97	17.16	-2.41	25.41
Polyacrylic	D6	-5.07	6.80	19.95	20.61	-4.43	30.97
Polyacrylic	W6	-5.33	7.22	19.65	20.45	-4.48	30.76
Silk	D4	-8.73	0.73	26.48	26.47	-0.97	27.83
Silk	W4	-9.69	2.17	18.86	18.92	-1.56	20.15
Silk	D5	-18.68	14.61	49.81	51.62	-5.48	54.76
Silk	W5	-13.16	8.78	30.17	31.15	-4.11	33.29
Silk	D6	-15.94	18.96	42.47	45.96	-7.13	49.22
Silk	W6	-15.88	13.56	34.61	36.73	-5.69	39.48
Viscose	D4	-1.13	-1.93	5.46	5.79	0.18	8.29
Viscose	W4	-1.43	1.06	-4.52	2.70	3.78	6.69
Viscose	D5	-2.59	-0.79	12.08	12.09	-0.63	17.33
Viscose	W5	-1.93	2.73	-0.84	1.51	-2.42	4.16
Viscose	D6	-3.88	4.09	7.72	8.50	-2.01	12.57
Viscose	W6	-5.26	5.79	-2.70	4.84	-4.17	9.35
Wool	D4	-5.47	-1.18	29.78	29.79	-1.03	28.91
Wool	W4	-4.45	3.25	25.15	25.20	-2.88	24.72
Wool	D5	-11.88	9.58	46.13	46.81	-5.39	46.03
Wool	W5	-7.71	9.24	31.90	32.76	-5.45	32.62
Wool	D6	-11.10	13.55	36.11	37.91	-7.06	38.05
Wool	W6	-7.56	10.15	33.27	34.30	-5.79	34.16

Table S3: Fabrics dyed and washed with compounds **13b**, **15b**, and **17b**. The fabrics were scanned and the results were presented in the CIELAB color space. Diacetate: cellulose diacetate; Nylon: nylon 6-6; Polyester: Dacron 54 polyester.

Fabric	Compound	DL*	Da*	Db*	DC*	DH*	DEcmc
Diacetate	D13b	0.13	-7.83	19.16	20.50	-2.87	24.84
Diacetate	W13b	-0.39	-7.21	22.80	23.62	-3.77	28.70
Diacetate	D15b	-0.75	-10.27	31.27	32.62	-4.39	39.49
Diacetate	W15b	-0.82	-10.98	40.97	42.04	-5.64	50.88
Diacetate	D17b	-2.87	-4.20	39.09	38.69	-7.02	47.22
Diacetate	W17b	-2.13	-4.01	35.00	34.61	-6.55	42.31
Cotton	D13b	-0.43	-1.99	4.98	4.75	-2.49	7.69
Cotton	W13b	0.46	1.54	-6.12	5.30	3.43	9.07
Cotton	D15b	-1.04	-3.88	12.67	12.52	-4.33	19.01
Cotton	W15b	1.33	-1.22	1.81	1.81	-1.22	3.16
Cotton	D17b	-0.64	-0.43	4.10	3.29	-2.49	5.93
Cotton	W17b	-0.20	1.76	-2.39	1.67	2.45	4.27
Nylon	D13b	-1.91	-9.20	37.62	38.10	-6.90	48.86
Nylon	W13b	-2.60	-7.91	41.81	41.84	-7.75	53.70
Nylon	D15b	-2.46	-10.41	41.35	42.03	-7.20	53.80
Nylon	W15b	-0.57	-10.21	41.29	41.91	-7.23	53.66
Nylon	D17b	-5.11	1.61	39.02	37.91	-9.37	49.35
Nylon	W17b	-6.12	4.24	44.83	43.77	-10.58	56.91
Polyester	D13b	-0.05	-2.49	7.35	7.33	-2.53	9.45
Polyester	W13b	0.23	-2.03	5.90	5.85	-2.17	7.61
Polyester	D15b	-1.33	-6.86	24.63	24.95	-5.57	31.06
Polyester	W15b	-0.48	-7.73	23.18	23.91	-5.05	29.68
Polyester	D17b	-0.26	0.50	4.35	3.38	-2.78	5.42
Polyester	W17b	-1.04	0.76	10.45	9.29	-4.85	12.85

Table S4: Fabrics dyed and washed with compounds **13b**, **15b**, and **17b**. The fabrics were scanned and the results were presented in the CIELAB color space. Polyacrylic: Dralon polyacrylic.

Fabric	Compound	DL*	Da*	Db*	DC*	DH*	DEcmc
Polyacrylic	D13b	-0.23	-1.52	3.76	3.40	-2.21	5.70
Polyacrylic	W13b	0.03	-1.34	2.89	2.61	-1.82	4.48
Polyacrylic	D15b	-0.39	-3.91	10.50	10.44	-4.08	15.73
Polyacrylic	W15b	0.40	-3.58	8.40	8.42	-3.52	12.82
Polyacrylic	D17b	-0.58	-0.30	3.28	2.37	-2.29	4.64
Polyacrylic	W17b	-0.03	-0.36	3.43	2.53	-2.35	4.86
Silk	D13b	-0.74	-5.57	16.11	17.00	1.29	18.06
Silk	W13b	-1.38	-3.25	13.92	14.29	0.40	15.13
Silk	D15b	-1.09	-8.17	27.23	28.40	1.30	30.09
Silk	W15b	-1.02	-5.31	22.69	23.29	0.55	24.65
Silk	D17b	-2.53	-0.83	19.78	19.76	-1.19	20.97
Silk	W17b	-3.65	-0.07	26.86	26.79	-1.85	28.47
Viscose	D13b	-0.57	-1.53	3.61	3.84	-0.83	5.47
Viscose	W13b	0.19	1.45	-5.82	3.70	4.72	8.40
Viscose	D15b	-0.74	-3.71	9.84	10.40	-1.62	14.65
Viscose	W15b	0.63	0.37	-3.33	1.25	3.11	4.71
Viscose	D17b	-0.81	-0.02	2.69	2.40	-1.21	3.76
Viscose	W17b	-0.39	1.79	-4.29	2.24	4.07	6.51
Wool	D13b	-1.10	-4.86	16.25	16.94	0.90	15.58
Wool	W13b	-2.70	-2.92	27.37	27.50	-1.16	25.27
Wool	D15b	-1.57	-5.27	22.68	23.28	0.38	21.35
Wool	W15b	1.70	2.06	4.01	3.88	-2.31	4.63
Wool	D17b	-2.79	-0.22	18.57	18.48	-1.86	17.13
Wool	W17b	-3.53	0.44	20.53	20.41	-2.34	18.99

A.2   UV-vis Spectra
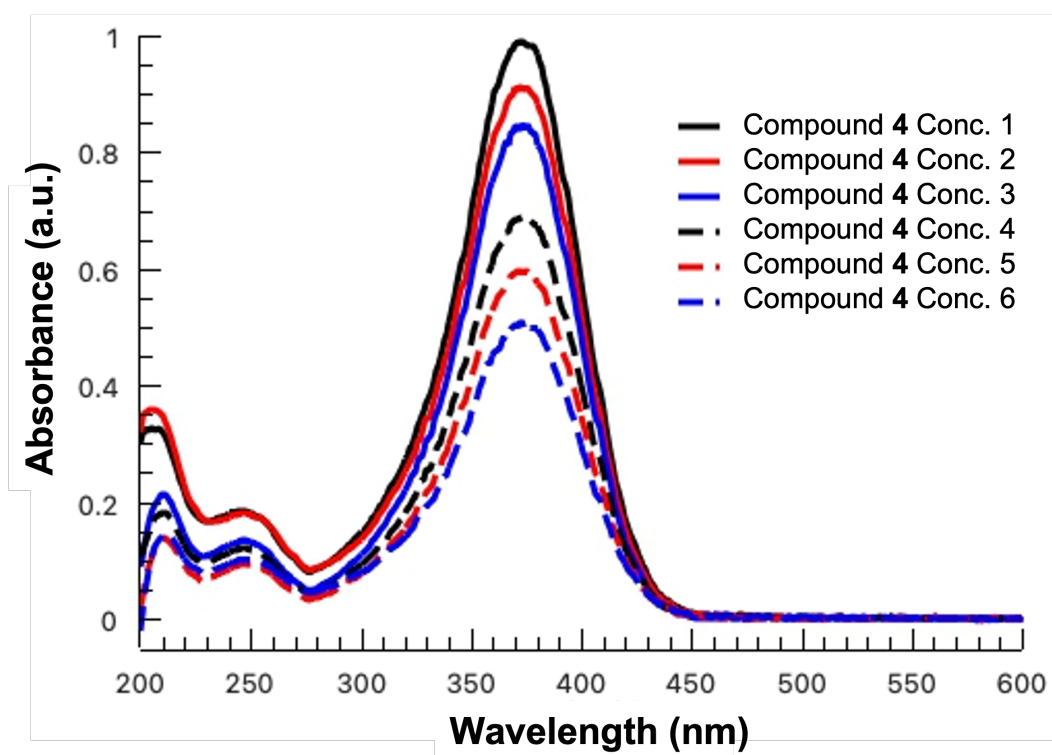
Figure S33: UV-vis spectra of compound **04** at various concentrations, with maximum absorption at 374 nm.
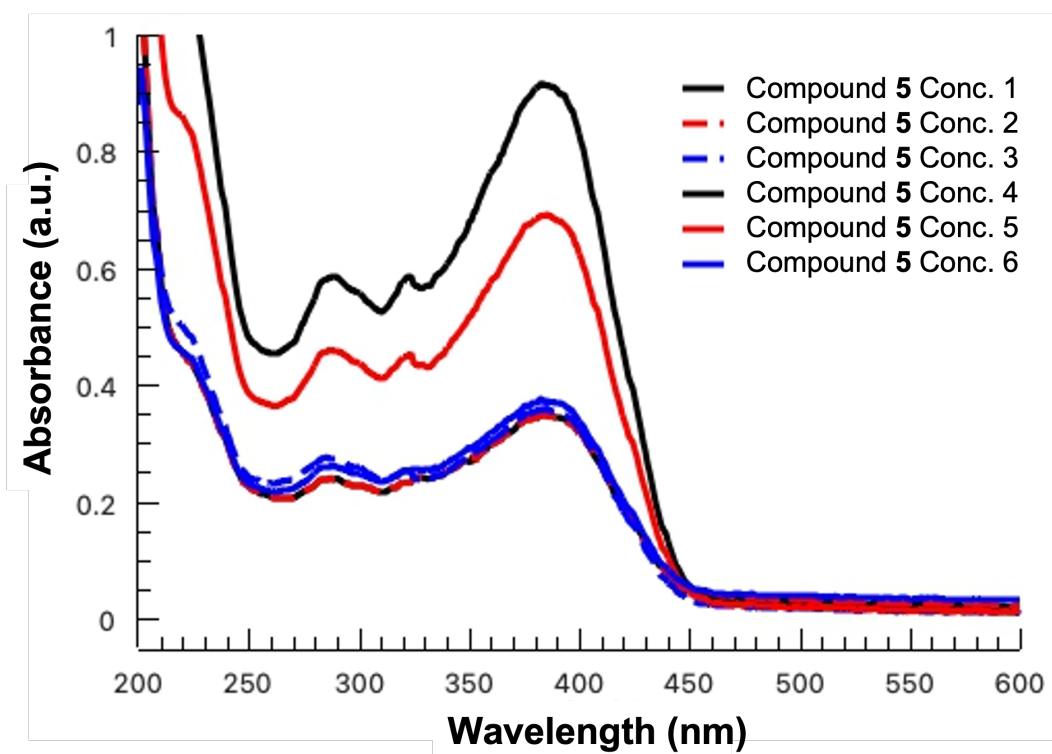
Figure S34: UV-vis spectra of compound **05** at various concentrations, with maximum absorption at 385 nm.
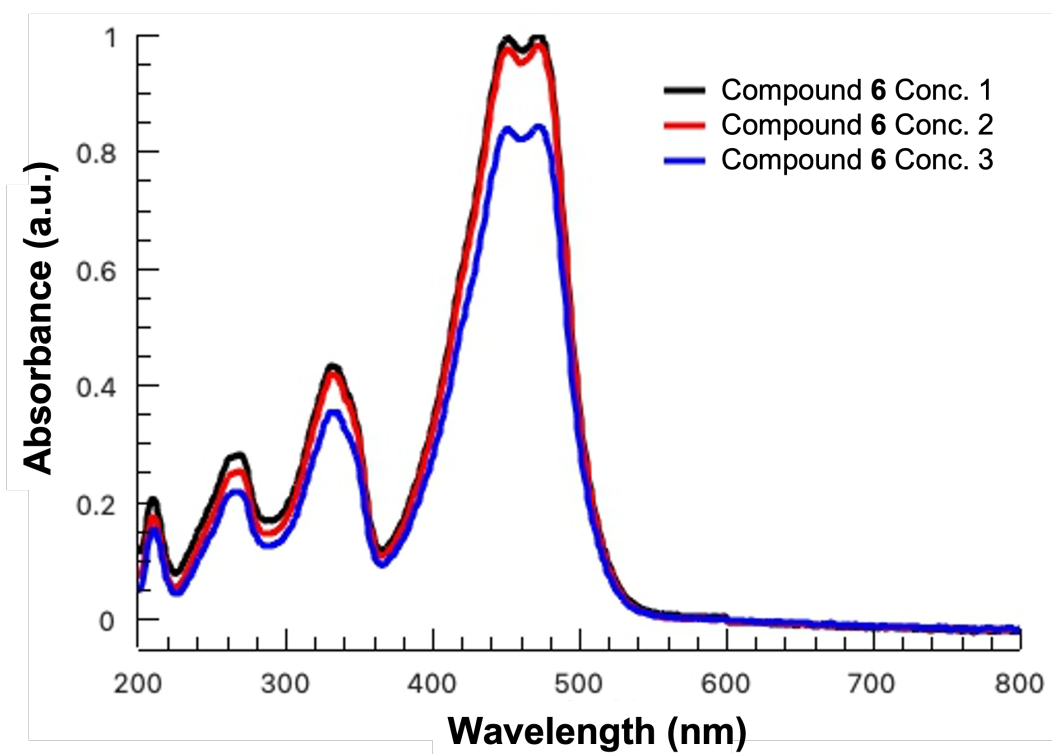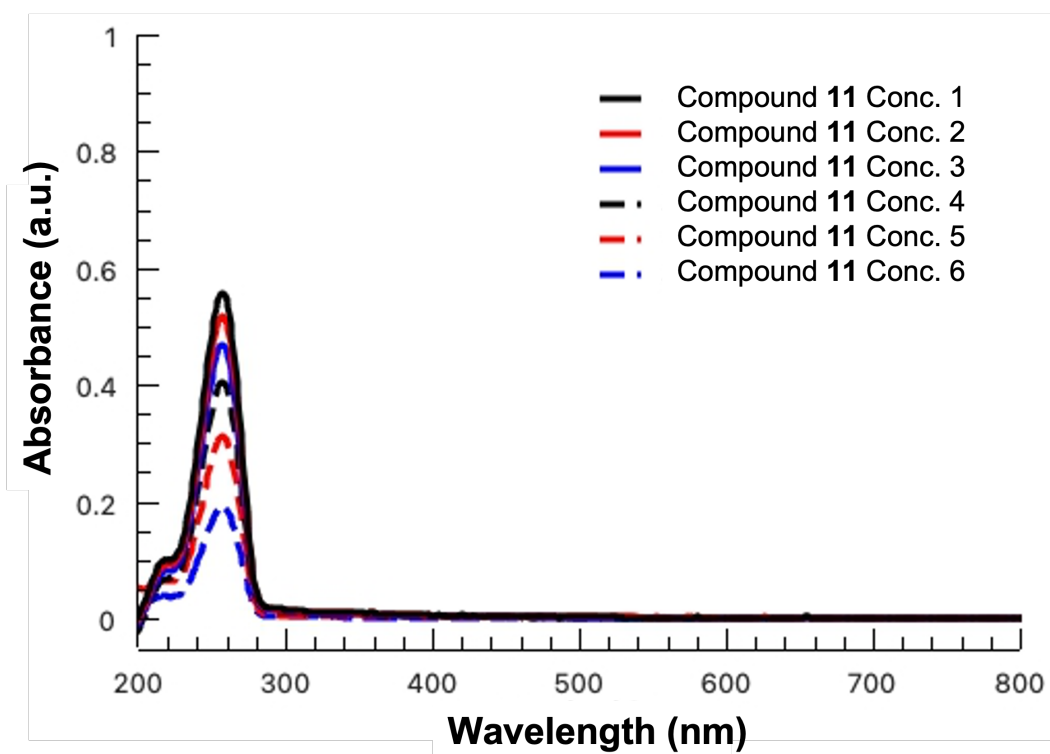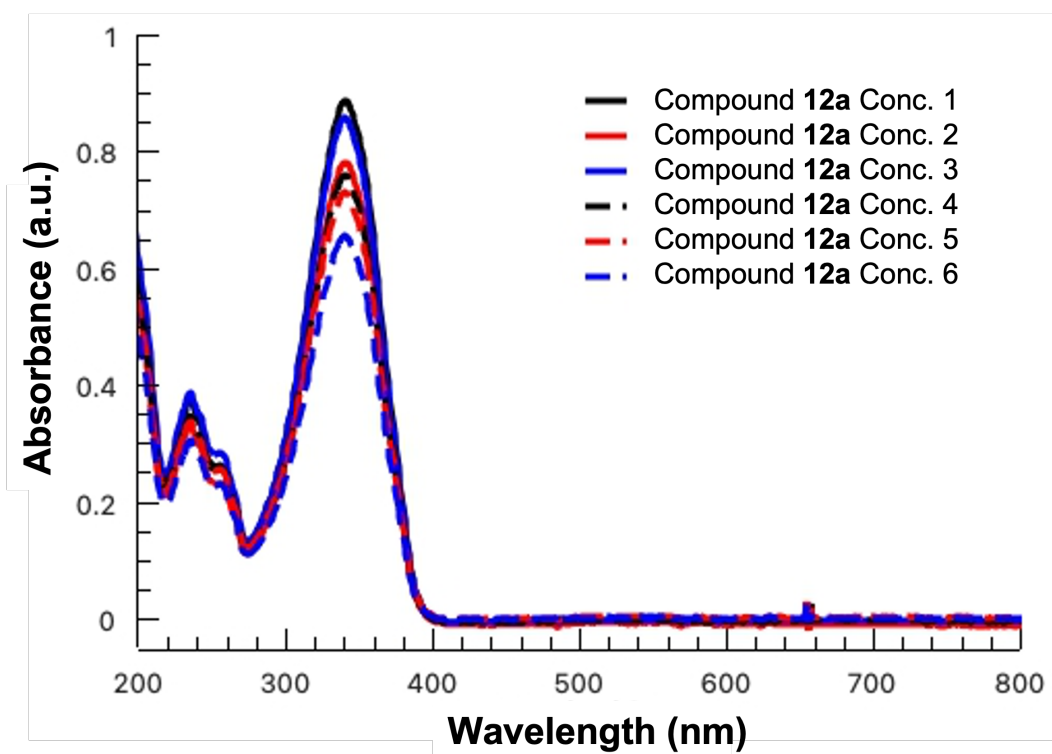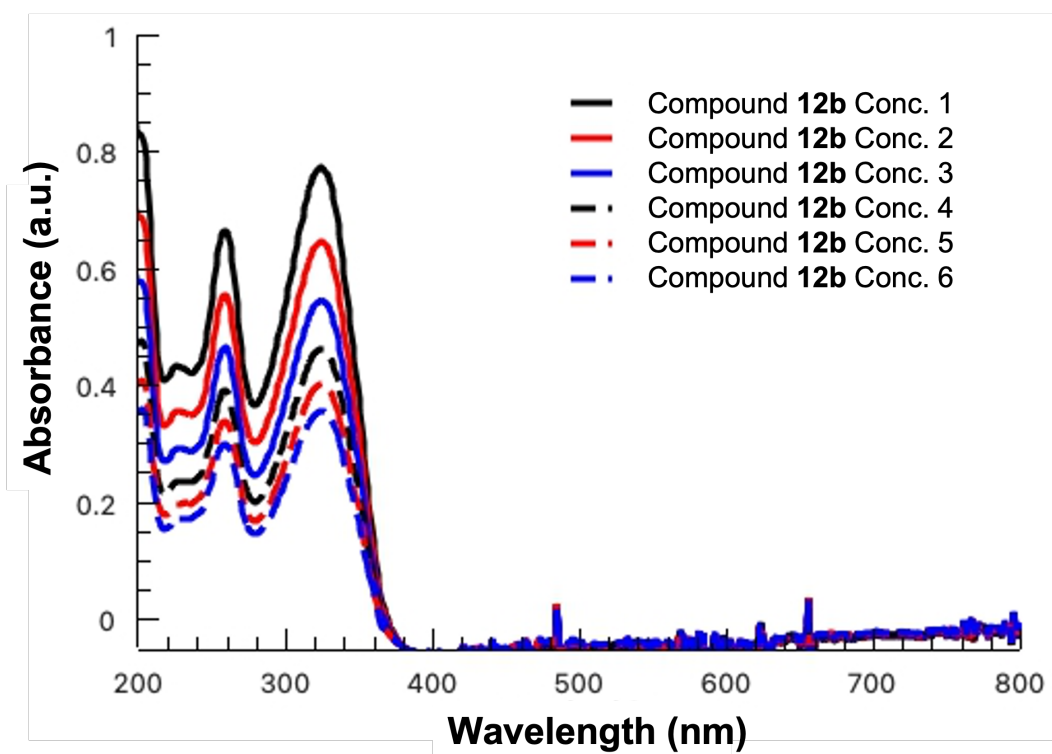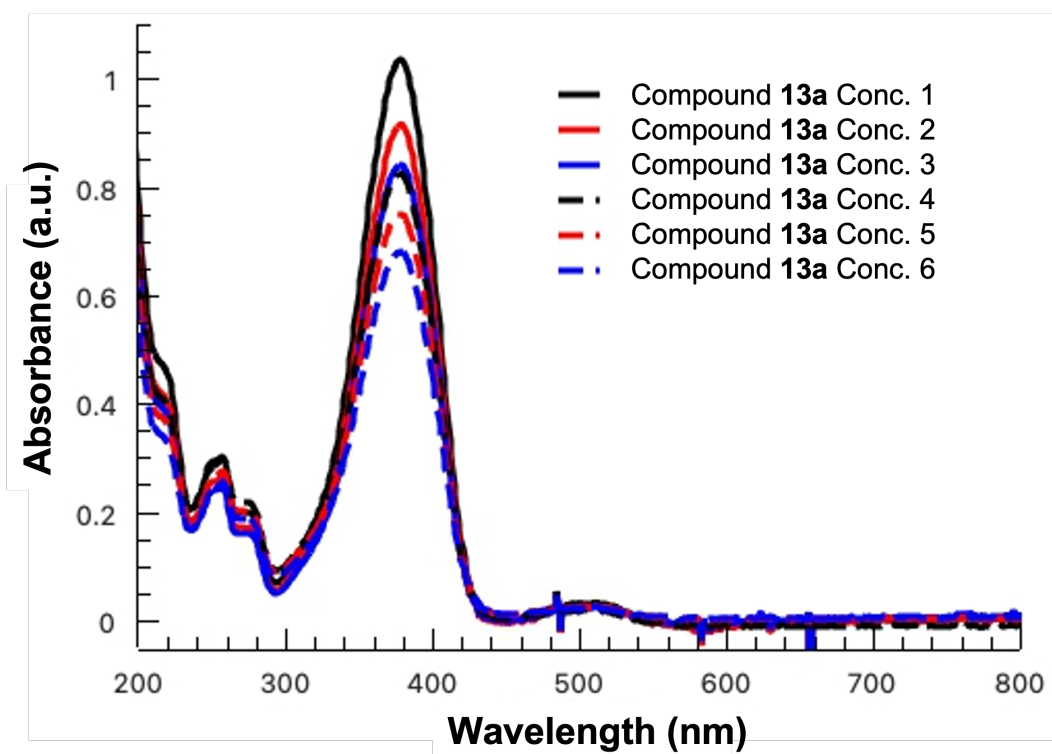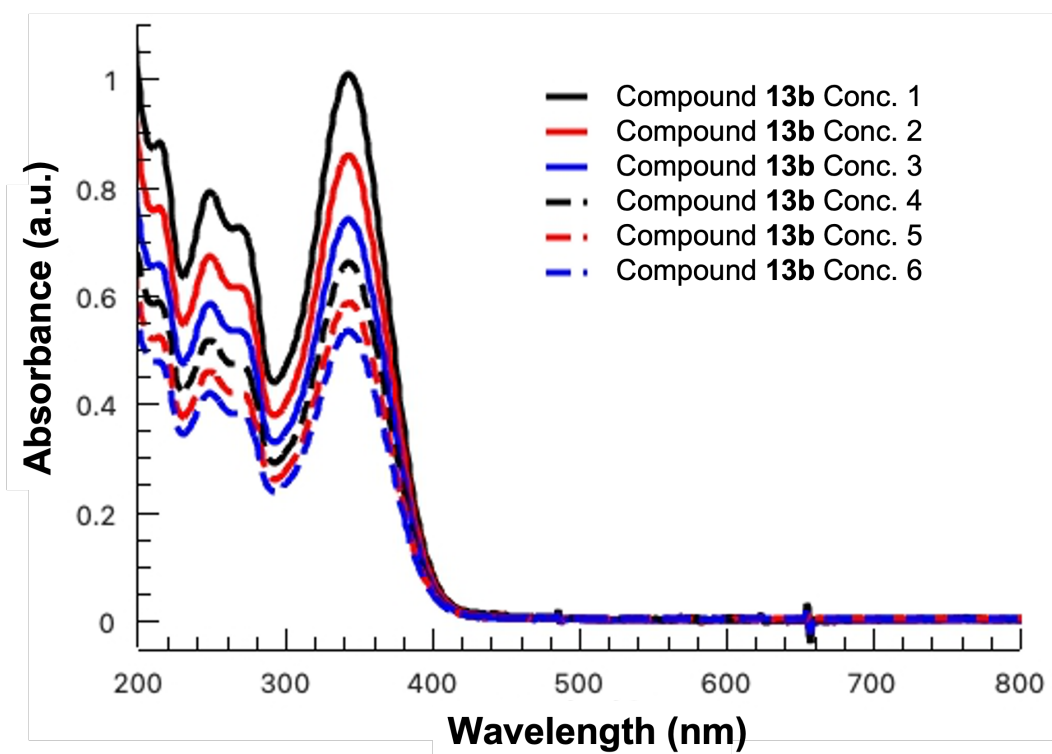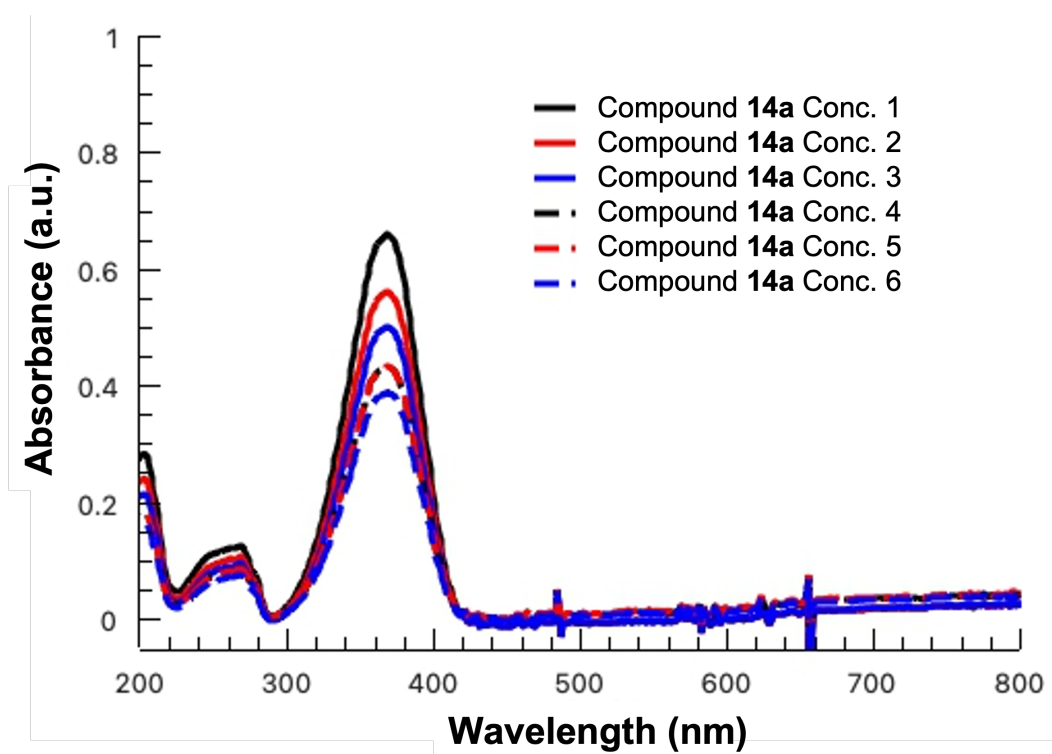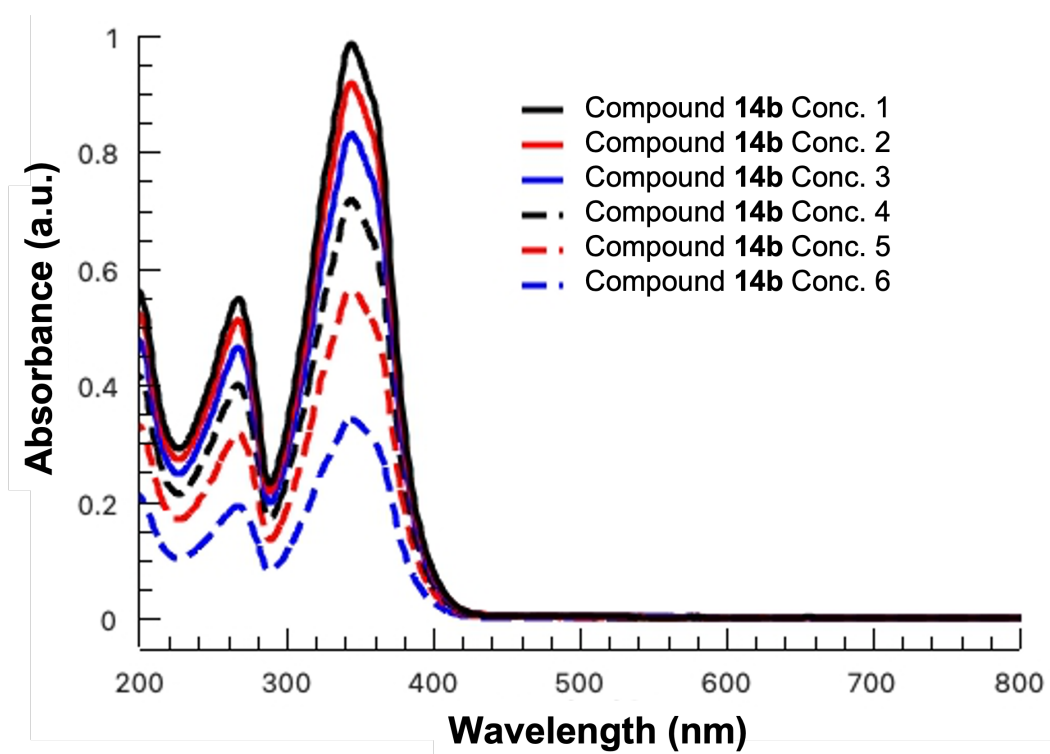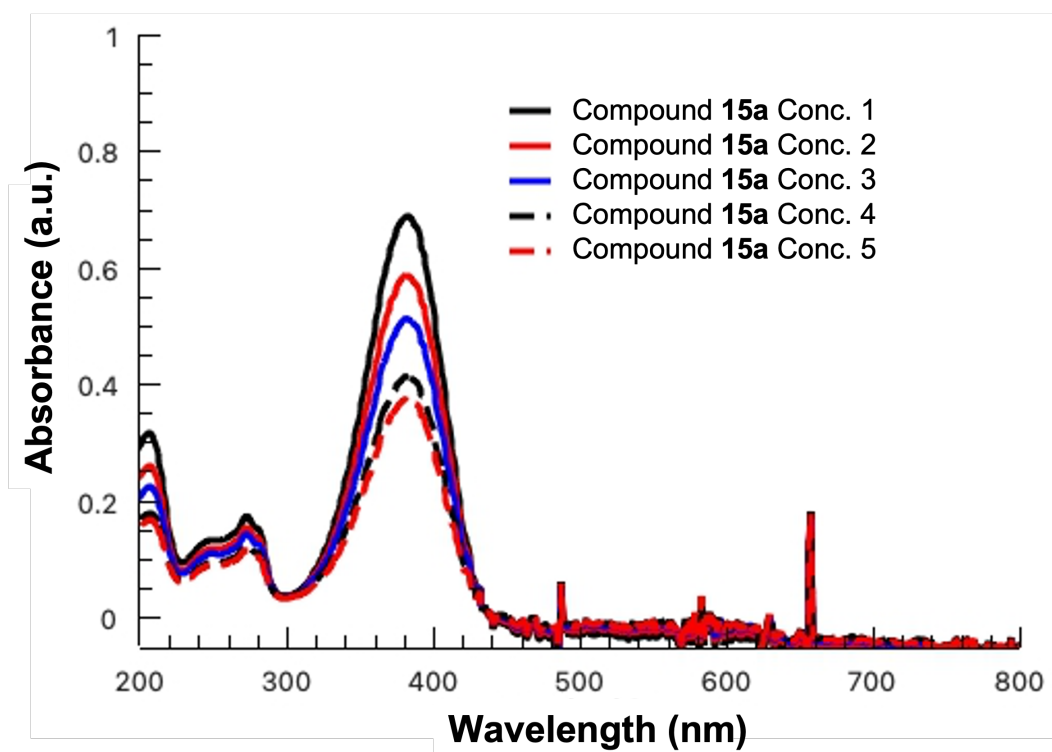
Figure S35: UV-vis spectra of compound **06** at various concentrations, with maximum absorption at 451 and 475 nm.
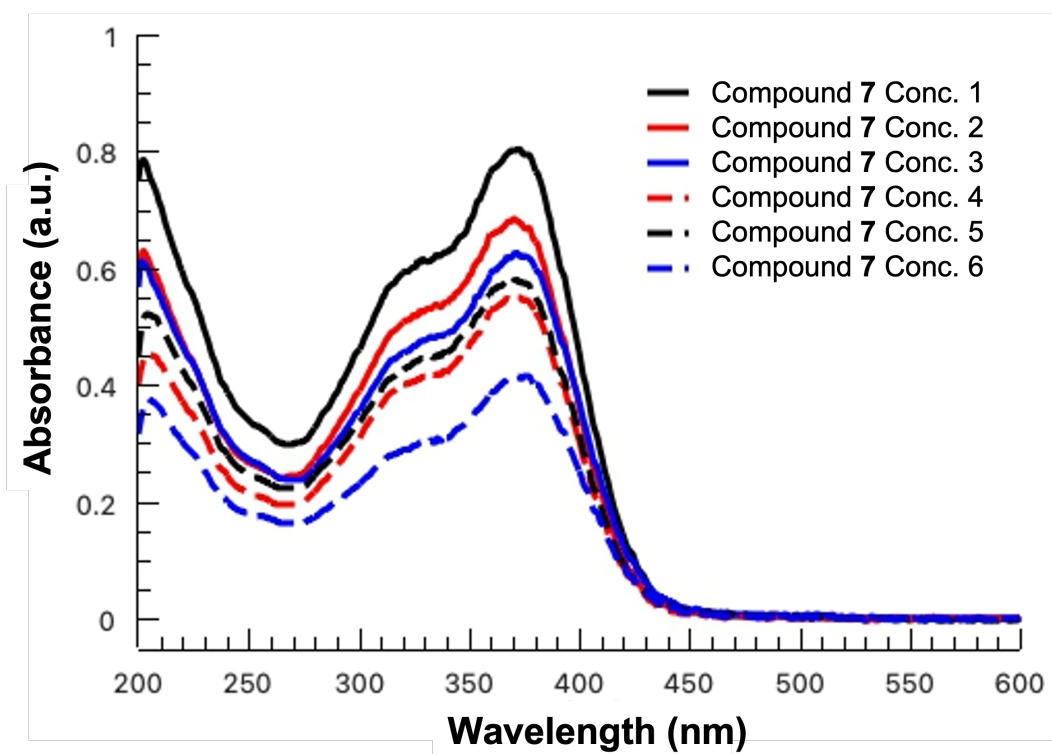
Figure S36: UV-vis spectra of compound **07** at various concentrations, with maximum absorption at 372 nm.
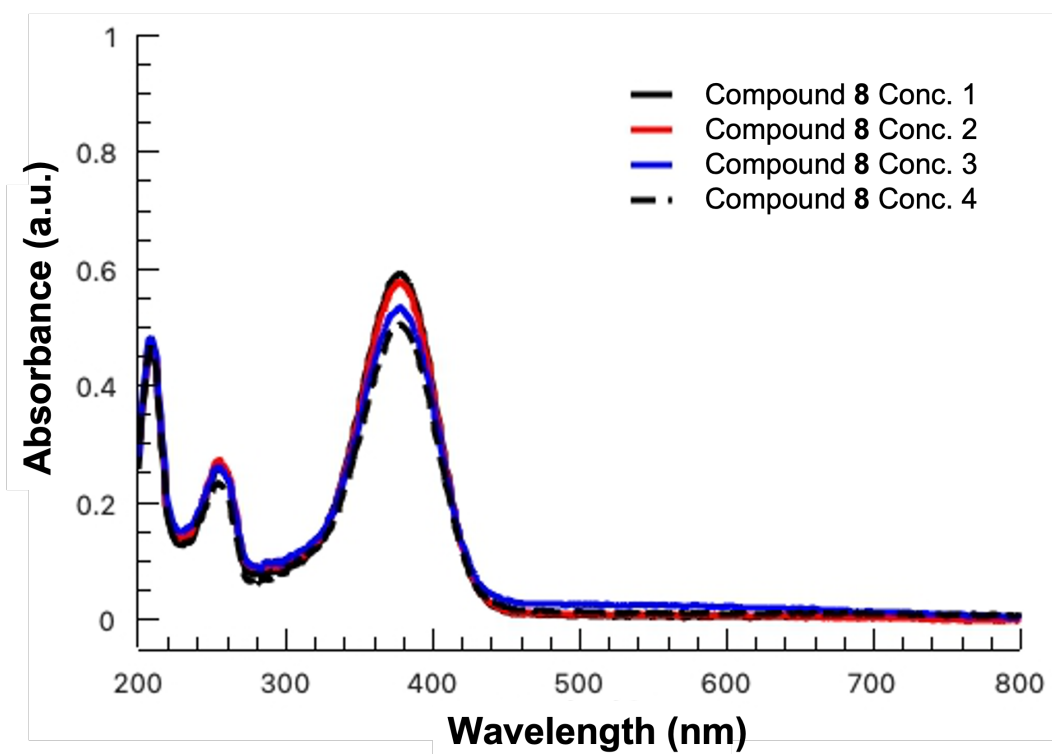
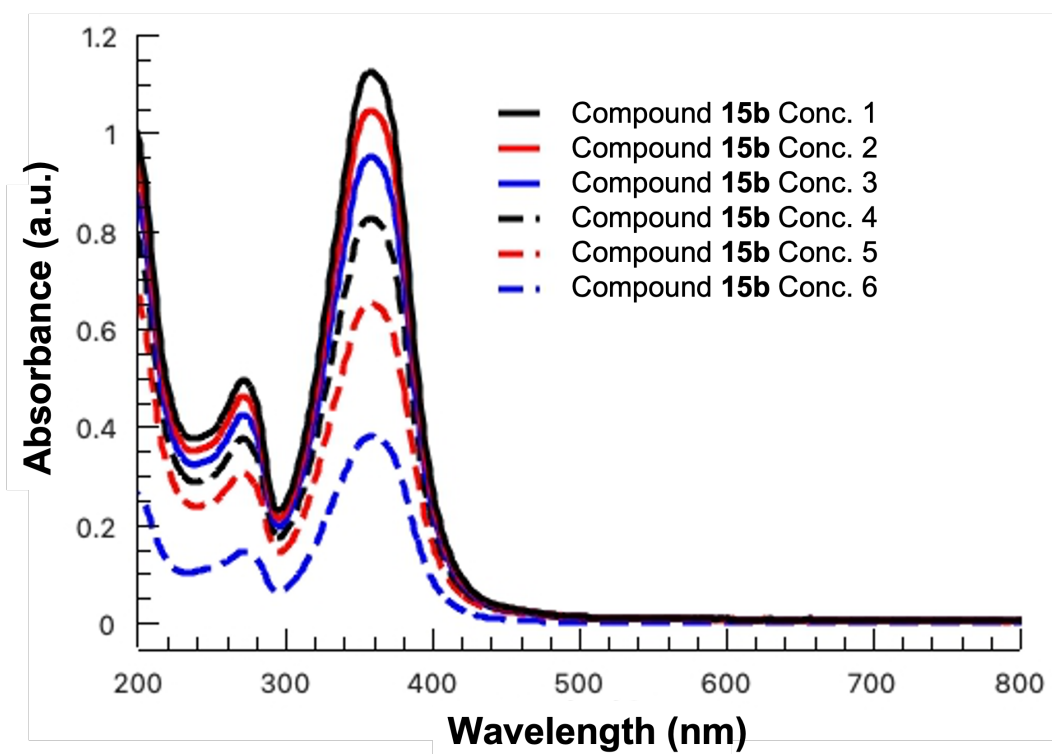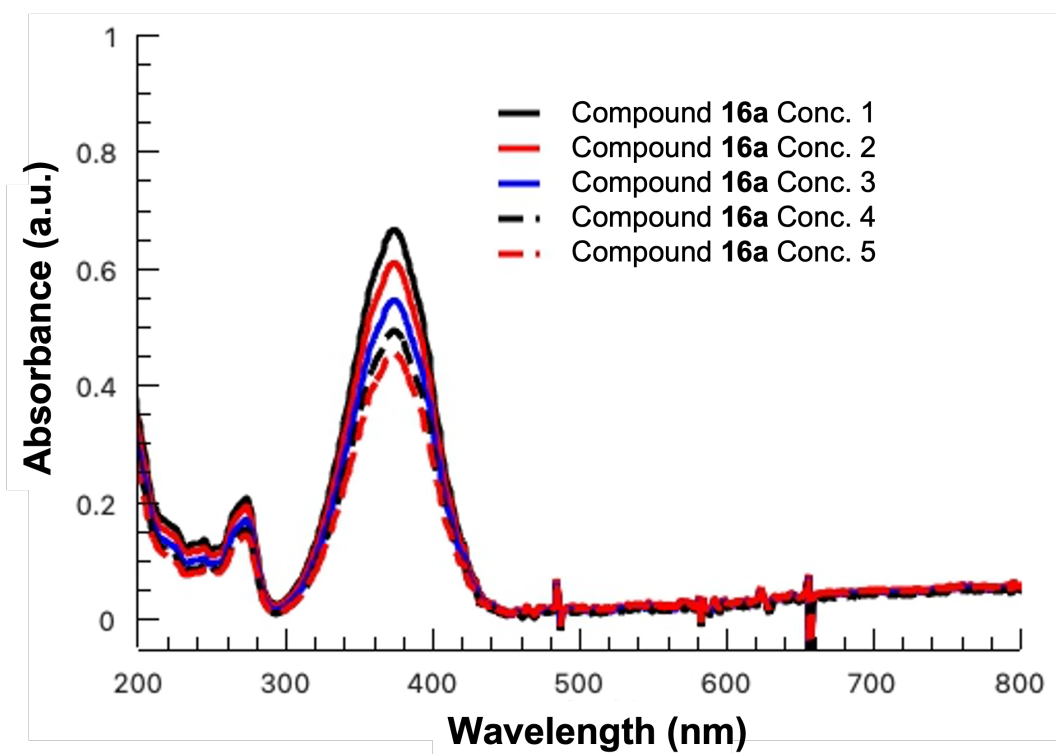Figure S37: UV-vis spectra of compound **08** at various concentrations, with maximum absorption at 378 nm.
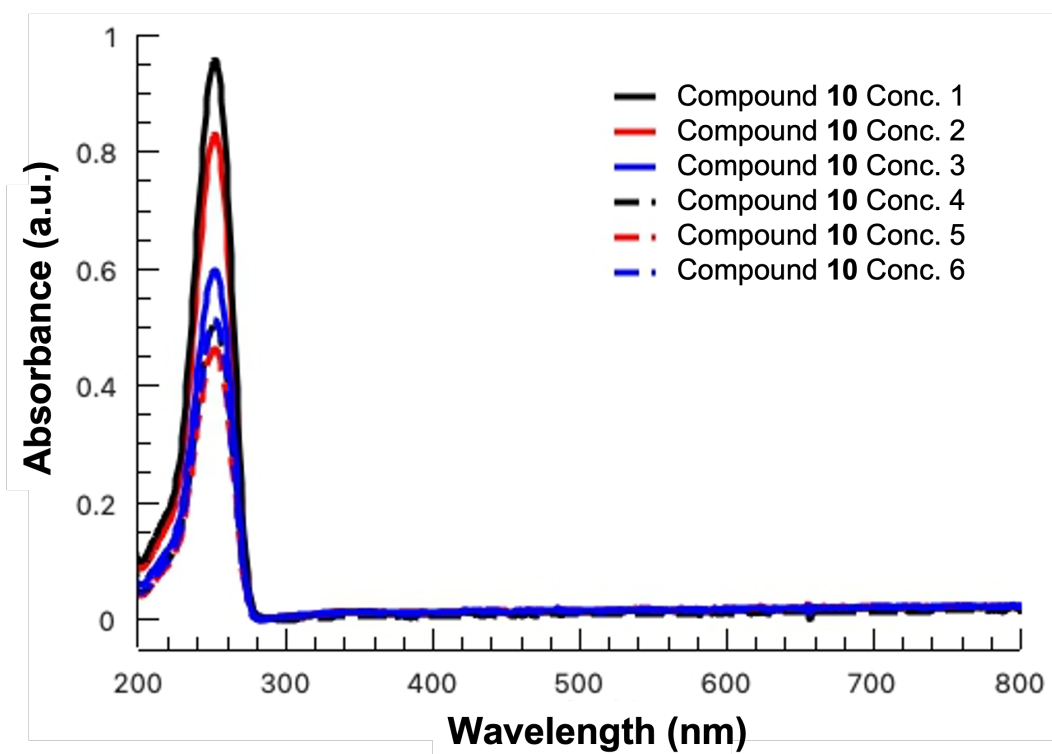
Figure S38: UV-vis spectra of compound **10** at various concentrations, with maximum absorption at 252 nm.

Figure S39: UV-vis spectra of compound **11** at various concentrations, with maximum absorption at 257 nm.

Figure S40: UV-vis spectra of compound **12a** at various concentrations, with maximum absorption at 341 nm.
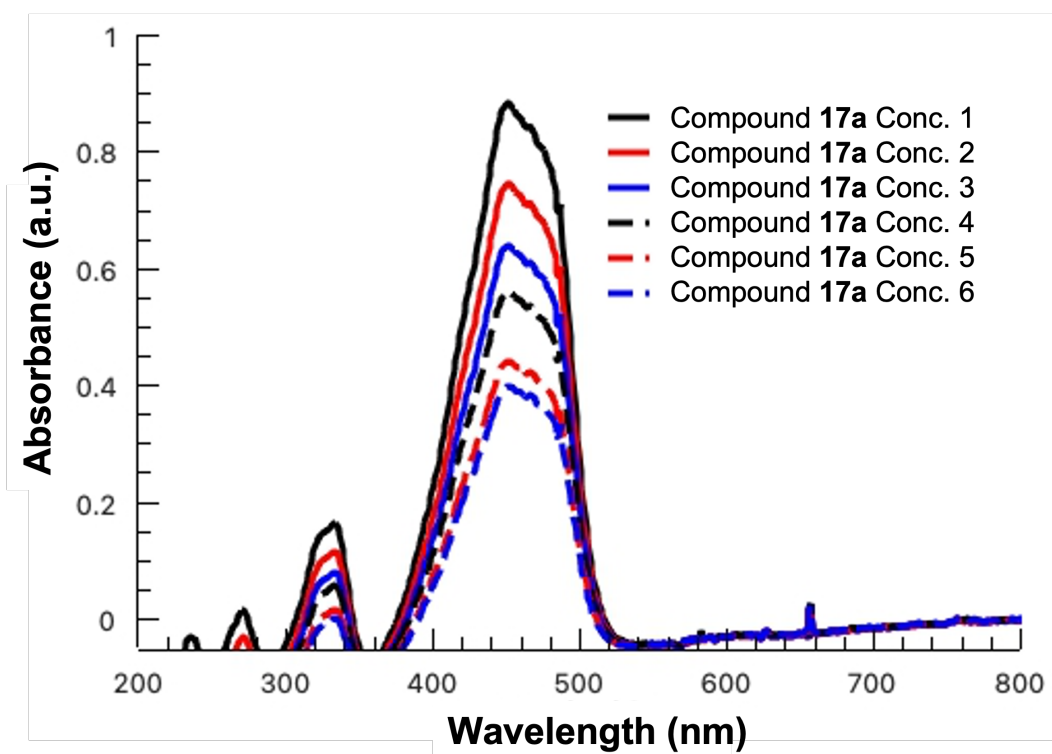
Figure S41: UV-vis spectra of compound **12b** at various concentrations, with maximum absorption at 325 nm.

Figure S42: UV-vis spectra of compound **13a** at various concentrations, with maximum absorption at 378 nm.

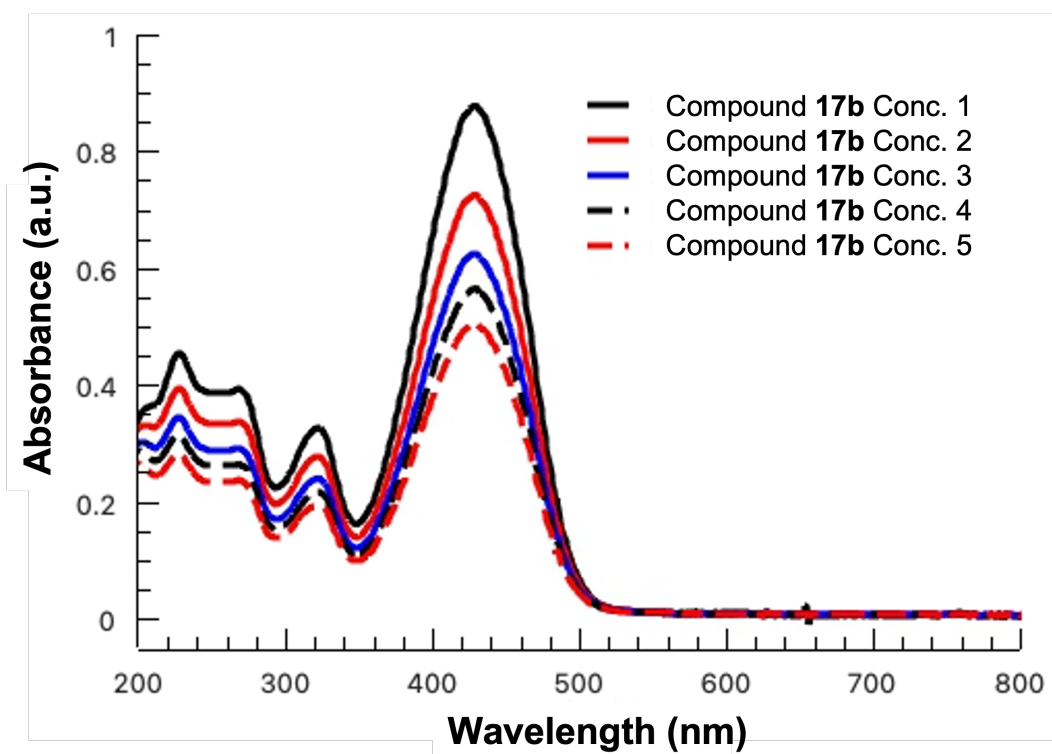Figure S43: UV-vis spectra of compound **13b** at various concentrations, with maximum absorption at 344 nm.

Figure S44: UV-vis spectra of compound **14a** at various concentrations, with maximum absorption at 368 nm.

Figure S45: UV-vis spectra of compound **14b** at various concentrations, with maximum absorption at 344 nm.

Figure S46: UV-vis spectra of compound **15a** at various concentrations, with maximum absorption at 382 nm.

Figure S47: UV-vis spectra of compound **15a** at various concentrations, with maximum absorption at 354 nm.

Figure S48: UV-vis spectra of compound **16a** at various concentrations, with maximum absorption at 374 nm.

Figure S49: UV-vis spectra of compound **17a** at various concentrations, with maximum absorption at 451 nm.

Figure S50: UV-vis spectra of compound **17b** at various concentrations, with maximum absorption at 430 nm.

B Appendix for Chapter 4: Optimization of the Synthesis of DFF from CMF.

B.1 NMR Spectra
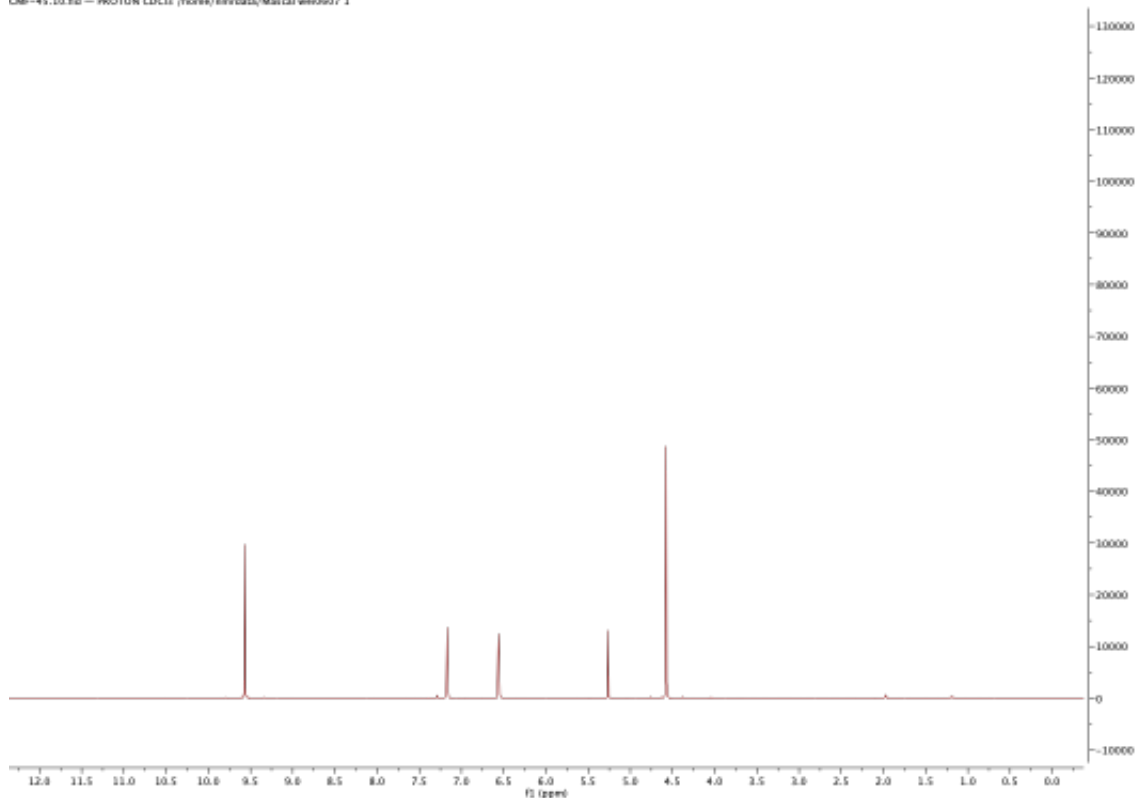
Figure S1: Proton NMR of CMF (500 MHz, CDCl$_3$): δ 6.56 (d, 1H), 7.17 (d, 1H), 4.58 (s, 2H), 9.57 (s, 1H).
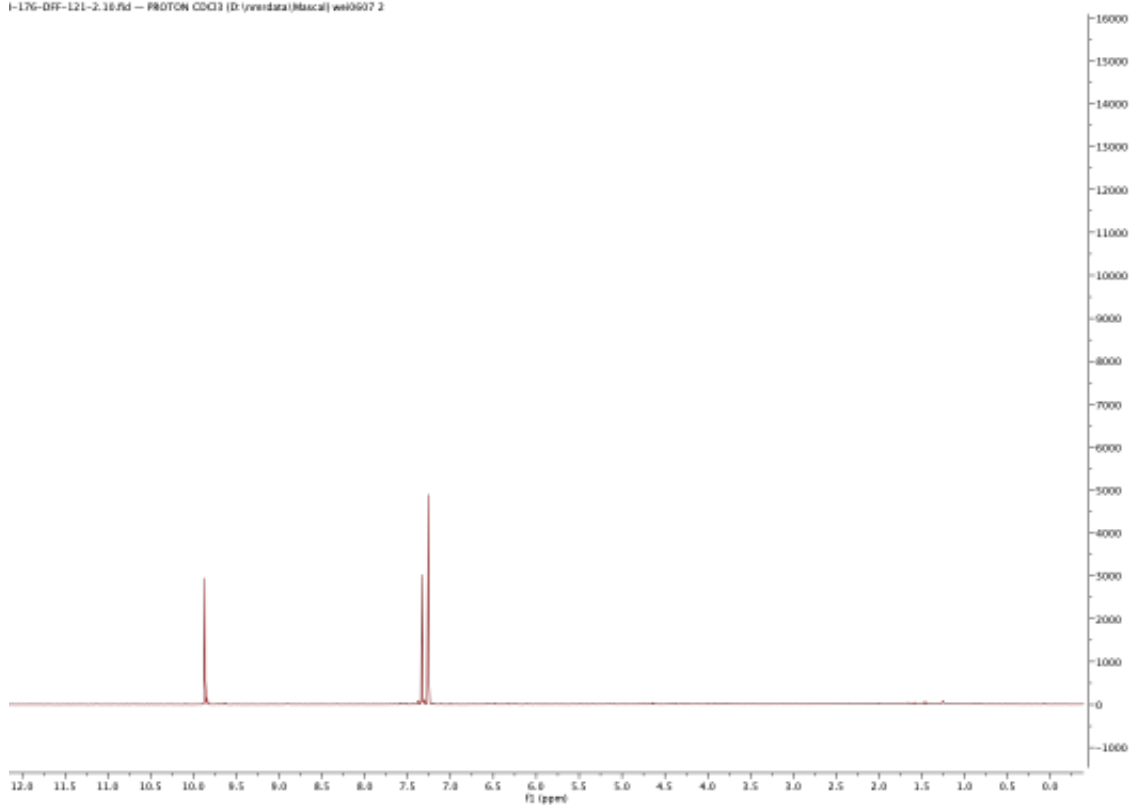
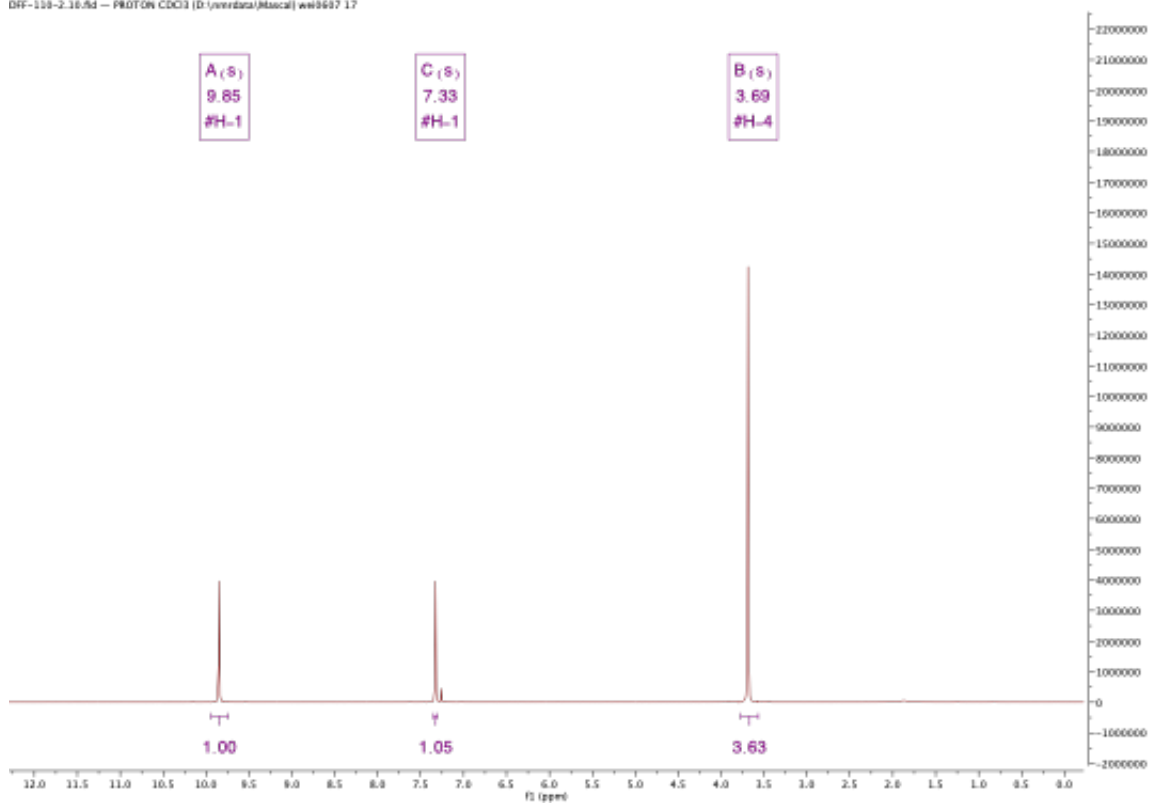Figure S2: Proton NMR of DFF (500 MHz, CDCl$_3$): CDCl$_3$: δ 9.86 (1, 1H), 7.33 (1, 1H)

Figure S3: S5: Proton NMR (500 MHz, CDCl$_3$) of DFF with 1,4-dioxane internal standard at 3.69 ppm. Sample mass: 9.6 mg, internal standard: 5 mg 1,4 dioxane, calculated DFF mass: 7.99 mg.
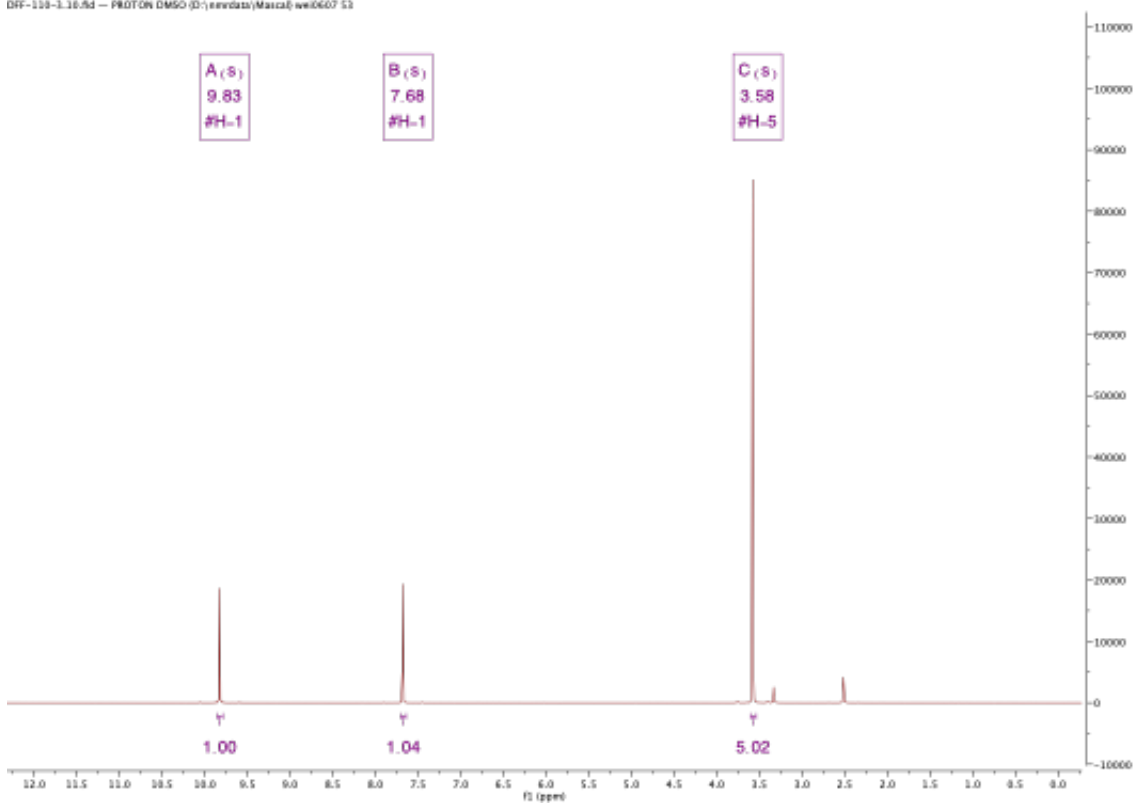
Figure S4: S5: Proton NMR (500 MHz, CDCl$_3$) of DFF with 1,4-dioxane internal standard at 3.69 ppm. Sample mass: 11.7 mg, internal standard: 5 mg 1,4 dioxane, calculated DFF mass: 6.40 mg.
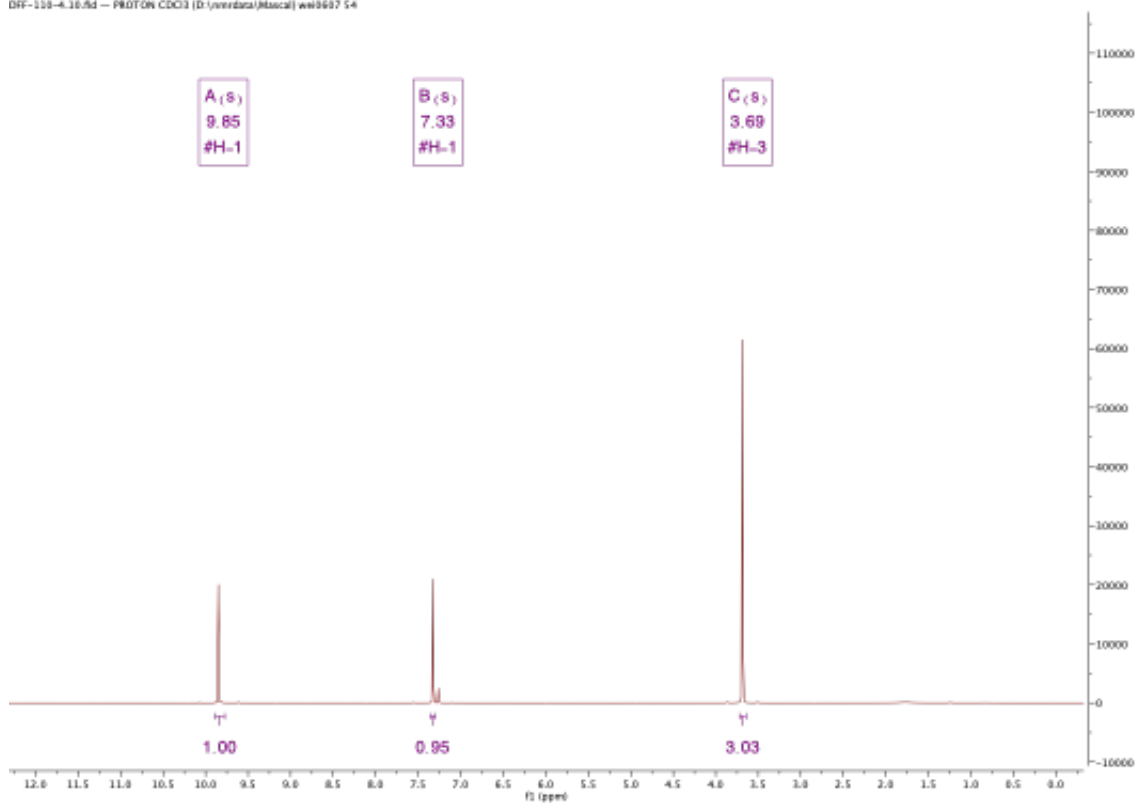
Figure S5: S5: Proton NMR (500 MHz, CDCl₃) of DFF with 1,4-dioxane internal standard at 3.69 ppm. Sample mass: 10.3 mg, internal standard: 5.6 mg 1,4 dioxane, calculated DFF mass: 10.19 mg.